Entry of Soil Gas and Radon into Houses

Andersen, Claus E.

Publication date:
1992

Document Version
Publisher's PDF, also known as Version of record

RISØ

Risø-R-623(EN)

Entry of Soil Gas and Radon into Houses

Claus E. Andersen

Risø National Laboratory, Roskilde, Denmark
April 1992

Entry of Soil Gas and Radon into Houses

Risø-R-623(EN)

Claus E. Andersen

Risø National Laboratory, Roskilde, Denmark
April 1992

Abstract Entry of soil gas and radon into houses has been investigated by a conjunction of experiments conducted at specially designed radon test structures and numerical or analytical modelling.

The numerical model solves the steady-state equations for Darcy flow of soil-gas and combined diffusive and advective transport of radon. Model calculations have been compared with results from field experiments conducted at Risø National Laboratory, and it was found that there was good agreement between measured and modelled pressure coupling and radon concentration profiles. However, discrepancies regarding absolute values of soil-gas entry rates and radon concentrations were observed.

The numerical model has been used to study the importance of soil and building related factors on radon entry rates into slab-on-grade houses. It was found, that for a house with a 3 mm perimeter crack along the floor-wall joint, the entry was mainly determined by the soil permeability and building related factors such as house depressurization and presence of a capillary breaking layer of gravel below the slab. For a house with a bare soil floor, the diffusivity of the soil was found to be of principal importance for the entry rate even for moderate permeabilities.

Finally, an analytical model has been developed for the purpose of studying soil-gas entry rates into houses in response to non-static driving forces. The model is based on the analogy between a 'buried drain' and a basement house with a perimeter crack. The modelling results have been compared with experiments conducted at a test structure at the Lawrence Berkeley Laboratory. The structure was depressurized sinusoidally in time and the frequency dependent pressure couplings were measured. There was fairly good agreement between theoretical and experimental results given the simplifying assumptions underlying the model.

This report is submitted, on February 19, 1992, to the Technical University of Denmark in partial fulfillment of the requirements for obtaining the Ph.D. degree.

The report has been revised April 1992.

E-mail address: claus@risoe.dk

ISBN-87-550-1804-1
ISSN 0106-2840

Grafisk Service · Risø · 1992

Contents

1 Introduction and summary

The radiation dose from inhaled decay products of radon (^{222}Rn) is the dominant component of radiation exposure to the general population and causes an increased risk of lung cancer; [BEIR88], [UNS88], [Nero89], [Naz90]. In Denmark, a nation-wide survey of indoor radiation was carried out in 1985-86, and it was found that the average annual effective dose equivalent due to indoor radon and its decay products amounted to 1.8 mSv y^{-1}; [Ulb88]. In a subsequent risk analysis, the current level of indoor radon was estimated to be responsible for approximately 300 lung cancer cases per year in Denmark; [Sund87].

In Denmark, the principal source of indoor radon is the subsoil under the house [Sund87], and the main objective of this study has been to establish a general model of entry of soil-gas radon into Danish houses. The entry rate depends on four factors: generation rate of radon in the subsoil, transport properties of the soil and of the interface region between soil and house, and driving forces such as indoor-outdoor pressure differences. Given the entry rate of radon, the accumulation of radon indoors depends on house volume, ventilation rate and inter-zone flows. A general understanding of the entry process is useful in the context of:

- Assessment of the impact of new (e.g. energy saving) building practices on radon entry rates.
- Improvement of building designs and practices in order to decrease future indoor radon levels.
- Cost effective search of houses with high radon levels.
- Mitigation of houses with high radon levels.

In addition, other indoor air pollutants like volatile organic compounds emanating from landfills or contaminated building sites enter houses in a way that is similar to that of radon, such that a general understanding of radon entry therefore might be useful for that problem as well; [Gar89], [Dom90].

Conceptually, this report is divided into two parts. The first part (chapter 2 to 5), outlines and applies a numerical radon entry model for static conditions. The second part (chapter 6 and 7), focuses on entry rates of soil gas in response to driving forces that are not static. Both parts are based on combinations of experimental studies conducted at specially designed radon test structures and numerical or analytical modelling. The first part of the work has been been carried out at Risø National Laboratory whereas the latter comes from a one year stay at Lawrence Berkeley Laboratory, California, USA. In the following, the content and findings of each chapter is briefly outlined.

In chapter 2 and 3, we describe a numerical model of the finite-difference type for steady transport of soil gas and radon through soil and entry into houses. The first part of the model determines the movement of soil gas in response to small indoor-outdoor pressure differences; created e.g. by wind, temperature differences, or mechanical ventilation systems. The movement itself is governed by Darcy's law. The second part of the model solves the radon transport equation that involves generation, decay, combined advective and diffusive transport, and partition of radon between gas and liquid phases of other soil fluids.

In chapter 4, we focus on the physical validity of the model and describe the results of a verification exercise grounded on the comparison of experimental results with model calculations based on measured soil parameters. The experimental results come from a radon test structure, that has been established at Risø National Laboratory as part of this study. The structure consists of a 40 liter stainless-steel cylinder placed in a 0.52 m deep quadratic excavation with a side length of

2.4 m. The excavation is lined with a 0.6 mm pvc membrane that is attached to the cylinder, and soil gas enters the cylinder through a 9.5 cm hole in the bottom. The cylinder is depressurized by a mass-flow controlled pump, and radon concentrations, pressures, and environmental parameters are logged onto a computer every 10 minutes. The experimental results used in the verification exercise include steady-state pressure couplings and radon concentrations measured in 19 soil probes located in the vicinity of the structure. In the two main experiments, radon concentrations were measured under conditions where the transport was mainly diffusive or advective: i.e. without or with an imposed depressurization. Relative to the situation where the transport was mainly diffusive, it was observed that most probe locations were partly diluted in response to radon-free atmospheric air being forced into the ground by the imposed flow. Model calculations based on measured soil parameters were made using the two-dimensional model in circular cylindrical coordinates. The model-experiment comparison showed agreement between pressure and radon concentration *profiles*, and the model was able to predict the degree of radon depletion for most probe locations. The latter verifies the models ability to describe the combined diffusive and advective transport, which is a key element of the model. However, *absolute* values of the soil-gas entry rates and radon concentrations differed from the predicted ones, which is claimed to be a result of soil inhomogeneities or incomplete mapping of some of the soil parameters.

In chapter 5, we present the results of model simulations of radon entry into (idealized) houses located on homogeneous soil. The emphasis of the sensitivity analysis is on slab-on-grade houses since this house type is common in Denmark and tend to have higher indoor radon levels compared with basement and crawlspace houses. A reference configuration is defined, and various soil and house related factors are changed in turn as to see the subsequent change in entry rate. In all cases, the entry rate is proportional to the radon generation rate of the soil. For houses with impermeable building materials and a narrow crack along the floor-wall joint, high entry rates can only be obtained by means of advective entry and the key parameters are the soil permeability and the house depressurization. For houses with a bare-soil floor, the situation is quite different since diffusive entry dominates even for moderate soil permeabilities. The influence of a subfloor gravel layer, footer, backfill region, and depressurization is also investigated and the entry into the slab-on-grade house is compared with that of a basement house of a similar configuration. The findings of the sensitivity analysis are in agreement with similar US studies conducted for basement houses.

Chapter 6 and 7 treat the specific issue of soil-gas entry into houses under conditions where the depressurization vary sinusoidally in time. An analytical model has been derived based on the analogy of a buried drain and a basement house with a perimeter crack along the floor-wall joint. The analytical treatment is performed in the frequency domain using transfer functions, and the model describes the development of the disturbance pressure field in the soil surrounding the drain. The model predicts the amplitude of the soil-gas entry rate to increase with the frequency of the depressurization. The increased flow rate comes about because of compression and expansion of gas in pore volumes of the 'active part of the soil'. In addition, an experimental investigation has been carried out at the Small Structures Project at Lawrence Berkeley Laboratory, California. Pressures have been measured in 8 soil probes while the structure was depressurized sinusoidally in time. Experiments were conducted for period times from 4 seconds up to 53 minutes, and the measured time-series have been Fourier analyzed for comparison with the theoretical transfer function. Given the simplifying assumptions underlying the model, there was good agreement between measured and modelled pressure responses.

2 Physical equations

In this chapter we define basic parameters and derive equations for steady soil-gas and radon transport in soils. The soil-gas transport equation is derived from the continuity equation, Darcy's law and the assumptions that the soil is isothermal and isotropic. The radon transport equation involves generation, decay, combined diffusive and advective transport, and partition of radon between gas and liquid phases of other soil fluids. The equation is derived under a number of simplifying assumptions. For example, we assume that water percolation and adsorption of radon to soil grain surfaces can be neglected. Similar transport equations can be found in [Naz88C], [Lou90], and [Rog91A].

The chapter is divided into three sections. Section 2.1 contains definitions of basic soil parameters like porosity, moisture content, and radon emanation. In section 2.2 and 2.3 the transport equations for soil gas and radon are derived.

2.1 Basic definitions

We treat soil as a porous medium consisting of organic matter, soil grains and pores filled with water and soil gas containing trace amounts of radon (^{222}Rn). We select a reference element of volume δV located at the point $S(x, y, z)$, and apply the continuum approach described in [Bear72]. Thus, soil properties such as the porosity and diffusivity and field values such as the radon concentration are averaged over δV and assigned to the point $S(x, y, z)$ for δV taken to a microscopic value. The interconnected pores of the reference element have a volume of δV_p. This volume is divided into an air-filled part of volume δV_a and a water-filled part of volume δV_w such that:

$$\delta V_p = \delta V_a + \delta V_w \tag{1}$$

We define porosity (ϵ), air-porosity (ϵ_a), and water-porosity (ϵ_w) as:

$$\epsilon = \frac{\delta V_p}{\delta V} \tag{2}$$

$$\epsilon_a = \frac{\delta V_a}{\delta V} \tag{3}$$

$$\epsilon_w = \frac{\delta V_w}{\delta V} \tag{4}$$

We also define the fraction of water saturation of the pores (m):

$$m = \frac{\delta V_w}{\delta V_p} = \frac{\epsilon_w}{\epsilon} \tag{5}$$

and the water content per wet mass (W):

$$W = \frac{\rho_w \delta V_w}{\rho_{ws} \delta V} = \epsilon_w \frac{\rho_w}{\rho_{ws}} = m\epsilon \frac{\rho_w}{\rho_{ws}} \tag{6}$$

where ρ_w and ρ_{ws} are densities of water and wet soil, respectively. The soil grain density ρ_g is in the range from 2.65 to 2.75 g cm^{-3} for a wide range of soils, [Har84], [Sco63]. For soils without organic matter, we have the following relations:

$$\rho_{ws} = (1 - \epsilon)\rho_g + \epsilon_w \rho_w = \frac{1 - \epsilon}{1 - W} \rho_g \tag{7}$$

and

$$\epsilon = 1 - (1 - W)\frac{\rho_{ws}}{\rho_g} \tag{8}$$

The activity of radon in δV_a is δA_a and we define the radon activity concentration of the air-filled pore parts (Bq m^{-3}) as:

$$c_a = \frac{\delta A_a}{\delta V_a} \tag{9}$$

The activity of radon in δV_w is δA_w and we define the radon activity concentration of the water-filled pore parts ($\mathrm{Bq\,m^{-3}}$) as:

$$c_w = \frac{\delta A_w}{\delta V_w} \tag{10}$$

The soil grains contain radium (^{226}Ra) and radon emanates into air-filled and water-filled pore parts. The total radon generation rate ($\mathrm{Bq\,m^{-3}\,s^{-1}}$) per pore volume ($\delta V_p$) is defined as:

$$G = \rho_s \frac{1-\epsilon}{\epsilon} \lambda f A_{Ra} = \frac{\rho_{ws} - \epsilon_w \rho_w}{\epsilon} \lambda E = \frac{1-W}{\epsilon} \rho_{ws} \lambda E \tag{11}$$

where λ is the decay constant of radon ($2.098 \cdot 10^{-6}\ \mathrm{s^{-1}}$). f is the emanating fraction, and A_{Ra} the concentration of radium in the soil grains (activity per grain mass). The emanation rate, E, gives the number of atoms that emanate into the pores per unit time per kg dry mass (i.e. organic matter and grains) of the soil[1]. We divide the generation rate into two terms, G_a and G_w, reflecting the amount of radon atoms that emanate into the air-filled and water-filled part of the pores. We have the relation:

$$G = G_a + G_w \tag{12}$$

2.2 Soil-gas transport

Soil gas moves in response to pressure differences created, for example, below houses because of the influence from wind, temperature and ventilation: [Naz88C], p. 92 For simplicity, we assume that the soil is isothermal and that soil gas simply moves in response to pressure differences imposed at the boundaries: e.g. that the house interior is depressurized relative to the atmospheric surface[2].

We define the disturbance pressure field $p(x, y, z)$ at a given location of the soil as the difference between the absolute pressure $P(x, y, z)$ at that point and the 'hydrostatic' pressure at that depth $P_H(z)$: [Lou87], p.37:

$$P(x, y, z) = P_H(z) + p(x, y, z) \tag{13}$$

where

$$P_H(z) = P_{atm} - \rho_a g z \tag{14}$$

where the z-axis is oriented vertically (pointing upwards). P_{atm} is the absolute pressure at the atmospheric surface ($\sim$ 101 kPa). ρ_a the soil-gas density ($\sim$ 1.3 $\mathrm{kg\,m^{-3}}$), and g the gravitational acceleration ($\sim 9.8\ \mathrm{m\,s^{-2}}$). For the stated typical values of the parameters, the hydrostatic pressure decreases app. 12 Pa per meter of depth. The transport of soil gas is assumed to follow Darcy's law:

$$\vec{q} = -\frac{k}{\mu} \nabla p \tag{15}$$

where $\vec{q}$ is the bulk flux density of soil-gas ($\mathrm{m^3/(m^2\,s)}$), k is the permeability ($\mathrm{m^2}$), and μ the dynamic viscosity ($\sim 18 \cdot 10^{-6}$ Pa s). Darcy's law implies that the flow is irrotational corresponding to potential flow with the disturbance pressure field as velocity potential. The equation of continuity (mass conservation) of gas in a porous medium is, [Bird60]:

$$\frac{\partial \epsilon \rho_a}{\partial t} + \nabla \cdot \rho_a \vec{q} = 0 \tag{16}$$

[1] *For soils without organic matter, we have* $E = f A_{Ra}$

[2] It was recently demonstrated in a modelling study, that buoyancy created by the heat loss from a basement might be an important driving force for soil-gas entry. [Rev91]

Table 1. Radon solubility in water as function of temperature (from [Clev79], p. 228).

Temp. K	L -
273.15	0.5249
278.15	0.4286
283.15	0.3565
288.15	0.3016
293.15	0.2593
298.15	0.2263
303.15	0.2003
308.15	0.1797

Under steady-state conditions we obtain:

$$\nabla \cdot \rho_a \bar{q} = 0 \tag{17}$$

Soil gas is compressible and in general the density is a function of the absolute pressure; for isothermal conditions the density is directly proportional to the absolute pressure. However, we neglect this in the present steady-state model since the maximum value of the disturbance pressure field is of the order of only 5 Pa (0.005 % of P_{atm}) and since the soil column of interest extends only a few meters below the atmospheric surface. Hence, in the following, we assume the soil gas to have a constant density and equation 17 becomes:

$$\nabla \cdot \bar{q} = 0 \tag{18}$$

Inserting Darcy's law gives:

$$\nabla \cdot (k \nabla p) = 0 \tag{19}$$

such that for homogeneous soils the disturbance pressure field obeys the Laplace equation[3]:

$$\nabla^2 p = 0 \tag{20}$$

2.3 Radon transport

We assume that the partition of radon between the gas and liquid phases is permanently in equilibrium: cf. [Roy91]. This appears to be a reasonable assumption since the mass transfer from air to water is rapid: a characteristic time of 0.1 sec is estimated in [Naz88C], p. 78. The concentration ratio is given by the Ostwald coefficient, L: [Clev79]:

$$c_w = L c_a \tag{21}$$

L depends on the temperature as specified in table 1. Radon also adsorbs to soil grain surfaces. However, data presented in [Rog91A] suggests that this effect is important only for dry soils (m <0.2-0.3) and we therefore limit this treatment to radon in the gas and liquid phases. We have the following equation for radon in the liquid phase:

$$\epsilon_w \frac{\partial c_w}{\partial t} = \epsilon G_w - \epsilon_w \lambda c_w \tag{22}$$

where we have neglected transport of radon, e.g. advection due to percolating water. Finally for radon in the air-filled pores, we have the equation:

[3] Inclusion of isothermal expansion gives the following equation for the absolute pressure field: $\nabla^2 P^2 = 0$; see [Car56], p. 5 or [Bird60], p. 150.

$$\epsilon_a \frac{\partial c_a}{\partial t} = \epsilon G_a - \epsilon_a \lambda c_a - \nabla \cdot \vec{j} \tag{23}$$

where the bulk flux density $\vec{j}$ ($\mathrm{Bq\,m^{-2}\,s^{-1}}$)) specifies the transport of radon within the air-filled pore parts per bulk cross-sectional area per unit time. The transport rate of radon, J ($\mathrm{Bq\,s^{-1}}$), across a plane with a uniform flux density of $\vec{j}$ is hence: $J = \vec{j} \cdot A\hat{a}$, where A is the geometric area of the plane, and $\hat{a}$ is a unit vector perpendicular to the plane. Equations 21, 22, and 23 can be combined to one equation for radon in the gas phase:

$$\beta \frac{\partial c_a}{\partial t} = \epsilon G - \beta \lambda c_a - \nabla \cdot \vec{j} \tag{24}$$

where we have introduced the quantity β, which we choose to call the partition-corrected porosity:

$$\beta = \epsilon_a + L\epsilon_w \tag{25}$$

The transport of radon within the air-filled pore parts is divided into two terms: the advective[4] and diffusive bulk flux density:

$$\vec{j} = \vec{j_a} + \vec{j_d} \tag{26}$$

where

$$\vec{j_a} = c_a \vec{q} = -c_a \frac{k}{\mu} \nabla p \tag{27}$$

and

$$\vec{j_d} = -D \nabla c_a \tag{28}$$

where the latter is Fick's first law and D is the bulk diffusion constant ($\mathrm{m^2\,s^{-1}}$). Inserting the expressions for $\vec{j_a}$ and $\vec{j_d}$ in equation 24 gives:

$$\frac{\partial c_a}{\partial t} = \frac{\epsilon G}{\beta} - \lambda c_a + \frac{1}{\beta} \frac{k}{\mu} \nabla p \cdot \nabla c_a + \frac{1}{\beta} \nabla \cdot (D \nabla c_a) \tag{29}$$

Homogeneous soil

If the soil is homogeneous and has a uniform distribution of moisture (m = constant), it is possible to eliminate β from equation 29 by introducing a set of new parameters: cf. [Rog91A]: G', D', and k' such that the transport equations takes the form:

$$\frac{\partial c_a}{\partial t} = G' - \lambda c_a - \frac{1}{\epsilon_a} \nabla \cdot \vec{j'} \tag{30}$$

or

$$\frac{\partial c_a}{\partial t} = G' - \lambda c_a + \frac{1}{\epsilon_a} \frac{k'}{\mu} \nabla p \cdot \nabla c_a + \frac{1}{\epsilon_a} \nabla \cdot (D' \nabla c_a) \tag{31}$$

where

$$\vec{j'} = \frac{\epsilon_a}{\beta} \vec{j} = -c_a \frac{k'}{\mu} \nabla p - D' \nabla c_a \tag{32}$$

$$D' = \frac{\epsilon_a}{\beta} D \tag{33}$$

$$k' = \frac{\epsilon_a}{\beta} k \tag{34}$$

$$G' = \frac{\epsilon}{\beta} G \tag{35}$$

Furthermore, we may define the effective diffusion constant D'_e such that:

[4] The terms 'advection' and 'convection' are used widely in the radon literature. Here, we adopt the definitions used in [Dom90], where advection refers to solute and particle transport, whereas convection is used to emphasize heat related transport (e.g. natural or forced convection). Cf. [Inc85] p. 6 and 258, and [Rev91].

$$D' = \epsilon_a D'_e \tag{36}$$

or equivalently:

$$D'_e = \frac{D}{\beta} \tag{37}$$

and obtain:

$$\frac{\partial c_a}{\partial t} = G' - \lambda c_a + \frac{1}{\epsilon_a}\frac{k'}{\mu}\nabla p \cdot \nabla c_a + \nabla \cdot (D'_e \nabla c_a) \tag{38}$$

Under steady-state conditions we finally have:

$$G' - \lambda c_a + \frac{1}{\epsilon_a}\frac{k'}{\mu}\nabla p \cdot \nabla c_a + \nabla \cdot (D'_e \nabla c_a) = 0 \tag{39}$$

Sample calculation

It is instructive to consider the steady-state solution of equation 39 for a semi-infinite, homogeneous and diffusion-dominated soil layer. In one dimension, equation 39 is equivalent to:

$$D'_e \frac{d^2 c_a}{dz^2} = \lambda c_a - G' \tag{40}$$

where z is the depth. For the atmospheric concentration set to zero, we obtain the following solution for $z \geq 0$:

$$c_a(z) = c_{a,\infty}(1 - \exp(-\frac{z}{L_d})) \tag{41}$$

where $c_{a,\infty}$ is the deep-soil radon concentration:

$$c_{a,\infty} = \frac{G'}{\lambda} = \frac{\epsilon}{\beta}\frac{G}{\lambda} = \frac{1-W}{\beta}\rho_w E \tag{42}$$

and L_d is the diffusion length:

$$L_d = \sqrt{\frac{D'_e}{\lambda}} \tag{43}$$

The exhalation rate J ($\mathrm{Bq\,s^{-1}}$) into the atmosphere over the surface area A (at $z = 0$) is:

$$J = -\vec{z} \cdot A\vec{j} = -\vec{z} \cdot A\frac{\beta}{\epsilon_a}\vec{j}' = A\beta D'_e \frac{c_{a,\infty}}{L_d} \tag{44}$$

A list of other closed-form solutions can be found in [Col81].

3 Numerical model

In this chapter we outline a two-dimensional numerical model that solves the equations for steady soil-gas and radon transport. The model is flexible and problems related to our test structure (chapter 4), real houses (chapter 5), or soil probes can be modelled in detail. The model is of the finite-difference type and is based on the widely used control-volume approach presented by Patankar: [Pat80]. Loureiro applied the same scheme in a previous model of radon transport, and this model is partly based on that work: [Lou87].

The chapter is divided into two sections. Firstly, we outline the numerical method and derive a discretization equation that matches the two-phase transport equation. Secondly, we present details related to the computational implementation and mathematical verification.

3.1 Numerical technique

The model solves the following two equations of the previous chapter with appropriate boundary conditions governing soil-gas and radon transport:

$$\nabla \cdot \vec{q} = 0 \tag{45}$$

and

$$\epsilon G - \beta \lambda c_a - \nabla \cdot \vec{j} = 0 \tag{46}$$

where

$$\vec{q} = -\frac{k}{\mu} \nabla p \tag{47}$$

and

$$\vec{j} = c_a \vec{q} - D \nabla c_a \tag{48}$$

From a mathematical point of view, the soil-gas transport equation is a special case of the more general radon transport equation, and we can solve the two equations with the same numerical technique[5]. In the following we therefore focus on the numerical method used to solve the radon transport equation. The method consists of the following three steps:

- Select grid: A two-dimensional computational grid containing $M \cdot N$ control-volumes is selected.
- Set-up matrix equation: The radon concentration at individual grid points is linked to the concentrations of the four nearest neighbours through a finite-difference approximation of the transport equation. Thus, we convert the original boundary value problem into a system of $M \cdot N$ algebraic equations with $M \cdot N$ unknowns. The matrix elements reflect the dimensions of the control volumes and the soil parameters.
- Solve matrix equation: The matrix equation is solved iteratively using a line-iterative procedure that is based on the Thomas algorithm and successive over-relaxation: [And84].

Each control volume consists of one node and four interfaces. The control volumes are not (in general) of equal size and the nodes are located midway between interfaces.

[5] To see this, interpret the radon concentration as pressure, ignore decay, generation and advection, and set the diffusion constant to k/μ.

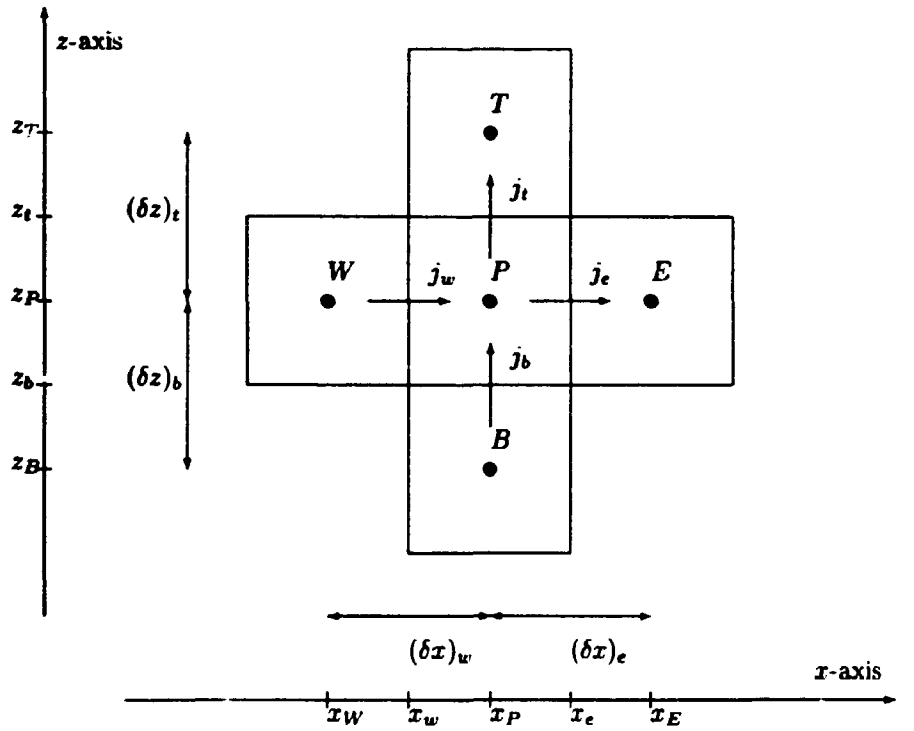

Figure 1. Location of control volumes.

Figure 1 shows a cluster of 5 generic control volumes named: P, W, E, B, and T, respectively. Control volume P is located in the center at node (i,j) and W is located on the west side at node $(i-1,j)$. The other control volumes are located in a similar fashion on the east, bottom, and top sides.

In the following, uppercase letters are used as reference index for soil properties or field values that relate to single nodes (e.g. ΔV_P) whereas lowercase letters are used as reference index for quantities that relate to the interface between two nodes (e.g. A_w). The control volumes are characterized as follows:

ΔV_P = volume of control volume P, m^3

x_w = coordinate of w-interface, m

x_e = coordinate of e-interface, m

x_b = coordinate of b-interface, m

x_t = coordinate of t-interface, m

$(\delta x)_w$ = distance from node W to P, m

$(\delta x)_e$ = distance from node E to P, m

$(\delta z)_b$ = distance from node B to P, m

$(\delta z)_t$ = distance from node T to P, m

A_w = area of interface between node W and P, m^2

A_e = area of interface between node E and P, m^2

A_b = area of interface between node B and P, m^2

A_t = area of interface between node T and P, m^2

The two dimensions of the model are universally referred to as x and z, and the model is implemented such that these two coordinates optionally can be interpreted as ordinary cartesian or cylindrical coordinates[6]. For cartesian coordinates, the length of the control volume in the y-direction is set to L_y and we have:

$$\begin{aligned} \Delta V_P &= L_y(x_e - x_w)(z_t - z_b) \\ A_e &= L_y(z_t - z_b) \\ A_w &= L_y(z_t - z_b) \\ A_b &= L_y(x_e - x_w) \\ A_t &= L_y(x_e - x_w) \end{aligned} \tag{49}$$

For cylindrical coordinates, the model coordinates x and z represent r and z in the normal (r, θ, z)-notation. It is thereby implicitly assumed, that the fields are axial-symmetric such that the polar angle θ can be left out of the equations. We have the following relations for the control volume sizes:

$$\begin{aligned} \Delta V_P &= \pi(x_e^2 - x_w^2)(z_t - z_b) \\ A_e &= 2\pi x_e(z_t - z_b) \\ A_w &= 2\pi x_w(z_t - z_b) \\ A_b &= \pi(x_e^2 - x_w^2) \\ A_t &= \pi(x_e^2 - x_w^2) \end{aligned} \tag{50}$$

We prescribe a discretization equation for each control volume that expresses the conservation of radon. Thus, integration of equation 46 over a control volume gives[7]:

$$\Delta V_P(\epsilon_P G - \beta\lambda c_P) + A_w j_w - A_e j_e + A_b j_b - A_t j_t = 0 \tag{51}$$

where

ϵ_P = porosity (ϵ) within P, –

β_P = value of β ($\epsilon_a + L\epsilon_w$) within P , –

G_P = radon generation rate (G) within P, $\mathrm{Bq\,m^{-3}\,s^{-1}}$

c_P = gas phase radon concentration (c_a) within P, $\mathrm{Bq\,m^{-3}}$

j_w = bulk flux density ($\hat{x} \cdot \vec{j}$) at w-interface, $\mathrm{Bq\,m^{-2}\,s^{-1}}$)

j_e = bulk flux density ($\hat{x} \cdot \vec{j}$) at w-interface, $\mathrm{Bq\,m^{-2}\,s^{-1}}$)

j_b = bulk flux density ($\hat{z} \cdot \vec{j}$) at w-interface, $\mathrm{Bq\,m^{-2}\,s^{-1}}$)

j_t = bulk flux density ($\hat{z} \cdot \vec{j}$) at w-interface, $\mathrm{Bq\,m^{-2}\,s^{-1}}$)

We use the following symbols for the radon concentration of the neighbour nodes:

c_W = gas phase radon concentration (c_a) within W, $\mathrm{Bq\,m^{-3}}$

c_E = gas phase radon concentration (c_a) within E, $\mathrm{Bq\,m^{-3}}$

c_B = gas phase radon concentration (c_a) within B, $\mathrm{Bq\,m^{-3}}$

c_T = gas phase radon concentration (c_a) within T, $\mathrm{Bq\,m^{-3}}$

[6] In this report we apply the model only in cylindrical coordinates.

[7] We assume that the bulk flux densities prevail over each of the control volume interfaces.

For a moment, we ignore the advective transport of radon and assume a linear concentration profile between neighbour nodes. Hence, the bulk fluxes at the interfaces are given by:

$$j_w = D_w \frac{c_W - c_P}{(\delta x)_w} \tag{52}$$

$$j_e = D_e \frac{c_P - c_E}{(\delta x)_e} \tag{53}$$

$$j_b = D_b \frac{c_B - c_P}{(\delta z)_b} \tag{54}$$

$$j_t = D_t \frac{c_P - c_T}{(\delta z)_t} \tag{55}$$

The mean diffusion constants D_w, D_e, D_b, and D_t between neighbour nodes (of different material) should be calculated as to give the best representation of the fluxes at the interfaces. This is accomplished by the following procedure; [Pat80], p. 45:

$$D_w = \left(\frac{1 - f_w}{D_W} + \frac{f_w}{D_P} \right)^{-1} \tag{56}$$

$$D_e = \left(\frac{1 - f_e}{D_P} + \frac{f_e}{D_E} \right)^{-1} \tag{57}$$

$$D_b = \left(\frac{1 - f_b}{D_B} + \frac{f_b}{D_P} \right)^{-1} \tag{58}$$

$$D_t = \left(\frac{1 - f_t}{D_P} + \frac{f_t}{D_T} \right)^{-1} \tag{59}$$

where

D_P = bulk diffusion constant (D) within P, $\mathrm{m^2\,s^{-1}}$

D_W = bulk diffusion constant (D) within W, $\mathrm{m^2\,s^{-1}}$

D_E = bulk diffusion constant (D) within E, $\mathrm{m^2\,s^{-1}}$

D_B = bulk diffusion constant (D) within B, $\mathrm{m^2\,s^{-1}}$

D_T = bulk diffusion constant (D) within T, $\mathrm{m^2\,s^{-1}}$

f_w, f_e, f_b, and f_t give the location of the respective interfaces relative to the distance between neighbour nodes. For example, if the w-interface happens to be located midway between node W and P, then $f_w = 0.5$. In general we have:

$$f_w = \frac{x_P - x_w}{(\delta x)_w} \tag{60}$$

$$f_e = \frac{x_E - x_e}{(\delta x)_e} \tag{61}$$

$$f_b = \frac{z_P - z_b}{(\delta z)_b} \tag{62}$$

$$f_t = \frac{z_T - z_t}{(\delta z)_t} \tag{63}$$

where the x and z coordinates of nodes and interfaces are defined in figure 1. We then introduce the conductivities:

$$Y_w = \frac{D_w A_w}{(\delta x)_w} \tag{64}$$

$$Y_e = \frac{D_e A_e}{(\delta x)_e} \tag{65}$$

$$Y_b = \frac{D_b A_b}{(\delta z)_b} \tag{66}$$

$$Y_t = \frac{D_t A_t}{(\delta z)_t} \tag{67}$$

and rewrite equation 51 as:

$$(Y_w+Y_e+Y_b+Y_t+\beta_P\Delta V_P\lambda)c_P = Y_w c_W+Y_e c_E+Y_b c_B+Y_t c_T+\epsilon_P\Delta V_P G_P \tag{68}$$

This equation is of the general form used by Patankar:

$$a_P c_P = a_W c_W + a_E c_E + a_B c_B + a_T c_T + b \tag{69}$$

and we identify the coefficients:

$$\begin{aligned} a_W &= Y_w \\ a_E &= Y_e \\ a_B &= Y_b \\ a_T &= Y_t \\ b &= \epsilon_P\Delta V_P G_P \\ a_P &= a_W + a_E + a_B + a_T + \beta_P\Delta V_P\lambda \end{aligned}$$

The advective transport can be included in several ways. Patankar recommends the use of a power-law interpolation function: A_{power}, such that we obtain the following coefficients; cf. [Pat80] p. 99 and [Lou87] p. 259:

$$a_W = Y_w A_{\text{power}}(\mathcal{P}_w) + \max(0, A_w q_w) \tag{70}$$

$$a_E = Y_e A_{\text{power}}(\mathcal{P}_e) + \max(0, -A_e q_e) \tag{71}$$

$$a_B = Y_b A_{\text{power}}(\mathcal{P}_b) + \max(0, A_b q_b) \tag{72}$$

$$a_T = Y_t A_{\text{power}}(\mathcal{P}_t) + \max(0, -A_t q_t) \tag{73}$$

$$b = \epsilon_P\Delta V_P G_P \tag{74}$$

$$a_P = a_W + a_E + a_B + a_T + \beta_P\Delta V_P\lambda \tag{75}$$

where

q_w = bulk soil-gas flux density ($\hat{x}\cdot\vec{q}$) at w-interface, $\mathrm{m}^3/(m^2\,\mathrm{s})$

q_e = bulk soil-gas flux density ($\hat{x}\cdot\vec{q}$) at e-interface, $\mathrm{m}^3/(m^2\,\mathrm{s})$

q_b = bulk soil-gas flux density ($\hat{z}\cdot\vec{q}$) at b-interface, $\mathrm{m}^3/(m^2\,\mathrm{s})$

q_t = bulk soil-gas flux density ($\hat{z}\cdot\vec{q}$) at t-interface, $\mathrm{m}^3/(m^2\,\mathrm{s})$

The grid-Péclet numbers: $\mathcal{P}_w$, $\mathcal{P}_e$, $\mathcal{P}_b$, and $\mathcal{P}_t$ indicate the relative importance of the advective and diffusive flux densities:

$$\mathcal{P}_w = \frac{A_w q_w}{Y_w} = q_w\frac{(\delta x)_w}{D_w} \tag{76}$$

$$\mathcal{P}_e = \frac{A_e q_e}{Y_e} = q_e\frac{(\delta x)_e}{D_e} \tag{77}$$

$$\mathcal{P}_b = \frac{A_b q_b}{Y_b} = q_b\frac{(\delta z)_b}{D_b} \tag{78}$$

$$\mathcal{P}_t = \frac{A_t q_t}{Y_t} = q_t\frac{(\delta z)_t}{D_t} \tag{79}$$

The powerlaw interpolation function is:

$$A_{\text{power}}(\mathcal{P}) = \max(0, (1 - 0.1|\mathcal{P}|)^5) \tag{80}$$

3.2 Model implementation

The model, named **Rnmod2d.pas** is programmed in the computer-language Pascal and consists of app. 2000 lines of code. The model has been run on personal computers and on the VAX-8700 at Riso National Laboratory. On a personal computer the model handles grids with up to 10000 nodes.

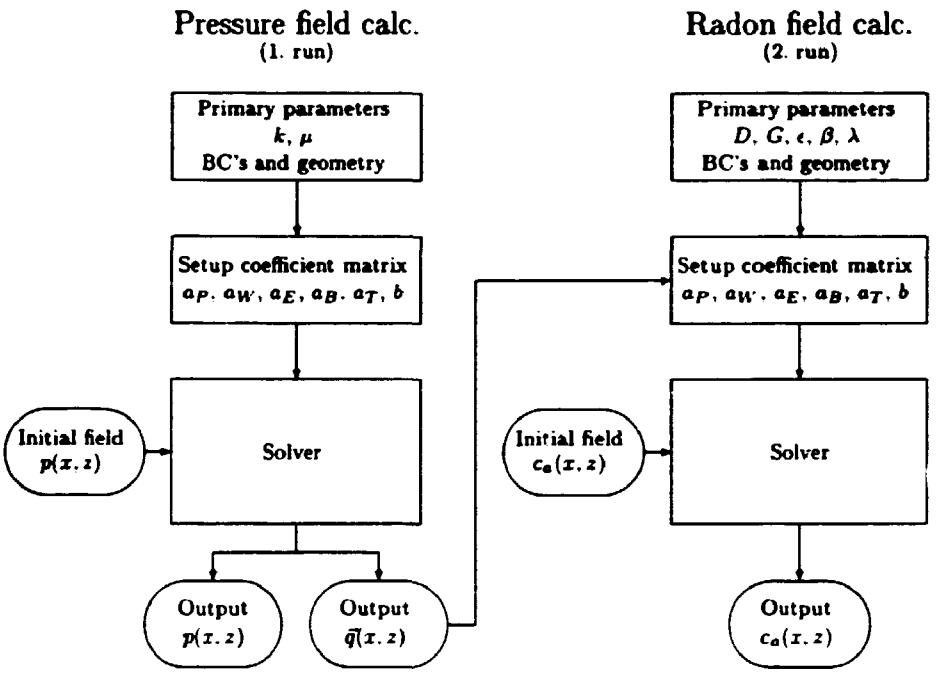

Figure 2. Overview of the computational procedure used in **Rnmod2d.pas**. *BC is short for boundary condition.*

As illustrated in figure 2, two model runs are needed to solve the transport equations. In the first run, the soil-gas problem is solved. The job specification involves: values for soil permeability, viscosity, boundary conditions, grid definition, and physical dimensions of the problem. The program sets up a coefficient matrix and initiates the iterative solution procedure (if a similar field problem has been solved previously, that field might be imported in order to speed up computations). Iterations are stopped when selected criteria for convergence are met. The pressure field and the soil-gas fluxes between nodes are stored onto separate files with other types of output useful for documentary purposes, post-processing or graphical presentation. The radon concentration field is found in a second model run. This time, the job specification includes: values for diffusivity, radon generation rate, porosity, partition corrected porosity (β), decay constant and directions concerning how to import the soil-gas flux between nodes as calculated in the first run. Again, the coefficient matrix is set up and the solution is found. Appendix A contains one example of a job specification file.

Figure 3 sketches the computational plane. The 'house' is located in the upper left corner of the grid. Soil gas and radon enter through the boundary sections named BC_cen (i.e. center crack), BC_per (i.e. perimeter crack), or BC_wall (i.e. wall crack). The boundary sections named: BC_atm and BC_wat represent the at-

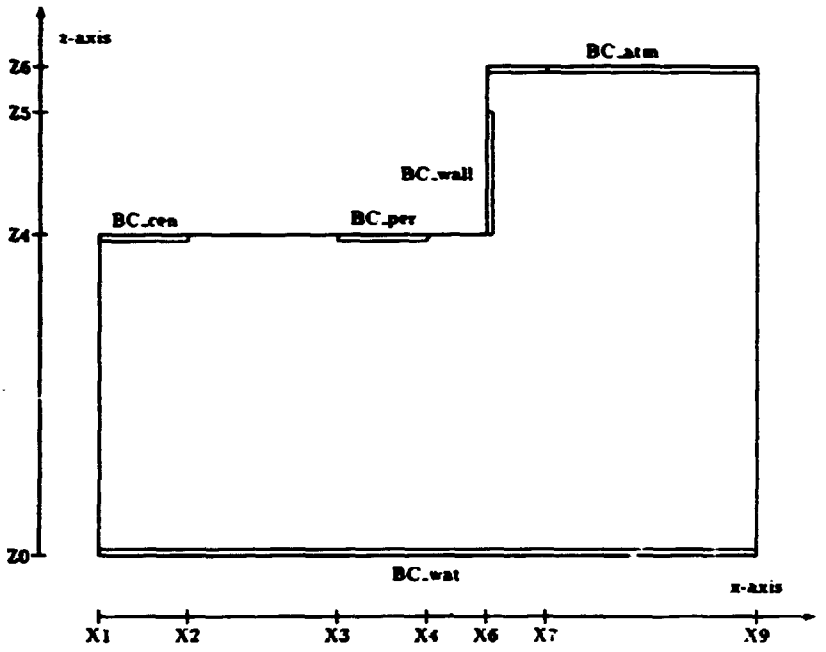

Figure 3. Outline of the computational plane and location of optional boundary conditions.

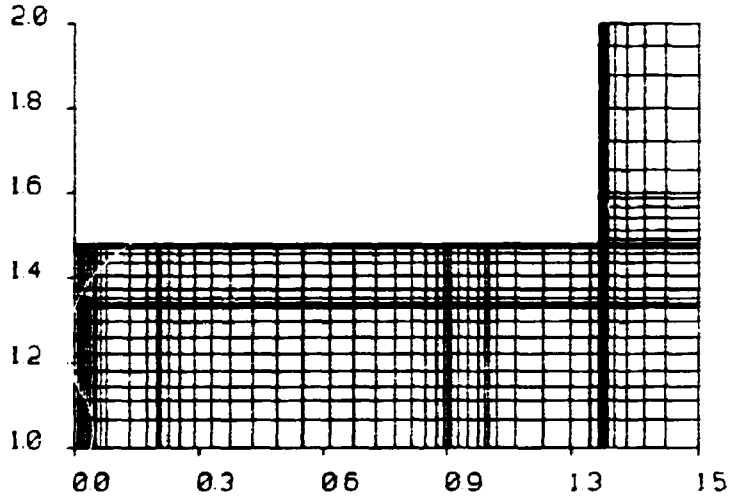

Figure 4. Part of the computational grid used in the calculations of radon entry into the radon test structure described in chapter 4.

mospheric surface and the water table, respectively. The named boundary sections fulfill optional boundary conditions of the Neumann ('no-flow') or Dirichlet type ('constant concentration'). In addition, special conditions that simulate ventilation and the accumulation of radon inside the 'house' can be applied at BC_cen, BC_per, and BC_wall. The other parts of the boundary fulfill Neumann conditions. The physical dimensions of the grid are specified through the constants shown in figure 3: X1 to X9 and Z0 to Z6. It is thereby possible to deform the computational plane for calculations of a variety of field problems related to radon entry into real houses, our test structure, or soil probes. The distribution of control volumes is

important in calculations where high gradients occur, and the model is supplied with a general set of functions such that the volumes can be distributed in an appropriate way. Figure 4 shows part of a grid used in the calculation of entry into the test structure described in chapter 4.

The model has been subject to a number of tests concerning the mathematical correctness of the programmed model. The verification has focused on the ability of the model to solve two-dimensional heat-flow problems for which solutions are known. The main source for these comparisons have been analytical solutions for simple geometries and model calculations obtained with a commercial heat-flow program based on the finite-element method. The ability of the model to simulate radon transport has been verified for a number of one-dimensional problems for which exact solutions were known; for example transport through two layers of soil having different properties and combined diffusive and advective transport through a single layer of soil.

4 Model verification

In the preceding two chapters, we have presented a model that provides a mathematical description of transport of soil gas and radon in soils. In this chapter, we focus on the physical validity of the model and describe the results of a verification exercise grounded on the comparison of *experimental results* with *model calculations* based on *measured soil parameters*. The experimental results come from a newly established radon test structure located at Risø National Laboratory. The chapter contains five sections: Firstly, we describe the location and design of the test structure. Thereafter, we present results from steady-state experiments. Pressure couplings and radon concentrations have been measured in 19 soil probes located in the vicinity of the structure. The radon concentrations have been measured under conditions where the transport was mainly diffusive or advective. Section 4.3 describes the measured soil parameters: porosity, density, radon emanation rate, permeability, and moisture content. Finally, in section 4.4 and 4.5 we describe results from model calculations for different sets of parameters and compare the modelling results with those of the experiments.

4.1 Structure location and design

The aim of the test structure design has been to establish an experimental facility[8] such that the transport and entry of soil gas and radon can be studied under field conditions where:

- The soil is typical for Danish surface geology.
- The building shell is simple and relatively well-defined.
- The entry rates of soil gas and radon can be measured directly.
- The main driving forces can be controlled and will not be influenced by house occupants.

The structure is located at Risø National Laboratory approximately 60 m west of the Chemistry department and 4-5 m above sea level. The surface is almost horizontal with a minor slope (down) towards south-west. Prior to the construction, the field site was covered with grass. A group of bushes and smaller trees 6 m west of the structure provides some shelter for the wind. The water table is found at a depth of approximately 2 m. This particular field site was selected out of a few possible locations at Risø National Laboratory. Initial soil investigations indicated the site to have a sufficiently high permeability ($\sim 4 \cdot 10^{-12}$ m^2) and radon concentration to be appropriate for a study of this type.

A cross-sectional view of the test structure is shown in figure 5. It consists of a 40 liter, stainless-steel cylinder placed in a 0.52 m deep quadratic excavation with a side length of 2.4 m. The excavation is lined with an airtight 0.6 mm pvc membrane that is attached to the cylinder. A layer of bentonite fills the interface region between the soil and the membrane. The membrane is kept in place by fine gravel backfilled into part of the excavation. Radon enters the cylinder through a changeable interface in the bottom. For example, the interface may consist of a cylindrical sample of cracked concrete mounted in a special holder of diameter 10 cm and height 20 cm. In the experiments reported here, radon simply enters the cylinder directly through a hole of 9.5 cm in diameter. Below the membrane, a capillary breaking layer of highly permeable gravel has been placed. This layer has

[8] Larger, basement-like test structures have been constructed and are being used for studies of soil-gas and radon entry at Colorado State University, Ft. Collins and at Lawrence Berkeley Laboratory; [Bor91], [Fisk89], [Sext91].

a thickness of 0.15 m and a side length of 1.6 m. The permeability of the gravel has been measured in the laboratory to be $4 \cdot 10^{-9}$ m^2.

A shelter for instrumentation is placed on top of the backfilled gravel. Easy access to the cylinder can be obtained through a hatch in the floor. A data acquisition system samples instrumental data every 10 minutes. The instrumentation includes: 2 continuous radon monitors, 2 differential pressure gauges, 6 thermometers, and gauges for wind and rain. One of the continuous radon monitors is connected to the cylinder in a closed loop. A small fan mixes the air inside the cylinder.

The cylinder is depressurized with an electronically controlled mass-flow controller unit and a pump. A reference probe for the pressure measurements is located in the backfilled gravel within the excavation.

In the vicinity of the structure a total of 26 pvc probes[9] of 1.7 cm in inner diameter have been installed as part of a site characterization project undertaken by the Technical University of Denmark (DTH): [Dam91]. Moreover, two simple probes are located in the gravel below the cylinder. Most probes are pair-wise located symmetrically on the east-west or north-south sides of the structure such that, for example, all east probes, E1 to E6, have corresponding probes on the west side, W1 to W6. Six of the probes are located below the structure: M1 to M6, of which M1 and M6 are in the gravel. Figures 5 and 6 show the probe locations. The probes serve several purposes: Firstly, drilling the probe holes provided samples for measurements by DTH of radon emanation rates (E) and content of moisture (W) and for a general characterization of the site geology. Secondly, in-situ permeability measurements were made by DTH using a simple 15 cm probe head that fits into the probe holes: [Dam91]. Finally, we use the probes for mapping pressure and radon fields manually. All probes are sealed off when not in use.

4.2 Experimental results

During the period from April 9 to August 30, 1991, different types of steady-state experiments have been conducted at the radon test structure. We report the results of these experiments in the following.

Soil-gas entry rates

The relationship between steady-state depressurization and soil-gas entry rate into the cylinder (i.e. the flow resistance, $\Delta p/Q$) has been investigated on three occasions: April 9, July 25, and August 10, 1991. The first series of measurements took place (under slightly primitive conditions) only a few days after the test structure was established[10]. In the other two series, the flow resistance was found during short-term experiments where the cylinder was depressurized to values in the range of 0 to 30 or 60 Pa. The depressurization was measured with an inclined micromanometer and/or a low-range differential pressure transducer (FCG-40, from *Furness Controls Limited*). The flow rates were measured with ordinary rotameters. For the three measurements we obtained the following linear flow resistances: $1.5 \cdot 10^5$, $1.5 \cdot 10^5$, and $1.2 \cdot 10^5$ Pa s m^{-3}, respectively. The precision of the values is at the order of 15%.

Pressure couplings

The pressure couplings of the probes have been measured with the cylinder depressurized to 30 Pa or 60 Pa. We define the pressure coupling at a given probe

[9] 'Pipe-end probes'.

[10] At that time, the cylinder was in place and gravel had just been backfilled into the excavation. The shelter for instrumentation had not been built yet.

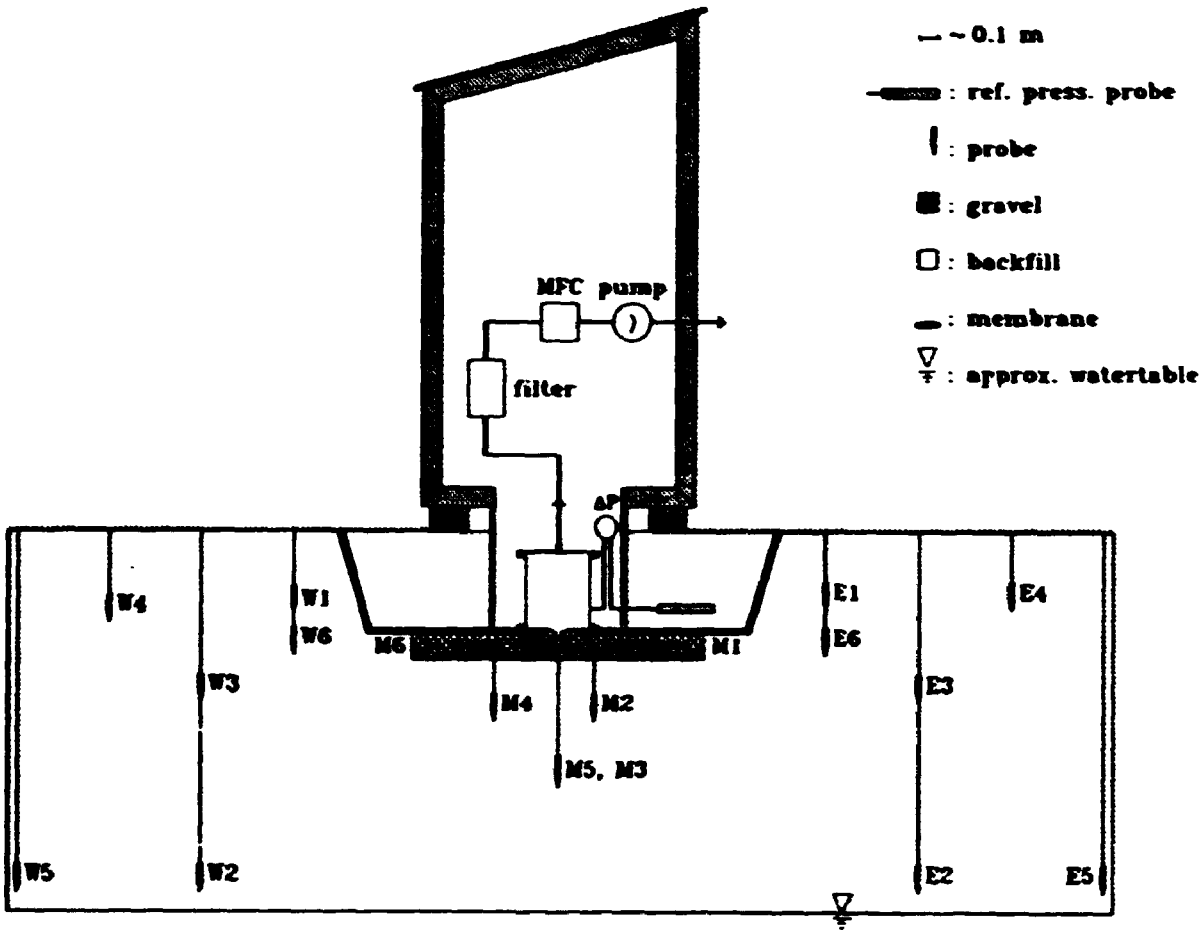

Figure 5. Cross-sectional view of the radon test structure.

location as p_{probe}/p_{cyl}, where p_{probe} is the measured pressure difference between the atmosphere (or the reference probe) and that particular probe. p_{cyl} is the pressure difference from the atmosphere (or the reference probe) to the cylinder. Table 2 lists the measured pressure couplings. The indicated uncertainties of the measurements are observed standard errors based on 3 to 5 measurements conducted at different times and/or with different types of pressure gauges. The table shows that the probes located below the membrane (M1 to M6) are well coupled with values from 75 to 100 %. The other probes have couplings less that 20 %. This series of measured pressure couplings is named Pr0, where 'Pr' stands for pressure couplings and '0' for experimental results. The corresponding model calculations are named Pr1, Pr2, and Pr3.

Radon concentrations

The results of three steady-state radon experiments are given in appendix B and summarized in table 2. In the first experiment (exp. 1), the pump was disconnected, so that no depressurization was applied. In the two other experiments (exp. 2 and exp. 3), the cylinder was depressurized to 8±2 Pa and 13±2 Pa respectively. This was achieved by (imposed) flow rates of 3.3±0.6 $\ell\,min^{-1}$ and 5.2±0.6 $\ell\,min^{-1}$, respectively. Conventional scintillation cells of 150 or 170 ml were used

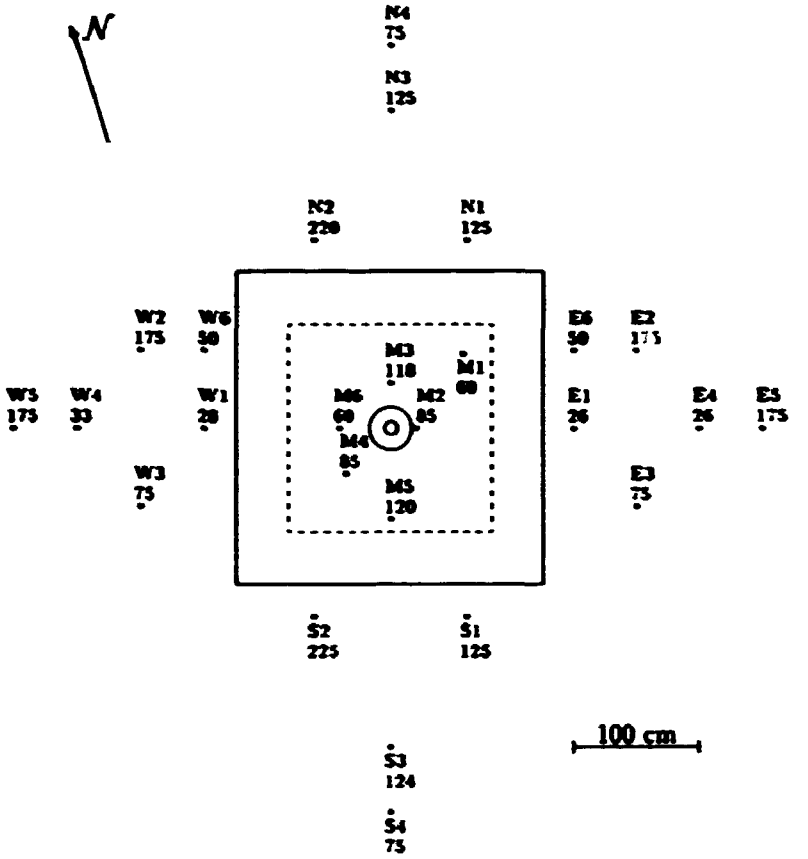

Figure 6. Outline of the field site where the radon test structure is located. The depths of the probes are given in cm. The dashed square indicates the gravel layer located below the membrane. The inner circle is the entry hole to the cylinder.

for the measurements of radon concentrations in the probes and in the cylinder.

Table 2 shows that most probe locations are partly depleted for radon in response to the imposed flow of soil gas. We define the degree of radon depletion shown in column 5 of table 2 as:

$$\frac{c_d - c_a}{c_d} \tag{81}$$

where c_d and c_a are the concentrations measured in one particular probe under diffusive and advective conditions, respectively. In section 4.5 we compare the results obtained in exp.1 and 3 with model calculations, and it is therefore convenient to introduce the following notation: Experiment 1 is named Di0, where 'Di' symbolizes that the transport was mainly diffusive; i.e. no forced flow was imposed. '0' stands for experimental results. Experiment 3 is named Ad0, where 'Ad' is for advection. The corresponding model calculations are named Di1, Di2 ... Di5 and Ad1, Ad2 ... Ad5. Experiment 2 is not used in the verification test and the results are only listed here for completeness.

4.3 Soil parameters

In the following, we summarize the soil parameters made available to this project mainly through a site characterization project undertaken by the Department of Electrophysics, the Technical University of Denmark (DTH) and partly financed by the Commission of the European Communities.

Table 2. Main results from steady-state experiments.

Location	Radon concentration			Radon depletion	Press. coupling
	exp. 1 Di0 kBq m^{-3}	exp. 2 kBq m^{-3}	exp. 3 Ad0 kBq m^{-3}	(exp. 1.3) %	Pr0 %
Cyl.	45.6±2	12.2±1	9.6±1	79±5	100
M1	42.4±2	9.6±1	6.5±1	85±6	89±1
M2	48.3±1	20.7±1	14.3±1	71±3	91±1
M3	58.5±1	46.9±2	45.0±1	23±2	75±1
M4	54.6±2	23.5±1	20.3±1	63±4	84±1
M5	58.3±2	30.5±1	28.8±1	51±4	81±2
M6	44.4±1	14.6±1	11.5±1	74±5	92±1
W1	27.6±4	8.3±1	7.4±1	73±16	15±4
E1	22.8±3	6.3±1	5.6±1	75±17	8.6±1
W2	48.2±1	43.8±2	50.1±1	-4±2	8.6±2
W3	37.0±4	31.8	24.4±1	34±10	5.9±2
E3	26.7±3	20.7±1	16.9±1	37±10	1.4±0.1
W4	20.8±2	18.2±1	14.7±1	30±9	1.3±0.4
E4	19.2±3	16.9±1	14.8±1	23±14	0.5±0.2
W5	55.0±1	49.8	51.9±1	6±2	4.1±0.6
W6	28.2±3	11.7±1	9.3±1	67±12	10±1
E6	23.9±2	4.7±1	4.8±1	80±12	11±3
N1	47.1±1	45.5±1	41.6±2	12±4	15±1
N3	57.7±1	72.1±1	63.0±1	-9±3	5.3±0.4
N4	24.9±2	(63.6)	27.4±2	-10±12	1.5±1

Geology; [Kors91]

Based on analysis of smal. soil samples from the borehole drilling. the site geology is characterized as follows: The uppermost 0.4 to 0.5 m consists of soil composed mainly of organic matters and sand. The layer contains many minor stones and fragments of carbonateous shells. The content of sand. stones and fragments of shells indicates that the site area is covered by an ancient beach from the time of the Litorina sea[11] about 6000 years ago. Due to farming activities during many years the upper 0.3-0.4 m are mixed by ploughing. Below 0.50 m. the site is dominated by moraine deposits of sandy clay[12]. A number of inhomogeneities are observed. For example. deposits dominated by sand are found outside the moraine clay layer 0.4 m from the excavation.

Porosity, density, and moisture content

Two soil investigations have been conducted:

Soil investigation A; [Fro91] Small soil samples of app. 3 g from the boreholes have been analysed for content of moisture. 25 samples from depths in the range of 30 to 170 cm had an average moisture content (W) of 11.4±0.4 %. The indicated uncertainty is the observed standard error. The values ranged from 5.5 to 15.3 %.

[11] In Danish: 'Stenalderhavet'.

[12] Moraine is a glacial deposit of till. i.e. an unconsolidated sediment containing all sizes of fragments from clay to boulders: [Pres86]. p. 638. According to [Fred90] 'Moræne ler' (Danish) should be translated to English as 'Clayey till'.

Soil investigation B; [Sog91] 8 soil samples of app. 150 ml have been collected from a separate excavation made 6-10 m north of the test structure. The samples have been analyzed for moisture, porosity, and density. A sharp-edged ring of aluminium was used for the sampling. The ring was forced horizontally into the wall of the excavation, and the soil sample was carefully transferred from the ring to a plastic beaker of the same diameter (7.7 cm) with an appropriate piston. The moisture content was found by drying the samples in an oven with a controlled temperature of either 60 or 550 °C The porosity was found by measuring the amount of water needed to saturate the dried samples. It was verified that the total volume of the sample was the same before and after saturation with water. Table 3 lists the results of samples taken at depths in the range of 15 to 85 cm. The average total porosity and moisture content were 0.53±0.02 % and 13±1 %, respectively. The indicated uncertainties are observed standard errors.

Table 3. Soil investigation B: Soil parameters measured in 8 samples taken at depths from 15 to 85 cm. ρ_{wet} is the (wet) soil density. ϵ_a, ϵ_w, and ϵ are air, water, and total porosities, respectively. W is the moisture content and m is the fraction of water saturation.

	ρ_{wet} $g\,cm^{-3}$	ϵ_a -	ϵ_w -	ϵ -	W %	m %
mean	1.36	0.35	0.17	0.53	13	32
st.dev.	0.2	0.03	0.03	0.04	3	5.3
min.	1.2	0.30	0.10	0.46	9	21
max.	1.8	0.39	0.21	0.57	17	37

Permeability; [Dam91]

Permeability has been measured in-situ using a 15 cm probe head that fits into the pvc probes described on page 21: [Dam91]. The method is based on the assumption that the soil is homogeneous and isotropic. Figure 7 shows the results of 16 measurements. The indicated depths correspond to the midpoints of the probe heads. It is seen that the permeability varies over four orders of magnitude. The permeability of the top layer (0-50 cm) ranges from $7 \cdot 10^{-14}$ m^2 to $1.4 \cdot 10^{-11}$ m^2, whereas the permeability of the bottom layer (50-200 cm) is from $2 \cdot 10^{-15}$ m^2 to $3.7 \cdot 10^{-12}$ m^2. The median permeabilities for the two layers are $4.5 \cdot 10^{-12}$ m^2 and $1.5 \cdot 10^{-12}$ m^2, respectively.

Emanation; [Fro91]

Emanation of radon has been measured in the laboratory using soil samples of app. 30 g collected from boreholes according to the following procedure: The (undisturbed) soil sample is located in a 160 ml radon-tight container with an alpha track film. The container is divided into two compartments by a thin membrane (11.5 μm). The membrane separates the soil sample and the track film. The purpose of the separation is to stop thoron that might emanate from the soil, and to prevent moisture from disturbing the exposure of the film. The film is exposed for app. 20 days. The method is based on the assumption that all radon that emanate into open pores escape the sample (by diffusion). The method does not account for the partition of radon between gas and liquid phases. However, because of

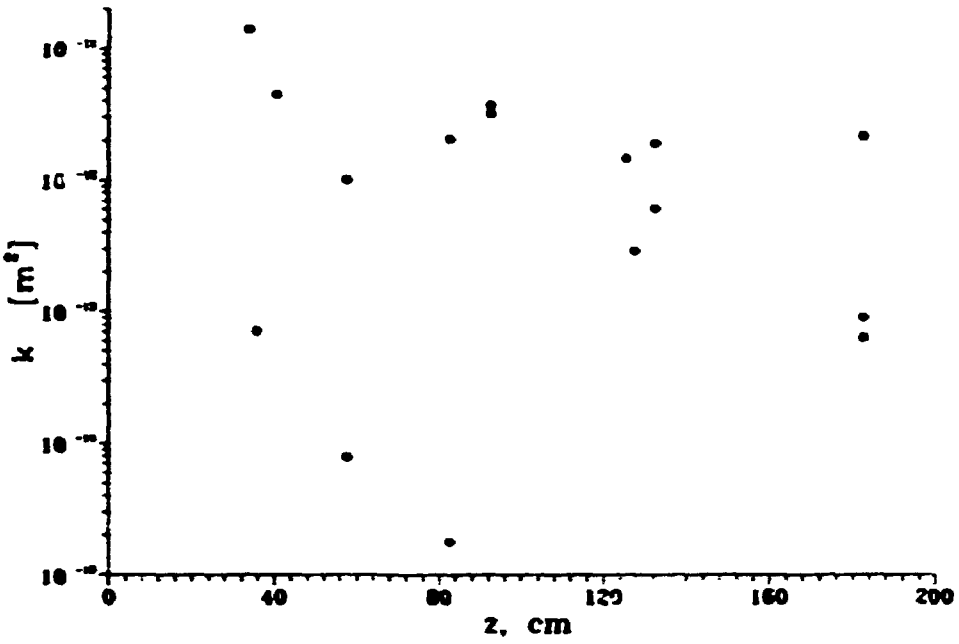

Figure 7. Permeability measurements in 16 locations as a function of depth: [Dam91].

the large volume of the container it might be reasonable to assume that radon dissolved in the soil water can be neglected.

Figure 8 shows the results of 81 emanation measurements as a function of depth. The average emanation rate (E) is 9.7±0.5 atoms $kg^{-1} s^{-1}$. A linear regression analysis of emanation rate versus depth (z, m) gives the following coefficients ($E = az+b$): a = -4.6±0.8 atoms $kg^{-1} s^{-1} m^{-1}$ and b = 14.1 ± 0.9 atoms $kg^{-1} s^{-1}$. The indicated uncertainties are observed standard errors. The regression analysis gives a correlation coefficient of -0.54. During the measuring period, the samples lost part of their moisture content (<25%), which might cause some bias in the reported emanation rates.

Selection of modelling parameters

Based on the site characterization we make the following three comments: (1) It is necessary to convert some of the measured parameters to those needed in the mathematical formalism: e.g. the measured emanation rates (E) in atoms $kg^{-1} s^{-1}$ must be converted to generation rates (G) in Bq $m^{-3} s^{-1}$. In short, the following soil parameters are needed in the model calculations: permeability (k), partition corrected porosity (β), bulk diffusion constant (D), and radon generation rate (G). (2) The present situation is not exactly ideal for model verification purposes since some of the parameters are distributed over a wide range of values (k) or have only been measured for the top part of the soil (ρ_w, and ϵ). Because of these limitations, it is necessary to pursue a line of attack aimed to demonstrate if experimental results agree with model calculations based on soil parameters that are 'reasonable', yet not necessarily equal to the mean values of the measurements. (3) The multidimensional nature of the involved parameter-space and the computational requirements in each field calculation make it necessary to limit the model calculations to selected combinations of parameters. The primary purpose

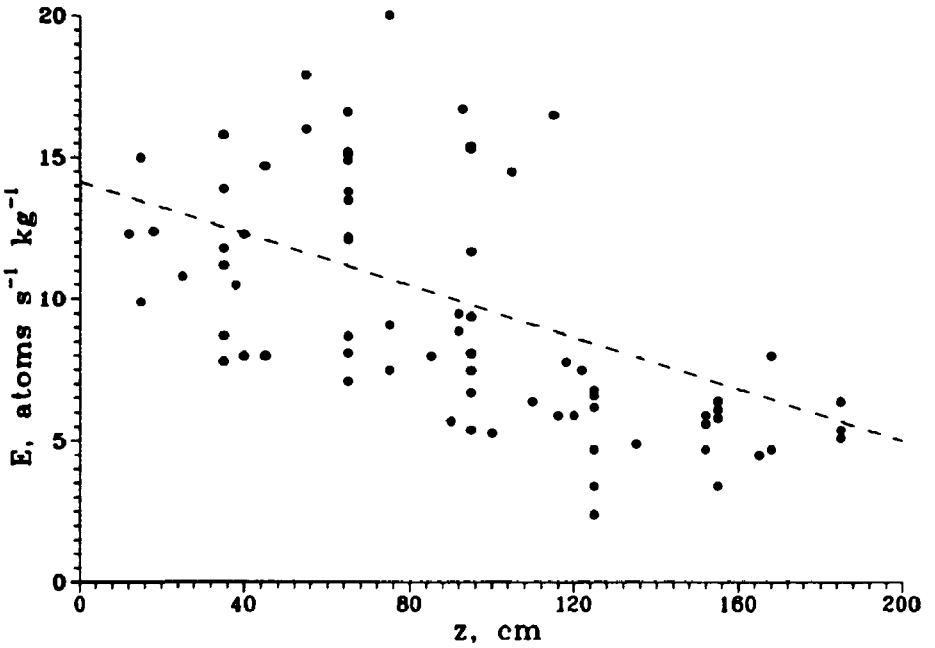

Figure 8. Measured emanation rates (E) from 81 soil samples; [Fro91].

of this section is to identify such combinations.

The geological characterization provides an important means for simplifying the parametric description of the soil. The analysis of soil samples showed that the top 40-50 cm of the soil was mainly sandy soil with organic matters whereas the region from 50 to 200 cm was dominated by (sandy) moraine clay deposits. We therefore divide the computational plane into two layers and provide the model with characteristic parameters for each of these[13].

Three sets of permeabilities are used in the model calculations: K1, K2, and K3. In the first set we assume the permeability of each layer to equal the median value of the permeability measurements; $4.5 \cdot 10^{-12}$ m^2 (0-50 cm) and $1.5 \cdot 10^{-12}$ m^2 (50-200 cm), respectively. In K2 we use maximum values of the measurements within each layer; $1.4 \cdot 10^{-11}$ m^2 and $3.7 \cdot 10^{-12}$ m^2, respectively. In the final set, we assume the permeability to be the same for both layers and that the value equals the highest of the measurements; $1.4 \cdot 10^{-11}$ m^2.

Two emanation rate profiles are used: E1 and E2. In the first profile, we use a constant value (for both layers) equal to the average of the measured radon emanation rates: $E = 9.7$ atoms kg^{-1} s^{-1}. In E2, we assume that the emanation rate takes the linear profile found in the regression analysis of the emanation rate measurements: $E = az + b$, where a= -4.6 atoms kg^{-1} s^{-1} m^{-1}, b= 14.1 atoms kg^{-1} s^{-1}, and z is the depth in m.

The remaining (basic) model parameters can not be selected independently of each other since they depend on soil density, porosity, and moisture content. For consistency, we therefore calculate values of β, D, and $G/(\lambda E)$ from given values of ρ_{ws}, ϵ, and W. The expressions for the derived model parameters are repeated here for completeness:

$$\epsilon_w = W\frac{\rho_{ws}}{\rho_w}$$

[13]In addition, separate parameters are assigned to the gravel layer located below the membrane.

$$\epsilon_a := \epsilon - \epsilon_w$$

$$m = \frac{\epsilon_w}{\epsilon}$$

$$\beta = \epsilon_a + L\epsilon_w$$

$$D = \beta D'_e$$

$$G = \frac{1-W}{\epsilon}\rho_{ws}\lambda E$$

We estimate the effective diffusion constant (D'_e) from the empirical expression found by Rogers and Nielson; [Rog91B]:

$$D'_e = D_0 \epsilon \exp(-6m\epsilon - 6m^{14\epsilon}) \tag{82}$$

where D_0 is the diffusion constant of radon in free air (app. $1.1 \cdot 10^{-5}$ $m^2 s^{-1}$).

Table 4. Characteristic properties for Danish moraine sand and moraine clay: [Har84]. ρ_g and ρ_{ws} are grain and (wet) soil densities, respectively.

Moraine type	ρ_g $g\,cm^{-3}$	ρ_{ws} $g\,cm^{-3}$	ϵ -	ϵ_w -	W %	Clay frac. % (mass)
sand	2.65 - 2.7	2.2 - 2.3	0.17 - 0.29	0.0 - 0.29	0 - 13	<10 - 15
clay	2.67 - 2.73	2.1 - 2.3	0.23 - 0.33	0.19 - 0.33	9 - 14	20 - 25

Table 5. Soil parameters calculated from given values of ρ_{ws}, W, and ϵ. The top part of the table defines the parameter sets named: S1, S2, and S3. The bottom part shows the sensitivity of the modelling parameters to changes in ρ_{ws}, W, or ϵ. L=0.3.

ID	ρ_{ws} (a)	W -	ϵ -	m -	β -	D'_e (b)	D (b)	$\frac{G}{\lambda E}$ (c)	$\frac{G'}{\lambda E}$ (c)	ρ_{sol} (a)	L_d m
S1	1.36	0.114	0.53	0.29	0.42	2.30	0.97	2.27	2.86	2.56	1.05
S2	1.36	0.114	0.28	0.55	0.17	0.67	0.12	4.30	7.03	1.67	0.57
S3	2.20	0.114	0.28	0.90	0.10	0.01	0.001	6.96	18.66	2.71	0.08
	1.09	0.114	0.53	0.23	0.44	2.77	1.23	1.82	2.18	2.05	1.15
ρ_{ws}	1.36	0.114	0.53	0.29	0.42	2.30	0.97	2.27	2.86	2.56	1.05
	1.63	0.114	0.53	0.35	0.40	1.91	0.76	2.72	3.61	3.07	0.95
	1.36	0.091	0.53	0.23	0.44	2.77	1.23	2.33	2.79	2.63	1.15
W	1.36	0.114	0.53	0.29	0.42	2.30	0.97	2.27	2.86	2.56	1.05
	1.36	0.136	0.53	0.35	0.40	1.92	0.77	2.22	2.93	2.50	0.96
	1.36	0.114	0.42	0.37	0.32	1.81	0.57	2.84	3.82	2.09	0.93
ϵ	1.36	0.114	0.53	0.29	0.42	2.30	0.97	2.27	2.86	2.56	1.05
	1.36	0.114	0.64	0.24	0.53	2.76	1.46	1.89	2.28	3.31	1.15

(a) $g\,cm^{-3}$; (b) 10^{-6} $m^2 s^{-1}$; (c) $Bq\,m^{-3}$ per $atoms\,kg^{-1}\,s^{-1}$

We use three sets of basic soil parameters: S1, S2, and S3. In S1, we use the measured (average) values of porosity and density of soil-investigation B: ρ_{ws}=1.36 g cm^{-3} and ϵ=0.53. In S3, we use literature values (table 4) for density and porosity characteristic for moraine clay[14]: ρ_{ws}=2.2 g cm^{-3} and ϵ=0.28. In S2, we apply the value of soil density found in soil investigation B (1.36 g cm^{-3}) and the porosity of 0.28. In all three sets, we use the value of water content of 11.4 % that was measured in soil investigation A. The three sets have been selected for the following reasons: S1 is a straightforward choice since it simply represents mean values of the measured parameters. However, the measurements come from the top 35 cm which is not necessarily representative for the bottom part of the soil. In fact, the geological characterization showed a clear difference between the region from 0 to 40-50 cm and the region from 50 to 200 cm. S3 has been selected as a possible substitute for soil parameters of the bottom layer which is dominated by moraine clay deposits. The justification for S2 is that it produces physical soil parameters that are in between the two other sets. Table 5 lists the three sets of the primary parameters (i.e. ρ_{ws}, W, and ϵ) and the subsequent values for m, β, D'_g, D, relative radon generation rates, diffusion length (L_d) and density of the solid part of the soil (ρ_{sol}). The latter is obtained as:

$$\rho_{sol} = \frac{1 - W}{1 - \epsilon} \rho_{ws} \tag{83}$$

If the soil is without organic matter, we would expect that ρ_{sol} approximately equals the density of the soil grains, which has a fairly constant value for a wide range of soils (app. 2.7 g cm^{-3}).

It can be seen from the table, that the three sets of parameters cover a wide range of physical situations. The water saturation (m) is 29 % for S1, 55 % for S2, and 90 % for S3. The diffusion length ranges from 8 cm for S3 to 1 m for S1. The relative generation rate vary by a factor of 6.5. Given a constant emanation rate of 9.7 atoms kg^{-1} s^{-1}, we have that S1, S2, and S3 predict deep-soil radon concentrations: $c_{a,\infty} = G'/\lambda$ of 28, 68, and 181 kBq m^{-3}, respectively.

The bottom part of table 5 illustrates the sensitivity of the derived parameters to changes in ρ_{ws}, W, and ϵ: The primary parameters are changed in turn by ±20 % from the values of S1. If we rank the parameters based on their impact on the relative radon generation rate ($G'/(\lambda E)$) and the diffusion length (L_d), we see that the porosity and the soil-density are (slightly) more important than the water content. Notice, that the calculated density for the solid part of the soil exceeds 2.7 g cm^{-3} for those of the calculations where porosity or soil density are set to maximum values.

In summary, we have identified the following sets of parameters: K1, K2, and K3 for permeability. E1 and E2 for emanation rate, and S1, S2, and S3 for the remaining (basic) soil parameters. Table 6 lists the selected combinations of parameters for which model calculations have been performed. The calculations of pressure couplings (and soil-gas flows) are named Pr1, Pr2, and Pr3 corresponding to K1, K2, and K3, respectively. The model calculations of radon concentration fields under diffusive conditions are named Di1 to Di5. Di1 represents the most important of the combinations since it is simply based on mean values of the measured parameters. In Di2 to Di4 the hypothetical values for the basic soil parameters (S2 and S3) are assigned to the bottom layer whereas S1 is unchanged for the top layer. In Di5 both layers are assigned the basic soil parameters of S2, which provides a means of reference for comparisons with Di1 that also has homogeneous soil parameters. The model calculations of the radon concentration

[14]It can be discussed if such a thing exists as 'typical moraine clay'. Firstly, moraine deposits are (per definition) inhomogeneous. Secondly, the properties depend on the degree of compaction of the soil, and finally, cracks might exist in moraine clays as discussed in [Fred90].

Table 6. List of model calculations.

ID	Job file	Type	Perm.	Eman.	Basic soilpar.	
					0-50cm	50-200cm
Pr1	Rn2_1100	Soil gas	K1			
Pr2	Rn2_1101	-	K2			
Pr3	Rn2_1102	-	K3			
Di1	Rn2_1110	Diff.		E1	S1	S1
Di2	Rn2_1115	-		E1	S1	S2
Di3	Rn2_1117	-		E2	S1	S2
Di4	Rn2_1116	-		E2	S1	S3
Di5	Rn2_1111	-		E1	S2	S2
Ad1	Rn2_1124	Advec.	(K2)	E1	S1	S1
Ad2	Rn2_1122	-	(K2)	E1	S1	S2
Ad3	Rn2_1125	-	(K2)	E2	S1	S2
Ad4	Rn2_1123	-	(K2)	E2	S1	S3
Ad5	Rn2_1120	-	(K2)	E1	S2	S2

fields under advective conditions are named Ad1 to Ad5. These calculations are based on the same parameters as Di1 to Di5 except for the imposed flowfield of soil gas. As indicated in the table we have based the flow field calculations on the permeabilities defined in K2. However, we have adjusted the depressurization applied in the model calculations such that the entry of soil gas into the cylinder equals that of the experimental situation (i.e. 5.2 $\ell\,\mathrm{min}^{-1}$).

All model calculations are based on a dynamic viscosity of μ=18 $\cdot$ 10^{-6} Pa s. and an Ostwald constant of: L=0.30. The gravel layer is assumed to be without moisture, and to have a porosity (ϵ) of 0.5 and a bulk diffusion constant (D) of $5 \cdot 10^{-6}$ $\mathrm{m}^2\,\mathrm{s}^{-1}$. The permeability of the gravel was measured in the laboratory to be $4 \cdot 10^{-9}$ m^2.

4.4 Modelling the test structure

In this section we present details connected to the application of the two-dimensional steady-state model described in chapter 3.

Computational plane

The physical water table was found to be located in a depth of app. 2 m ([Dam91]) and the computational plane therefore extends 2 m in the vertical direction. In the horizontal direction the computational plane is cut-off at 10 m from the center of the structure. Extending the plane further was found to have no significant influence on any of the reported results.

The model is applied in circular coordinates and the 'model structure' (centered at the z-axis) is forced to take a circular shape. Horizontal distances therefore have to be scaled appropriately. We select the scaling parameter such that the area of the gravel layer is the same for the physical and the model structure. The basis for this selection is that it provides the best possible estimate of the soil-gas entry rate into the structure. The cost is that the field is slightly deformed[15]. In general,

[15] An alternative mapping criteria is to set the radius of the model structure equal to the half side length of the physical structure.

a quadratic region (say, the gravel layer) with a side length of b, is mapped onto a circular region of radius r, where:

$$r = \frac{b}{\sqrt{\pi}} \tag{84}$$

such that the areas of the two regions are the same. The radius of the 'model gravel layer' is hence taken to be 1.6 m $/\sqrt{\pi} \simeq 0.90$ m. The radius of the model excavation is calculated in a similar fashion. However, the walls of the excavation are not vertical (see figure 5), and we therefore calculate the radius based on the mean side length[16] of 2.24 m: $r = 2.24$ m $/\sqrt{\pi} \simeq 1.26$ m. For consistency, we map the horizontal locations of the soil probes using the same scaling parameter.

The model calculations are conducted with a grid of 3024 nodes. The distribution of nodes was optimized through a series of subsequent grid refinements. The results obtained with the (standard) 3024-node grid have been compared with those obtained with a much larger grid of 9520 nodes. For the pressure and radon field calculations all primary output variables (fluxes at boundaries and radon concentrations within the cylinder) differed by less that 0.1 %. The calculated field values at probe locations as found by a simple bilinear interpolation function (from field values at neighboring nodes) typically differed less than 2 %.

Boundary conditions

The following boundary conditions are used in the calculations: In the pressure field calculation we assume the interior of the cylinder to take a specified value depending on the experiment (e.g. -13 Pa). The pressure at the atmospheric surface is set to 0 Pa. For the radon field calculation, we assume the radon concentration at the atmospheric surface to be zero Bq m^{-3}. In the cylinder, we assume that radon accumulates according to the following simple mass-balance equation:

$$J = (\lambda V_{cyl} + Q) c_{cyl} \tag{85}$$

where

Q = soil-gas flow through the cylinder, m^3 s^{-1}

J = radon entry rate into the cylinder, Bq s^{-1}

V_{cyl} = volume of cylinder, 0.040 m^3

c_{cyl} = radon concentration of the cylinder, Bq m^{-3}

c_{cyl} and J are found iteratively as part of the normal solution procedure applied to the computational nodes located in the soil. We assume Neumann (i.e no-flow) conditions for all other boundaries.

Modelling input

The input parameters are defined in table 6. Appendix A contains a sample job-file used in the radon field calculation named Ad1.

Modelling output

We calculate fluxes of soil gas and radon at all boundaries, including entry rates into the cylinder. Field values at the 19 probe locations are calculated with a bilinear interpolation technique; from the nearest four nodes of the computational plane; [Pres89]. Appendix C includes tables of computed field values for the 19 probe locations for all model calculations.

[16]The top and bottom side length measures are 2.40 m and 2.08 m, respectively. In its present form, the model cannot treat boundaries that are not horizontal or vertical.

Computed fields

Figures 9 to 13 show the computed fields of model calculation Pr3. Di1, and Ad1.

Figure 9 shows the flowfield as calculated in Pr3. Air enters the soil at the atmospheric surface and is drawn through the soil, the highly permeable gravel layer and finally into the depressurized cylinder. The flow is not distributed uniformly over the gravel layer. In fact, the figure indicates that the small region of soil extending from the gravel layer and to the edge of the membrane (i.e. where the footer of a real house would be) is a critical region since most soil-gas enters here. The corresponding pressure field of the same calculation is shown in figure 10. The depressurization of the cylinder is set to -100 Pa relative to the atmospheric surface where p=0 Pa. The figure shows that the pressure loss over the gravel layer is small (but not negligible) compared with that over the soil.

Figure 11 shows the radon concentration field under diffusive conditions as found in Dr1. As can be seen, the radon concentration builds up from 0 kBq m^{-3} at the atmospheric surface towards the level of saturation (c_∞=28 kBq m^{-3}). The figure also shows that the concentration below the center of the membrane is slightly higher than in the region of the same depth located directly below the atmospheric surface. Figure 12 shows the corresponding radon field with an imposed flow of soil gas (Ad1). The figure shows that forcing radon-free air into the ground depletes the vicinity of the structure of radon. Figure 13 shows the degree of depletion as calculated from equation 81 and Di1 and Ad1.

4.5 Comparison of experimental and modelling results

This section contains the comparison between the experimental results named Pr0. Di0. and Ad0. and the model calculations: Pr1 to Pr3. D1 to D5. and Ad1 to Ad5. The following aspects will be investigated:

- Soil-gas flow resistance
- Pressure couplings of soil probes: Pr1-Pr3 vs. Pr0
- Radon conc. in the probes under diffusive conditions: Dr1-Dr5 vs. Di0
- Radon conc. in the probes under advective conditions: Ad1-Ad5 vs. Ad0
- Degree of depletion of radon of the probes: Di1/Ad1-Di5/Ad5 vs. Di0/Ad0

For each of the field comparisons, we state coefficients of correlation (r) and regression (a and b) found by linear (or logarithmic) regression analyses based on calculated and measured field values at the 19 probe locations. For example, for the radon concentrations fields we obtain a regression line of the form:

$$c_p = ac_m + b \tag{86}$$

where c_p and c_m represent predicted (i.e. calculated) and measured radon concentrations, respectively[17]. We also state the average prediction-to-measurement ratio:

$$\mathrm{APMR} = \frac{1}{N}\sum_{i=1}^{N}\frac{c_p(i)}{c_m(i)} \tag{87}$$

where N is the number of probes (i.e. 19, unless otherwise specified).

[17] All regression analyses are unweighted: i.e. observed variations of measured values are neglected.

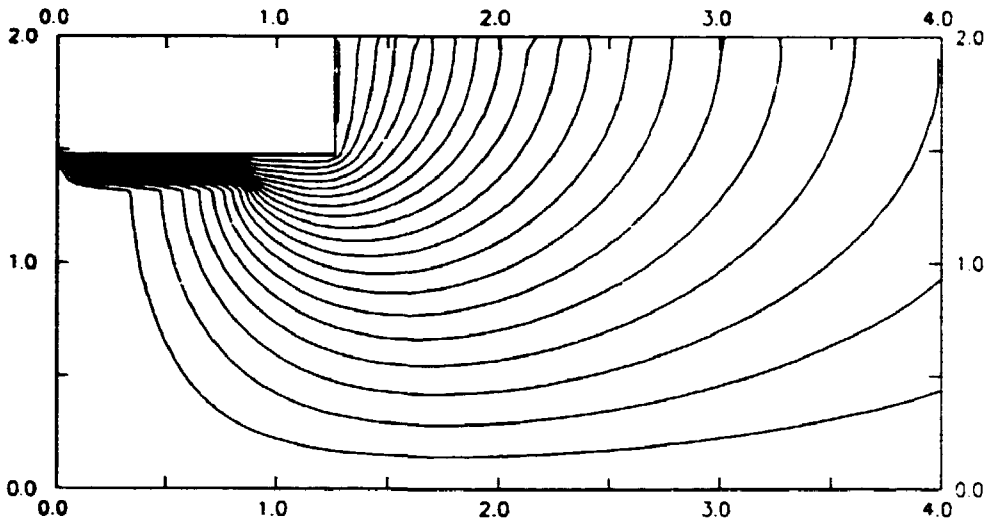

Figure 9. Streamlines (Pr3).

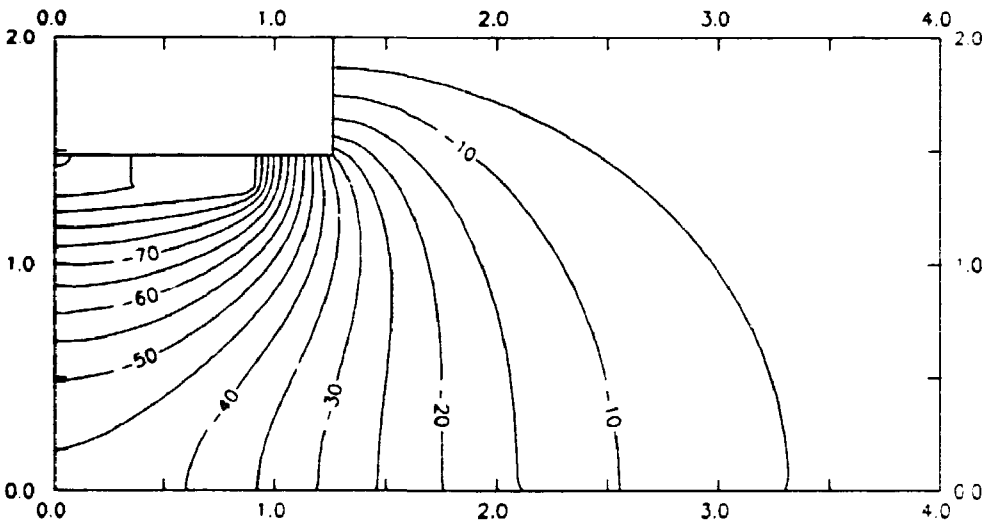

Figure 10. Pressure field (Pr3).

Soil-gas entry rates

Table 7 lists the calculated values of soil-gas flow resistances ($\Delta p/Q$) and the equivalent soil-gas entry rates at 10 Pa depressurization. Compared with the measured values of $1.2 \cdot 10^5$ to $1.5 \cdot 10^5$ Pa s m^{-3} (i.e. 5.2 to 4.1 ℓ min^{-1} at 10 Pa), we see that the model underestimates the entry of soil gas considerably. For example, based on the regional medians of the measured permeabilities (Pr1), the calculated soil-gas entry rate is underestimated by more than an order of magnitude. The best agreement is obtained for Pr3 where the permeabilities for the top and bottom regions are assumed to be equal to the overall maximum of the measured values ($1.4 \cdot 10^{-11}$ m^2); Pr3 gives a soil-gas entry rate that is app. 50 % lower than the measured value.

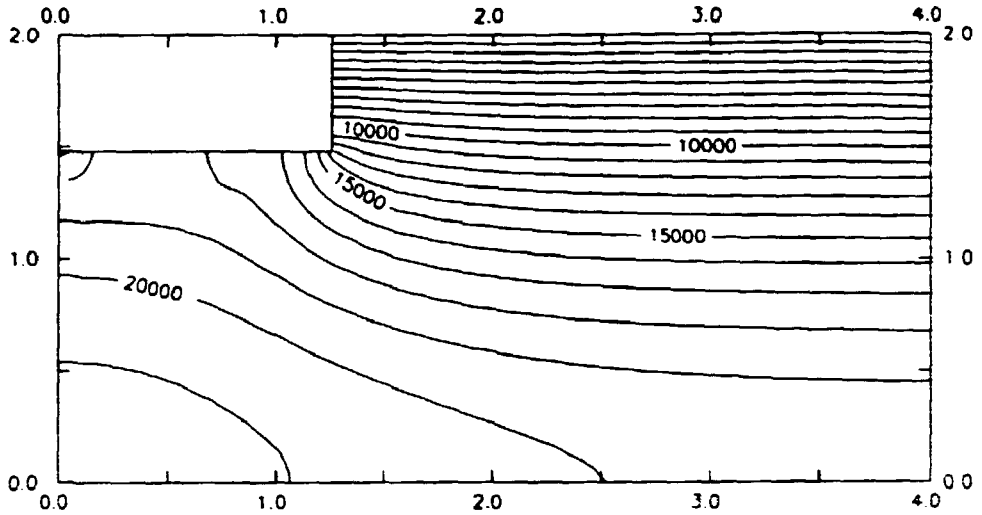

Figure 11. Radon concentration field under diffusive conditions (Di1).

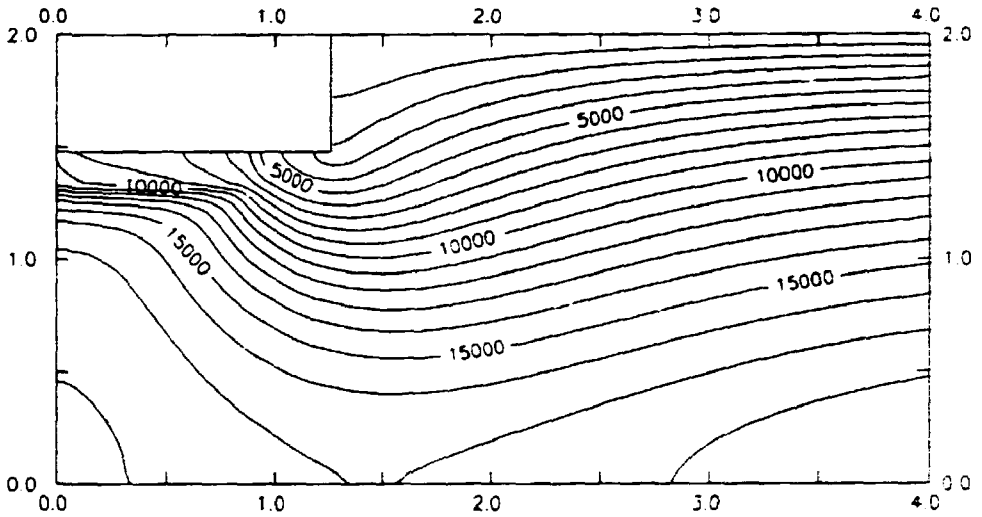

Figure 12. Radon concentration field under advective conditions (Ad1).

Table 7. Flow resistances and entry rates (Q).

ID	Flow resistance $Pa\,s\,m^{-3}$	Q at 10 Pa $\ell\,min^{-1}$	Remark
Pr1	$1.9 \cdot 10^6$	0.32	K1 (regional medians)
Pr2	$7.7 \cdot 10^5$	0.78	K2 (regional maxima)
Pr3	$2.5 \cdot 10^5$	2.41	K3 (overall maximum)

Pressure couplings

Figure 14 shows the measured and calculated pressure couplings for the 19 soil probes. It is seen, that there is a good overall agreement between measurements and modelling results. However, some discrepancies are observed. For example, the pressure couplings of the membrane probes: M2, M3, and M5 are underestimated

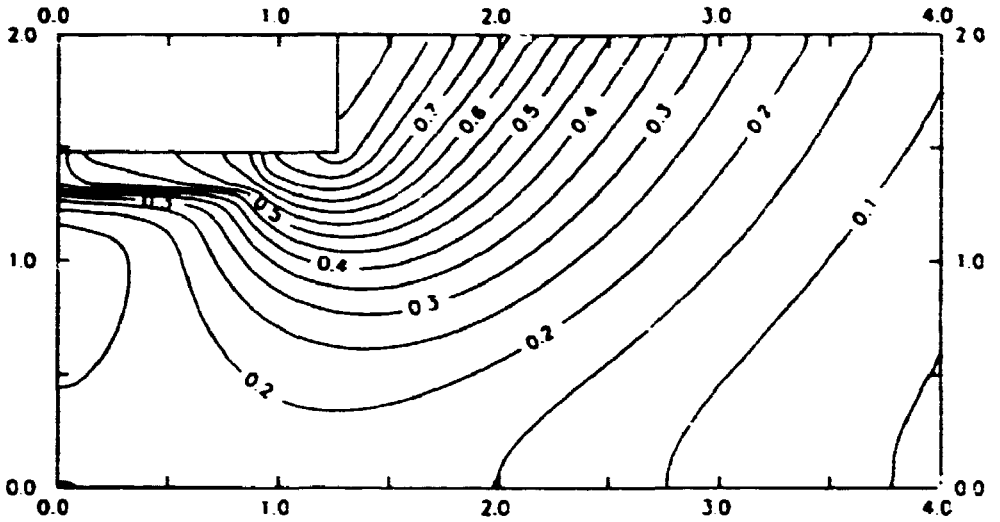

Figure 13. Radon depletion field calculated from equation 81 (Di1 and Ad1).

in all three model calculations. The pressure couplings of most of the probes located on the sides of the structure tend to be underestimated by Pr1 and Pr2 but overestimated in Pr3. Results of linear regression analyses are shown in table 8 on page 39. Since the pressure couplings are either relatively high (>70 %) or relatively low (<20 %), we conduct the regression analyses based on the logarithm of the pressure couplings. The correlation coefficients of the three model calculations are larger than 0.95, and the average prediction-to-measurement ratios range from 0.9±0.2 for Pr2 to 1.5±0.3 for Pr3.

Di1 to Di5 versus Di0

The top part of figure 15 shows the calculated radon concentrations of Di1 plotted versus the corresponding measurements (Di0). The linear regression analysis gives that the correlation is highly significant (r=0.91 and a=0.31±0.03) which indicates that the radon concentration *profile* under diffusive conditions is well described by the model. However, a large discrepancy exists between the *absolute* values of the calculated and measured radon concentrations: the average prediction-to-measurement ratio amounts to 0.39±0.02. Obviously, one or more of the soil parameters in Di1 related to the radon generation rate are incorrect. The parameters applied in Di1 predict a maximum radon concentration of c_∞ = 28 kBq m^{-3} (see table 5), whereas the measured radon concentrations for the deepest probes are at the order of 60 kBq m^{-3}. The radon generation depends on emanation rate (E), moisture content (W), porosity (ϵ), and soil density (ρ_{ws}). As discussed previously, we only have measured values for porosity and soil density for the top 85 cm of the soil, and the observed discrepancy therefore might be explained as a systematic error introduced because the measured values for porosity and soil density are wrongly assumed to represent the entire soil region.

The top part of figure 16 shows the calculated radon concentrations of Di2 versus those of the measurements (Di0). Di2 is based on the same soil parameters as Di1 except for the bottom layer (50-200 cm) where the parameters: D, G, and β are calculated from a hypothetical porosity of 0.28 (S2, see table 5). The average prediction-to-measurement ratio for the comparison of Di2 versus Di0 amounts to 0.82±0.08, which demonstrates that the agreement between calculations and measurements also might be extended to the absolute scale: the linear regression

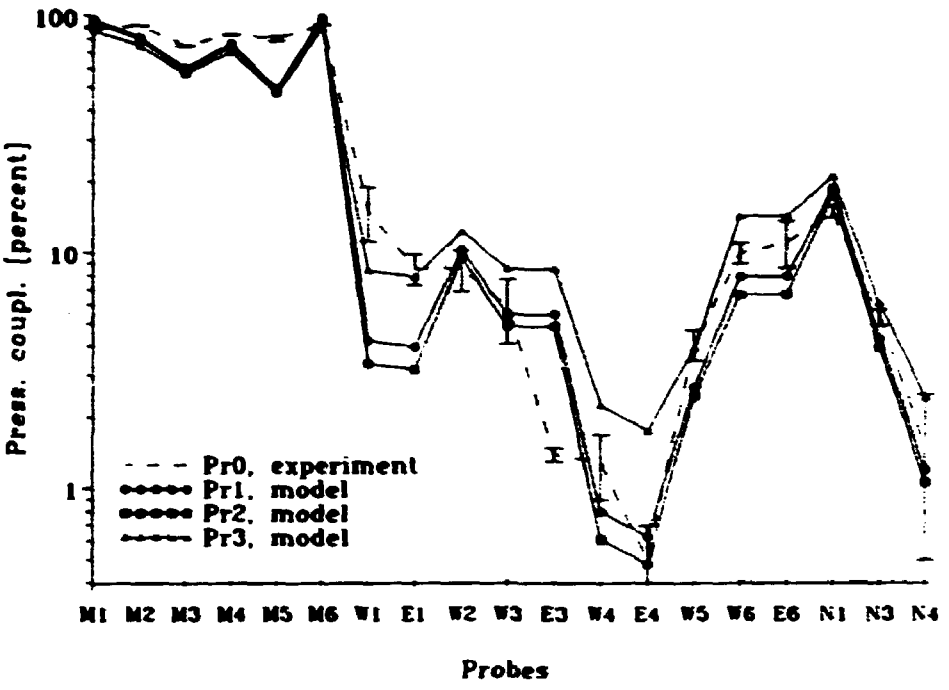

Figure 14. Pressure couplings measured (Pr0) and calculated (Pr1, Pr2, and Pr3) for the 19 probes. The indicated uncertainties of the measurements are observed standard errors based on 3 to 5 measurements conducted at different times or with different types of pressure gauges.

analysis of Di2 versus Di0 gives a correlation coefficient of 0.92 and a regression coefficient of a=1.27±0.1.

The difference between the parameters used in Di2 and Di3 is that Di2 is based on a constant emanation rate (E1) whereas Di3 is based on a linear profile (E2). It is seen from table 8. that these model calculations are quite insensitive to the choice of emanation profile.

In model calculation Di4. we have assumed the values for porosity and density for the region below 50 cm to equal typical values for moraine clay (S3): see table 4. This affects the relative radon generation rate and the diffusion constant considerably. The corresponding radon generation rate gives radon concentrations of the deepest probes of app. 180 kBq m^{-3}. which is much higher than the measured values (APMR=2.7±0.5). Moreover. the correlation coefficient between calculated and measured values is only 0.50.

Model calculation Di5 is based on homogeneous soil parameters equal to those specified in the parameter set named S2. It is seen from table 8 that the calculated radon concentrations are larger than the measured values (APMR=1.3±0.08) and that the correlation coefficient amounts to 0.80.

Ad1 to Ad5 versus Ad0

The mid part of figure 15 shows the calculated radon concentrations of Ad1 versus the measured values (Ad0). It is observed. that the points are somewhat more scattered compared with the situation for the diffusion dominated field (Di1 vs. Di0). which is reflected in a lower correlation coefficient of r=0.81. Relative to the regression line. the main outliers are M2. M3. and M5 where the radon concentrations are overestimated and N3 where the radon concentration is underestimated.

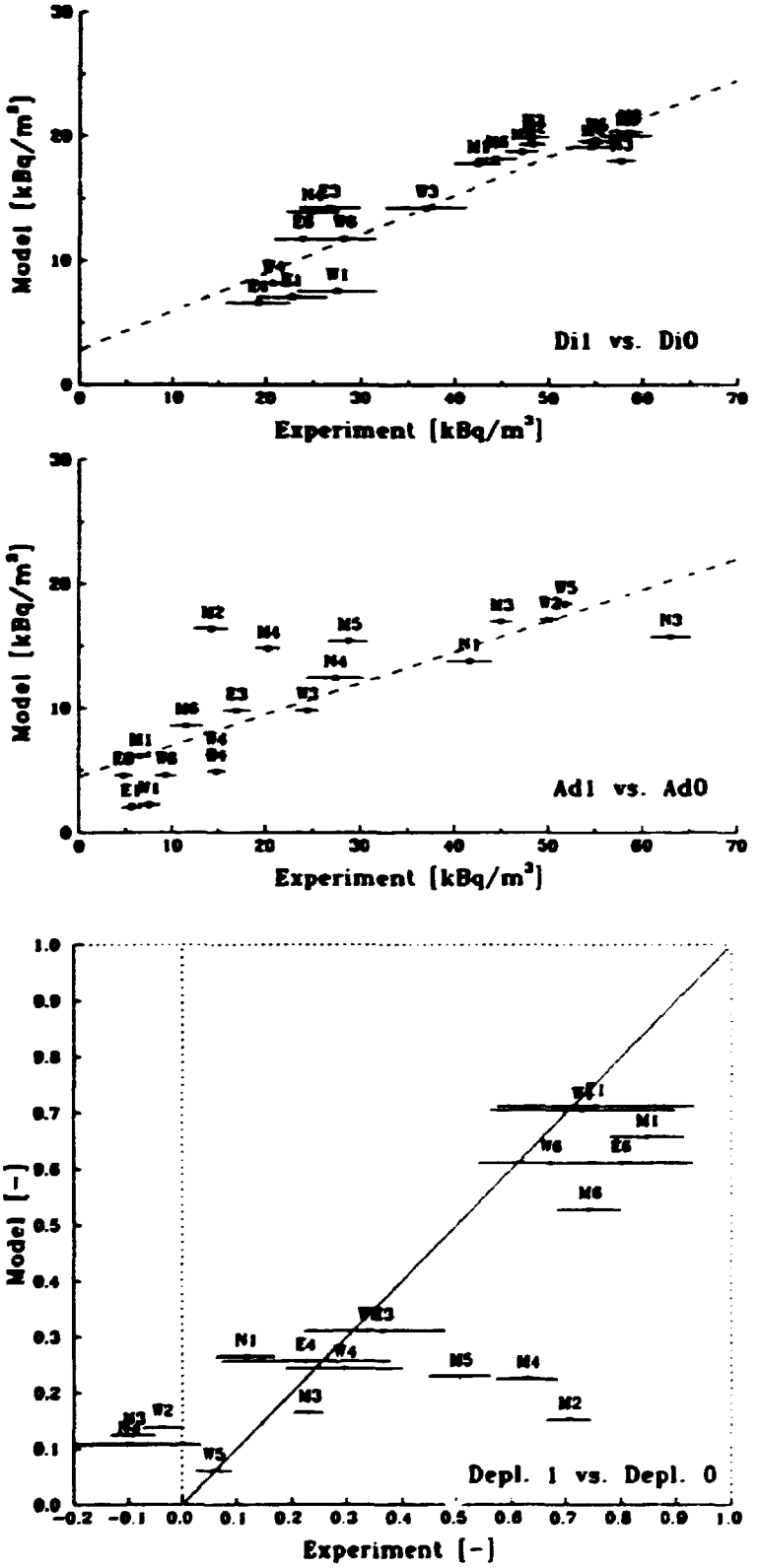

Figure 15. Model calculations: Di1, Ad1, and Depl. 1 versus measurements.

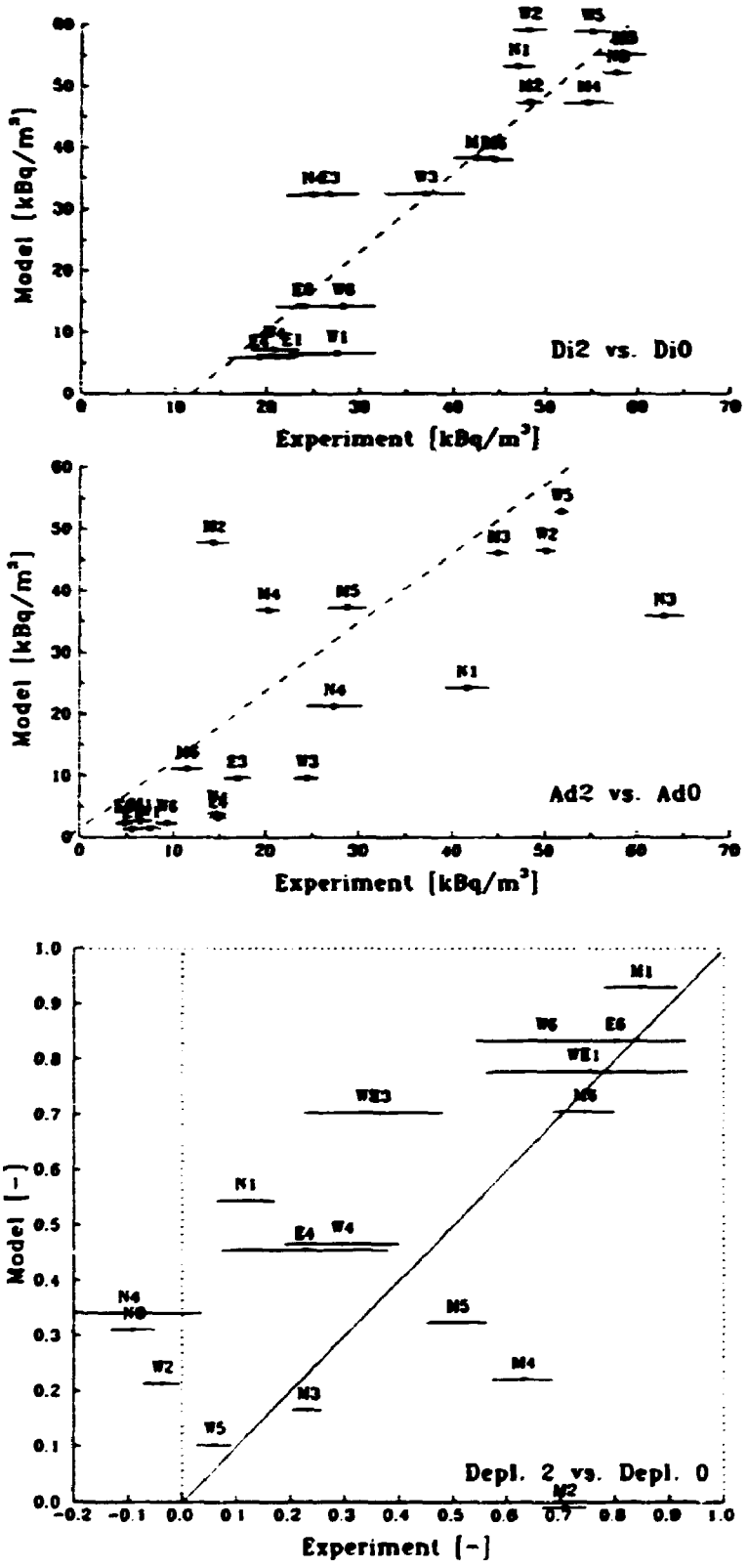

Figure 16. Model calculations: Di2, Ad2, and Depl. 2 versus measurements.

Table 8. Main results of model-experiment comparisons based on field values for 19 probe locations. APMR is the average prediction-to-measurement ratio defined in equation 87. r is the correlation coefficient, and a and b are regression coefficients. Depl. 1 is the calculated degrees of depletion from Di1 and Ad1, etc..

ID	r	a	b	APMR	Parameters
Pr1	0.95	0.94±0.07	0.00±0.1	1.0±0.2	K1
Pr2	0.95	0.98±0.08	-0.1±0.1	0.9±0.2	K2
Pr3	0.96	0.74±0.06	0.36±0.1	1.5±0.3	K3
Di1	0.91	0.31±0.03	2.8±1	0.39±0.02	S1, S1, E1
Di2	0.92	1.27±0.1	-15±6	0.82±0.08	S1, S2, E1
Di3	0.91	0.97±0.1	-7.9±5	0.74±0.06	S1, S2, E2
Di4	0.50	2.5±1	9±43	2.7±0.5	S1, S3, E2
Di5	0.80	0.67±0.1	22±5	1.3±0.08	S2, S2, E1
Ad1	0.81	0.25±0.04	4.5±1	0.53±0.06	S1, S1, E1, (K2)
Ad2	0.76	0.81±0.2	1.4±5	0.81±0.2	S1, S2, E1, (K2)
Ad3	0.79	0.63±0.1	2.5±4	0.73±0.1	S1, S2, E2, (K2)
Ad4	0.74	1.8±0.4	-1.2±12	1.6±0.4	S1, S3, E2, (K2)
Ad5	0.79	0.90±0.2	4.1±5	1.0±0.2	S2, S2, E1, (K2)
Depl. 1	0.79	0.54±0.1	0.11±0.05	0.91±0.09	see Di1 and Ad1
Depl. 2	0.54	0.48±2	0.29±0.1	1.45±0.2	see Di2 and Ad2
Depl. 3	0.69	0.54±0.1	0.25±0.07	1.4±0.2	see Di3 and Ad3
Depl. 4	0.40	0.38±0.2	0.42±0.1	1.6±0.3	see Di4 and Ad4
Depl. 5	0.57	0.57±0.2	0.29±0.1	1.6±0.2	see Di5 and Ad5

Table 9. Radon concentrations and degree of depletion for probes located pairwise symmetrically around the test structure. Depl. 0 is based on measured radon concentrations of Di0 and Ad0. Depl. 1 is based on model calculations Di1 and Ad1.

ID	Di0 $kBq\,m^{-3}$	Ad0 $kBq\,m^{-3}$	Depl. 0 %	Depl. 1 %
W1	27.6±4	7.4±1	73±16	70
E1	22.8±3	5.6±1	75±17	71
W3	37.0±4	24.4±1	34±10	31
E3	26.7±3	16.9±1	37±10	31
W4	20.8±2	14.7±1	30±9	24
E4	19.2±3	14.8±1	23±14	26
W6	28.2±3	9.3±1	67±12	61
E6	23.9±2	4.8±1	80±12	61

Compared with the situation for the diffusion dominated field, it is seen that most points are moved downwards along the regression line. It can be seen from table 8 that there are only slight differences between the Ad1/Ad0 and Di1/Di0 regression lines.

As for the Di1-Di0 comparison, a large discrepancy exists between the *absolute* radon concentrations of Ad1 relative to those of Ad0, which again can be explained by an incorrect value for the radon generation rate. Generally, the comments of the

previous subsection concerning the influence of the various sets of parameters on the model calculations also apply to Ad1-Ad5. The main results of the comparisons are found in table 8.

Depl.1 to Depl.5 versus Depl.0

The comparison between calculated and measured degrees of radon depletion is important for two reasons. Firstly, the degree of radon depletion (defined in equation 81) provides a 'normalized' measure that is relatively insensitive to the radon generation rates (absolute magnitude and inhomogeneities). Secondly, the comparison emphasizes the ability of the model to describe the combined diffusive and advective transport of radon, which is a key element in the model.

Table 8 shows, that the best correlation between calculated and measured degrees of depletions is obtained for Di1/Ad1 (Depl. 1) with a linear correlation coefficient of 0.79 and an average prediction-to-measurement ratio of 0.91±0.09. The other calculations have correlation coefficients below 0.69, and APMR's above 1.45±0.2.

The bottom part of figure 15 shows that the model calculations Di1/Ad1 predict the depletion of most probes fairly well. However, some outliers exist. For example, it is seen that the model underestimates the depletion of the probes located below the membrane (especially: M2, M4, and M5). This indicates that more soil gas pass through this region than calculated from the soil-gas model. It is likely, that this discrepancy might be explained by inhomogeneities in the permeabilities not captured in the simple two-layer model. Notice, that it was found previously, that the model underestimated the pressure couplings to these probes.

As mentioned in section 4.1, some probes are located pairwise symmetrically on the sides of the test structure. The results obtained for these probes deserve special attention since they provide the highest quality of data and might indicate possible soil inhomogeneities. Table 9 lists the results of the four pairs where radon measurements have been made: W1/E1, W3/E3, W4/E4, and W6/E6. The table shows, that there is good agreement within each pair, however in all but one case, the radon concentrations are higher for the west probes compared with those probes located on the east side; the exception is for W4/E4 under advective conditions where the measured radon concentrations are virtually equal. For the four sets of probes (under diffusive or advective conditions) we find that the east probes have radon concentrations that are 21±5 % lower than those of the corresponding west probes. This indicates the degree of inhomogeneity: for example the radon generation rate of the west side might be higher than that of the east side. Table 9 shows that the observed and calculated degrees of depletion are in very good agreement. For example, the model predicts the probe location at W3/E3 to be 31 % depleted, which is in excellent agreement with the measured values of 34±10 % and 37±10 %, respectively. The results presented in table 9 provide a strong indication that the model in fact describes the combined diffusive and advective transport quite well.

4.6 Discussion

The purpose of the following is to bring attention to some of the limitations of this verification exercise and to sum up conclusions.

Limitations

The amount of soil parameters available for the exercise present one limitation. For example, porosity and density have only been measured for the top 85 cm of the

soil. These values are not necessarily representative for the bottom part of the soil since the geological characterization showed a pronounced difference between soil types for the top and bottom regions. With better estimates for these parameters, the discrepancy between calculated and measured radon concentrations might not have existed.

The experimental work is limited in size with only three steady-state experiments. For example, it would have been of interest to repeat the reported experiments under winter time conditions or to conduct experiments with the cylinder being pressurized (i.e. reversed flow). Such experiments might have been conducted if the membrane of the excavation had not been partly removed for visual inspection after completion of the final experiment (30 August 91). On that occasion it was discovered that the layer of bentonite located between the membrane and the soil was partly cracked. The bentonite was simply dried out during the summer, and roots from the top vegetation had found their ways along the membrane. Since cracking of the bentonite represents potential danger of air leakage from the atmosphere along the membrane to the gravel layer this situation would seriously conflict the basic design goal of the test structure as 'simple and well-defined'. There are good reasons to belive that the data presented in this report have not been influenced by the cracking of the bentonite layer. Firstly, the flow resistance was virtually unchanged from the April 9 to July 25; the day after the final experiment with imposed flow (Ad3) was stopped. Thus, from July 26 to August 30, the test structure was operated only in 'diffusive mode' (Di0). An attempt was made to reestablish the bentonite layer, but a new measurement of the flow resistance showed that the visual inspection of the recovered membrane etc. had lowered the flow resistance by a factor of 2.6: the structure now had a leak along the soil-membrane interface. Finally, it is of interest to notice that the physical flow of soil gas from the 'deep' soil to the gravel apparently is larger for the physical structure than predicted in the model calculations[18]. For example, the pressure coupling to the probes located below the membrane are larger than those of the model calculations These probes are also more depleted for radon than predicted from the model calculations.

The model calculations are limited in the sense that the model is two-dimensional and that it is therefore necessary to treat the square-formed test structure as being circular. Furthermore, the model is not capable of simulating the inclined wall of the test structure excavation. These limitations might have changed the calculated field values at physical probe locations. However, only those of the probes located close to the excavation wall are likely to have been affected.

Conclusion

The main question of this verification exercise is if the model calculations based on the measured set of parameters match (or mismatch) the experimental results such that we may conclude the model to be right (or wrong). Because of the limitations related to the soil characterization (described above) it is not possible to answer this question firmly. However, there *are* elements of the model-experiment comparison that strongly suggest the model to be right. First of all, the model predicted the pressure couplings of most soil probes fairly well; Pr1, Pr2, and Pr3. Secondly, the radon concentration *profiles* under diffusive and advective conditions were also correctly described by the model; Di1 and Ad1. The best support, however, is found in the comparison of measured and calculated degrees of radon depletion. This test suppresses inhomogeneities related to the radon generation rate (and its absolute value) and emphasizes the ability of the model to describe

[18] Leakage along the membrane would cause an opposite effect.

the combined diffusive and advective transport of radon in the soil. Again, there is good agreement for most probe locations; Dil and Adl (i.e. Depl. 1).

In contrast to the abovementioned, there is also evidence of discrepancies between experimental results and model calculations. However, we claim that these mainly can be explained in terms of soil inhomogeneities or incomplete mapping of some of the soil parameters. For example, the overall discrepancy between measured and calculated radon concentrations (Dil and Adl) are clearly due to an incorrect value for the radon generation rate that rely on the four measured parameters: radon emanation rate, soil porosity, density and moisture content. A discrepancy of more concern, is the underestimation of the soil-gas entry rate into the cylinder for a given depressurization. Even if the soil is assumed to be homogeneous and to have a permeability equal to the highest of the measured values ($1.4 \cdot 10^{-11}$ m^2) the calculated flow resistance is still off by a factor of two. To this end, we add the observations that the pressure couplings and the degree of radon depletion of the probes located below the membrane were found to be higher in the experimental situation than in the model calculation. All of this indicate that more soil gas passes through the center part of the soil (below the gravel) than calculated from the measured permeabilities. It is likely that part of the discrepancy is to due to inhomogeneities of the soil not captured in the permeability measurements and the two-layer model calculations. For example, visual inspection of the subsoil made during the construction phase of the structure showed 'pockets' of highly permeable sand or gravel at various locations in the soil. However, whether such deposits could dominate the soil-gas flow remains unsolved in this investigation.

It is important to bring in mind, that this verification exercise was conducted under field conditions typical for Danish surface geology. The type of soils found here are normally far from homogeneous and verification under such circumstances appears to be important given that the framework of mathematical models and site characterization techniques of the type presented herein are to be applied for any predictive, diagnostic or mitigative purposes related to the entry of soil-gas pollutants into houses.

5 Modelling entry into houses

The purpose of this chapter is to use the numerical model of chapter 3 to quantify the influence of building and soil related factors on the radon entry rates into real houses. The emphasis of the investigation is on slab-on-grade houses since this house type is common in Denmark and tends to have higher indoor radon levels compared with basement and crawl-space houses.

The chapter is divided into four sections. Firstly, we outline the background and objective of the investigation. Thereafter, we present details regarding the application of the numerical model. Finally, in the last two sections we report and discuss the findings of the sensitivity analysis.

5.1 Background

Various aspects of the entry of radon into houses have previously been studied using analytical and numerical methods. Reviews are given in [Lou87], [Naz88B], [Nero90], and [Gad91]. In the following, we briefly review that part of the literature on which this study has been based and outline the objective of this investigation.

Previous studies

Dimbylow et al. investigated the steady-state entry of radon through cracks in a concrete slab using 2-dimensional finite-difference and finite-element models: [Wil85], [Dim85], [Dim87], [Wri88]. Three cases were considered: a slab with a single crack in the center, a slab with a periodic array of cracks, and a bare-soil floor. In [Dim85] it was found that for concrete cracked periodically with 1 cm in crack width and 50 cm in distance between cracks, the diffusive entry of radon (for Δp=0) can be as high as 50 % compared with the entry through a bare-soil floor. In [Dim87] and [Wri88] pressure-driven entry was modelled. Values were given for the radon concentration gradient at the crack-house interface as a function of house depressurization and soil permeability among other parameters. It was found, that depressurization of a house can lead to a 15 fold increase in radon entry compared with the case where diffusion is the only transport mechanism. However, for most combinations of the investigated parameters the effect was much smaller. Moreover, it was concluded that because of the low permeability of concrete, the sealing of cracks should be an effective remedial measure to reduce indoor radon concentrations. However, since the crack width and periodicity were found to have a relative little influence on the radon entry rates, sealing a concrete floor would only be effective if all cracks are sealed.

Mowris modelled the steady-state entry of soil-gas into basement houses using a buried drain analogy and a finite-difference model coupled with empirical expressions for the flow resistance across cracks in the slab: [Mow86]. It was demonstrated, that the soil resistance dominates over that of the crack for crack widths larger than 0.5 mm.

Loureiro developed a 3-dimensional steady-state finite-difference model, and investigated the entry of radon into a depressurized basement house located on homogeneous soil: [Lou87], [Lou90]. The main factors of the sensitivity analysis were radon source variables, applied house depressurization, soil permeability, width of the perimeter crack, bulk diffusion constant, soil porosity, and depth of the water table. Loureiro demonstrated that those of the investigated variables that had the most dramatic effect on the radon entry rate were the radium concentration of the soil, the soil permeability, and the applied house depressurization. It was shown, that the entry can be divided into a diffusive and advective component, and that

the radon entry rate for sufficiently low permeabilities will be mainly affected by source related variables.

Rogers and Nielson developed and benchmarked a numerical model that incorporates steady-state soil-gas and radon transport, and correlation between soil parameters; [Rog90]. An output variable called the radon entry efficiency was defined as the indoor radon concentration divided by the area-averaged sub-slab radon concentration in the soil pores. The radon entry efficiency was calculated for a slab-on-grade house for different soil types and perimeter crack areas. The analysis suggested 0.03 % radon entry efficiency for slab-on-grade houses on low permeable soils, increasing to 0.1 % for sandy soils. A benchmark test was conducted for one Florida house, and it was found that for a house depressurization of 1 Pa, the calculated indoor radon concentration was within 30 % of the measured value.

Revzan et al. made a steady-state finite difference model of radon entry into basement houses using the same framework as that presented by Loureiro; [Rev90], [Rev91]. A basement house with footer, L-shaped crack, subfloor gravel layer, backfill, and alternative entry routes was modelled. The most important of the structural factors was found to be the presence or absence of a gravel layer of relatively high permeability gravel under the basement slab. For low permeability soils, the radon entry rate through the slab-footer crack increased by a factor of 5 when the gravel was added. The sizes and number of cracks or openings in the slab were found to be relatively unimportant for the radon entry rates as long as the overall area of the penetration was small compared with the area of the slab and as long as the flow resistance of the openings remained small compared with that of the soil. Soil gas transport due to natural convection (buoyancy) in response to the heat loss from the basement was also studied, and it was shown to increase the radon entry rate by approximately 40 %. Finally, the modelling results were compared with available data from a number of houses in the Spokane River Valley. Assuming the soil to be homogeneous and isotropic with permeability equal to the mean of the measured values, the predicted radon entry rates were 22 % of the mean of the observations.

Objectives

Most of the above mentioned studies concern basement houses. Since slab-on-grade houses are common in Denmark and tend to have higher radon levels compared with crawl-space and basement houses. [Sund87], the main objective of this study is:

- to investigate the influence of building and soil related factors on the entry rates into slab-on-grade houses
- to intercompare entry rates for slab-on-grade and basement houses

Table 10 outlines the investigated factors. Given the reference configuration stated in column three, we change each of the parameters in turn, and observe the impact on entry rates of soil gas and radon into the house.

5.2 Modelling details

We use the model described in chapter 3, and all assumptions stated there apply to the present situation.

Table 10. Outline of factors investigated in the sensitivity analysis

Factors	Parameter range	Reference configuration
Geological factors		
k, m^2	10^{-13}, 10^{-12}, 10^{-11}, 10^{-10}, 10^{-9}	(a)
D, $m^2 s^{-1}$	$5 \cdot 10^{-9}$, 10^{-6}, $4 \cdot 10^{-6}$	10^{-6}
Structural factors		
Slab leakage	3 mm crack or bare soil floor	Crack
House type	Basement or slab-on-grade	Slab-on-grade
Gravel layer	Present or not present	Present
Backfill	Present or not present	Not present
Footer	30, 60, 90 cm	90 cm
House depressurization		
Δp, Pa	-0.1, -5, -10, -20	-5

(a) No preference permeability is defined.

Computational plane

The model is used in circular cylindrical coordinates as in the previous chapter, which implies that all house features and soil inhomogeneities must be axial-symmetric. The computational plane extends 10 m in the vertical direction and 20 m in the horizontal.

The idealized slab-on-grade and basement houses are shown in figure 17 and figure 18, respectively. The dimensions reflect the general recommendations of the Danish building authorities; [Chr69], [Byg82], [Bal85]. The building shell is divided into three regions: slab, wall, and footer. These regions can be assigned individual properties for permeability and diffusivity. In this investigation the building materials are assumed to be virtually soil-gas and radon tight with permeability and diffusivity equal to 10^{-18} m^2 and 10^{-10} $m^2 s^{-1}$, respectively. The internal generation of radon within the building materials is set to zero for all calculations. The vicinity of the house is divided into three regions: undisturbed soil, subfloor gravel layer, and backfill region. Again, each region can be assigned individual properties.

Boundary conditions

For the soil-gas transport, the disturbance pressure is assumed to equal zero at the atmospheric surface and -5 Pa at the indoor side of the crack[19] unless otherwise specified. The remaining part of the boundary, including the indoor side of the building shell, fulfills no-flow conditions. In the calculation of entry rates into houses with bare-soil floor, the inside part of the 'slab' is assigned a constant pressure of -5 Pa[20]. Similar conditions apply to the radon field. The outdoor and indoor radon concentrations are set to zero and the remaining part of the boundary fulfills no-flow conditions. In the calculation of entry rates into houses with bare-soil floor, the inside part of the 'slab' is assigned a radon concentration of zero at the indoor side. Setting the indoor radon concentration to zero is conceptually incorrect, but causes no significant errors in the calculations of the

[19]The boundary section named: BC_per in figure 3 on page 18.
[20]The boundary section named: BC_cen in figure 3 on page 18.

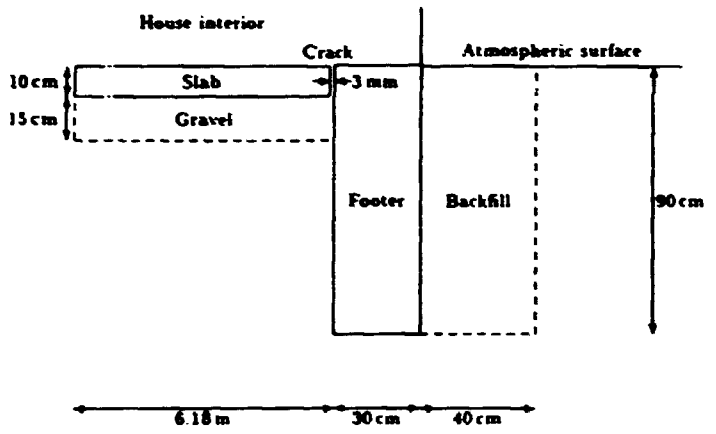

Figure 17. Outline of slab-on-grade house.

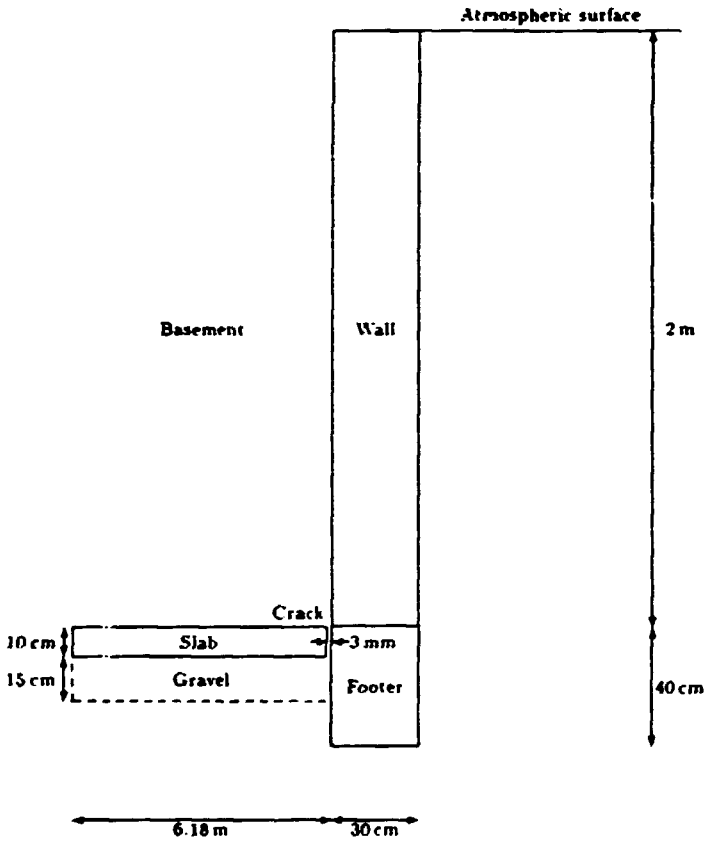

Figure 18. Outline of basement house.

radon entry rates. The approximation is only violated when the entry is mainly advective. However, under such circumstances, the indoor compartment is located on the down-stream side of the flow causing only minor effects on radon entry rates or radon concentrations of the up-stream side. For the cases where diffusion dominates, the indoor radon concentrations are in fact low and the approximation holds.

Modelling transport through the crack

Modelling of the transport through the crack is an implicit part of this model since the computational grid covers the building shell and the crack region. In the model of Loureiro, the transport within the crack was treated separately using exact (analytical) solutions of the transport problems.

The flow resistance of a straight-through crack is described empirically and theoretically in [Bak87] by the following expression:

$$\Delta p_c = AQ + BQ^2 \tag{88}$$

where Q is the soil-gas flow rate through the crack and Δp_c is the pressure drop across the crack. The A and B coefficients for an infinitely long and straight-through crack are given as:

$$A = \frac{12\mu h}{Td^3} \tag{89}$$

$$B = \frac{\rho_a C}{2d^2T^2} \tag{90}$$

where C is a geometric factor here equal to 1.4. μ is the dynamic viscosity, and ρ_a is the density of air. T, d, and h are length, width, and height of the crack, respectively. In this chapter, the highest flow rate for an indoor-outdoor pressure difference of 5 Pa is of the order of $6 \cdot 10^{-3}$ $m^3 s^{-1}$ distributed over a length of 38.8 m ($\simeq 2\pi \cdot 6.18$ m). Thus, the maximum pressure drop across the crack is 0.13 Pa or less than 0.3 % of the total indoor-outdoor pressure difference. Neglecting the non-linear part of the crack resistance introduces an error of less than $2 \cdot 10^{-3}$ Pa. In this model, we adopt only the linear part of the crack flow resistance (B=0) because it eases the modelling efforts considerably. The calculated soil-gas and radon entry rates are insensitive to the errors introduced because of this, and the choice of a crack thickness of exactly 3 mm is anyway rather arbitrary. Hence, we simulate the crack resistance by assigning the computational crack region a permeability, k_c, such that for a given entry rate of soil gas we obtain the same pressure drop across the crack as given in equation 88. Combining Darcy's law and equation 88 with $B = 0$ gives:

$$\begin{aligned} Q_{crack} &= Q_{Darcy} \Rightarrow \\ \frac{\Delta p_c}{A} &= dT\frac{k_c}{\mu}\frac{\Delta p_c}{h} \Rightarrow \\ k_c &= \frac{d^2}{12} \Rightarrow \\ k_c &= 7.5 \cdot 10^{-7} m^2 \end{aligned}$$

where T=38.8 m, d=3 mm, and h=0.1 m. A series of model calculations have been investigated in detail to verify the presented method. It was found that the pressure drop across the crack agreed within 0.1 % compared with that of equation 88.

The radon transport through the crack is treated in a similar fashion by assigning the crack region appropriate transport parameters and verify that the calculated fields agree with the analytical solution presented in [Col81]. For the radon transport the region is assigned a diffusion constant equal to that of radon in free air: $D_{crack} = 1.2 \cdot 10^{-5}$ $m^2 s^{-1}$. The porosity is set to unity.

Reference configuration

The reference configuration is defined as a 120 m^2 (radius=6.18 m) slab-on-grade house with building materials that are soil-gas and radon tight except for a 3 mm

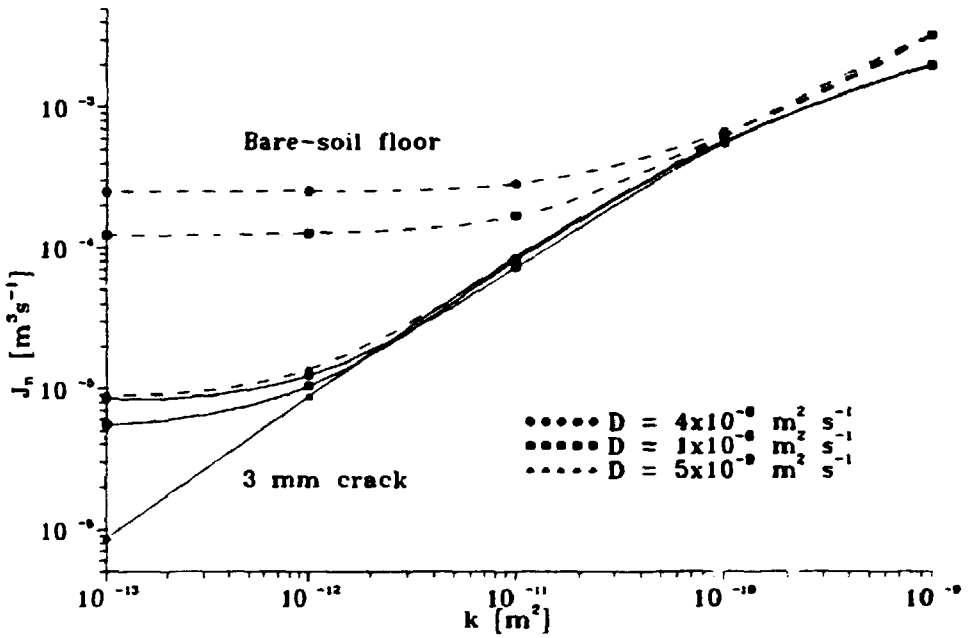

Figure 19. Geological factors and slab type: Normalized radon entry rate vs. permeability and diffusivity for a 'slab-on-grade' house with a perimeter crack (solid lines) or bare-soil floor (dashed lines).

perimeter crack at the slab-wall joint: see figure 17. Such a perimeter crack is likely to exist in a real house because the foundation and the slab are poured separately. The building materials are without internal radon sources. The house is depressurized 5 Pa relative to the atmosphere and the soil is assumed to be homogeneous and dry (m=0) with porosity (ϵ) and bulk diffusivity (D) equal to 0.5 and 10^{-6} $m^2 s^{-1}$, respectively. The radon generation rate (G) is arbitrarily set to λc_∞, where c_∞=1 Bq m^{-3}. We have not included any reference value for the permeability of the soil. The house footer extends 90 cm below the atmospheric surface, and the 'backfill region' is filled with ordinary soil. A 15 cm capillary breaking layer of gravel of permeability equal to $5 \cdot 10^{-9}$ m^2 is located below the slab. Other parameters of the gravel layer are equal to those of the undisturbed soil. The calculations are based on a dynamic viscosity (μ) of $18.3 \cdot 10^{-6}$ Pa s.

5.3 Sensitivity analysis

The sensitivity analysis is simply based on calculations of soil-gas and radon entry rates for a number of selected configurations as outlined in table 10. Because of the importance of the soil permeability, k, we have organized the analysis such, that all other factors are investigated in combination with changes in the permeability. For each configuration, we report the soil-gas and normalized radon entry rates, Q ($m^3 s^{-1}$) and J_n ($m^3 s^{-1}$), and where meaningful, the normalized radon concentration at the soil-crack interface, c_n (-). J_n and c_n are normalized with respect to c_∞, the radon concentration at infinite depth: see page 11:

$$J = c_\infty J_n \tag{91}$$

$$c_{crack} = c_\infty c_n \tag{92}$$

Table 11. Geological factors: perimeter crack. Variation of soil diffusivity and permeability.

k	Q	$D=4\cdot10^{-6}$ m^{2}s^{-1}		$D=1\cdot10^{-6}$ m^{2}s^{-1}		$D=5\cdot10^{-9}$ m^{2}s^{-1}	
		c_n	J_n	c_n	J_n	c_n	J_n
m^2	m^{3}s^{-1}	-	m^{3}s^{-1}	-	m^{3}s^{-1}	-	m^{3}s^{-1}
10^{-9}	$4.4\cdot10^{-3}$	0.45	$2.0\cdot10^{-3}$	0.45	$2.0\cdot10^{-3}$	0.45	$2.0\cdot10^{-3}$
10^{-10}	$7.7\cdot10^{-4}$	0.71	$5.5\cdot10^{-4}$	0.73	$5.6\cdot10^{-4}$	0.73	$5.7\cdot10^{-4}$
10^{-11}	$8.7\cdot10^{-5}$	0.82	$7.2\cdot10^{-5}$	0.93	$8.1\cdot10^{-5}$	0.98	$8.5\cdot10^{-5}$
10^{-12}	$8.8\cdot10^{-6}$	0.66	$1.2\cdot10^{-5}$	0.55	$1.0\cdot10^{-5}$	0.46	$8.7\cdot10^{-6}$
10^{-13}	$8.8\cdot10^{-7}$	0.59	$8.5\cdot10^{-6}$	0.38	$5.5\cdot10^{-6}$	0.06	$8.7\cdot10^{-7}$

Table 12. Geological factors: bare-soil floor. Variation of soil diffusivity and permeability.

k	Q	$D=4\cdot10^{-6}$ m^{2}s^{-1}	$D=1\cdot10^{-6}$ m^{2}s^{-1}	$D=5\cdot10^{-9}$ m^{2}s^{-1}
		J_n	J_n	J_n
m^2	m^{3}s^{-1}	m^{3}s^{-1}	m^{3}s^{-1}	m^{3}s^{-1}
10^{-9}	$8.2\cdot10^{-3}$	$3.2\cdot10^{-3}$	$3.3\cdot10^{-3}$	$3.3\cdot10^{-3}$
10^{-10}	$8.2\cdot10^{-4}$	$6.6\cdot10^{-4}$	$6.2\cdot10^{-4}$	$6.1\cdot10^{-4}$
10^{-11}	$8.2\cdot10^{-5}$	$2.8\cdot10^{-4}$	$1.7\cdot10^{-4}$	$8.2\cdot10^{-5}$
10^{-12}	$8.2\cdot10^{-6}$	$2.5\cdot10^{-4}$	$1.3\cdot10^{-4}$	$1.4\cdot10^{-5}$
10^{-13}	$8.2\cdot10^{-7}$	$2.5\cdot10^{-4}$	$1.2\cdot10^{-4}$	$9.0\cdot10^{-6}$

where J is the radon entry rate (Bq s^{-1}), and c_{crack} is the radon concentration at the soil-crack interface (Bq m^{-3}). Before any other factors are analyzed, it is therefore important to observe, that for homogeneous soil the radon entry rate is proportional to the radon generation rate of the soil (i.e. c_∞).

Geological factors and slab type

Firstly, we investigate the influence of diffusivity and permeability on the radon entry rate into a house with a perimeter crack (reference configuration) or a bare-soil floor.

Table 11 shows the results for the house with a perimeter crack. For example, if $D=10^{-6}$ m^2 s^{-1}and $k=10^{-11}$ m^2, soil-gas enters the house through the crack with a rate of $8.7\cdot10^{-5}$ m^{3}s^{-1}. The normalized radon concentration at the soil-crack interface is 0.93 (i.e. 93 % of c_∞), and the normalized radon entry rate is $8.1\cdot10^{-5}$ m^{3}s^{-1}. Hence, if c_∞ equals 20 kBq m^{-3}, then the entry rate of radon would be 1.62 Bq s^{-1}.

Column two of the table shows, that the soil-gas entry rate increases with the permeability. For permeabilities that are low compared with that of the gravel layer, the increase is virtually linear. The radon concentration at the crack takes the highest values for $k=10^{-11}$ m^2. For higher permeabilities, the soil is partly depleted for radon. For example, c_n decreases by app. a factor of 2, if k is enhanced from 10^{-11} m^2 to 10^{-9} m^2. For permeabilities lower than 10^{-11} m^2, c_n also decreases, which is due to the influence of the indoor radon concentration imposed at the bottom of the crack. The radon entry rate increases with the permeability. For $k\geq10^{-11}$ m^2, the entry is mainly advective, and J_n equals the product of c_n and Q. The table shows that the diffusion constant is of marginal importance for the radon entry rate unless $k=10^{-13}$ m^2, where J_n is anyway small. Notice, that D is the diffusion constant for the undisturbed soil *and* the gravel layer[21].

[21] If the gravel layer is assigned an individual diffusion constant of 10^{-6} m^{2}s^{-1}, we obtain radon entry rates that are somewhat different from those given in column 4 and 8 of table 11. For a soil diffusivity of $4\cdot10^{-6}$ m^{2}s^{-1}, $J_n=9.5\cdot10^{-6}$ m^{3}s^{-1} for $k=10^{-12}$ m^2 and $J_n=$

Table 13. House type: Slab-on-grade or basement.

	Slab-on-grade			Basement		
k	Q	c_n	J_n	Q	c_n	J_n
m^2	$m^3 s^{-1}$	-	$m^3 s^{-1}$	$m^3 s^{-1}$	-	$m^3 s^{-1}$
10^{-9}	$4.4 \cdot 10^{-3}$	0.45	$2.0 \cdot 10^{-3}$	$4.7 \cdot 10^{-3}$	0.55	$2.6 \cdot 10^{-3}$
10^{-10}	$7.7 \cdot 10^{-4}$	0.73	$5.6 \cdot 10^{-4}$	$8.3 \cdot 10^{-4}$	0.85	$7.1 \cdot 10^{-4}$
10^{-11}	$8.7 \cdot 10^{-5}$	0.93	$8.1 \cdot 10^{-5}$	$9.3 \cdot 10^{-5}$	0.97	$9.0 \cdot 10^{-5}$
10^{-12}	$8.8 \cdot 10^{-6}$	0.55	$1.0 \cdot 10^{-5}$	$9.4 \cdot 10^{-6}$	0.58	$1.1 \cdot 10^{-5}$
10^{-13}	$8.8 \cdot 10^{-7}$	0.38	$5.5 \cdot 10^{-6}$	$9.4 \cdot 10^{-7}$	0.39	$5.6 \cdot 10^{-6}$

Table 14. Structual factors: Subfloor gravel layer.

	Gravel			No gravel		
k	Q	c_n	J_n	Q	c_n	J_n
m^2	$m^3 s^{-1}$	-	$m^3 s^{-1}$	$m^3 s^{-1}$	-	$m^3 s^{-1}$
10^{-9}	$4.4 \cdot 10^{-3}$	0.45	$2.0 \cdot 10^{-3}$	$1.9 \cdot 10^{-3}$	0.55	$1.1 \cdot 10^{-3}$
10^{-10}	$7.7 \cdot 10^{-4}$	0.73	$5.6 \cdot 10^{-4}$	$1.9 \cdot 10^{-4}$	0.85	$1.7 \cdot 10^{-4}$
10^{-11}	$8.7 \cdot 10^{-5}$	0.93	$8.1 \cdot 10^{-5}$	$1.9 \cdot 10^{-5}$	0.73	$1.9 \cdot 10^{-5}$
10^{-12}	$8.8 \cdot 10^{-6}$	0.55	$1.0 \cdot 10^{-5}$	$1.9 \cdot 10^{-6}$	0.41	$6.1 \cdot 10^{-6}$
10^{-13}	$8.8 \cdot 10^{-7}$	0.38	$5.5 \cdot 10^{-6}$	$1.9 \cdot 10^{-7}$	0.37	$5.2 \cdot 10^{-6}$

Table 12 shows the results for a house with a bare-soil floor and no gravel layer. The house is otherwise as in the reference configuration. Such houses exist in Denmark, however the reason why they are included in this investigation is mainly because they provide a means of reference regarding a slab that is very leaky, and because entry into crawl spaces might be similar in magnitude. The table shows that Q is proportional to k as expected since the entire soil volume now has the same permeability. For $k \geq 10^{-10}$ m^2, J_n is virtually independent of D, but for all other permeabilities D is an important factor. As expected from equation 44 on page 11. J_n decreases with the square of the diffusion constant: for example, if D is changed from $4 \cdot 10^{-6}$ to 10^{-6} m^2 s^{-1}, then J_n decreases by a factor of 2.

Figure 19 shows the radon entry rates for both slab types versus permeability. A number of observations can be made: (1) The diffusive entry into the bare-soil house dominates over the advective entry for permeabilities up to app. 10^{-11} m^2. (2) The entry into the house with the perimeter crack is insensitive to the magnitude of diffusion constant for most permeabilities. (3) If the diffusion constant is set to $5 \cdot 10^{-9}$ m^2 s^{-1}, then the entry rate of radon into the bare-soil house app. equals that of the perimeter-crack house.

House type

Table 13 shows the entry rates for a slab-on-grade house and a basement house of a similar configuration: see figure 17 and 18. For all of the stated permeabilities, the soil-gas entry rate is app. 10 % higher for the basement house compared with that of the slab-on-grade house. Also the radon entry rate is calculated to be higher for the basement house, which is partly due to the increased Q and partly because the soil is less depleted of radon. For $k = 10^{-9}$ m^2 or 10^{-10} m^2, J_n is app. 30 % higher

$5.3 \cdot 10^{-6}$ m^2 s^{-1} for $k = 10^{-11}$ m^2. For a soil diffusivity of $5 \cdot 10^{-9}$ m^2 s^{-1}, $J_n = 9.5 \cdot 10^{-6}$ m^3 s^{-1} for $k = 10^{-12}$ m^2 and $J_n = 3.9 \cdot 10^{-6}$ m^2 s^{-1} for $k = 10^{-13}$ m^2. The radon entry rates differ by less than 0.5 % from those of table 11, if $k \geq 10^{-11}$ m^2. This note was added during the revision of the report April 1992

Table 15. Structual factors: Backfill.

	No backfill		Backfill. $G_b/G = 1$		Backfill. $G_b/G = 0.1$	
k	Q	J_n	Q	J_n	Q	J_n
m^2	$m^3 s^{-1}$	$m^3 s^{-1}$	$m^3 s^{-1}$	$m^3 s^{-1}$	$m^3 s^{-1}$	$m^3 s^{-1}$
10^{-9}	$4.4 \cdot 10^{-3}$	$2.0 \cdot 10^{-3}$	$4.3 \cdot 10^{-3}$	$2.1 \cdot 10^{-3}$	$4.3 \cdot 10^{-3}$	$2.1 \cdot 10^{-3}$
10^{-10}	$7.7 \cdot 10^{-4}$	$5.6 \cdot 10^{-4}$	$7.7 \cdot 10^{-4}$	$5.6 \cdot 10^{-4}$	$7.7 \cdot 10^{-4}$	$5.5 \cdot 10^{-4}$
10^{-11}	$8.7 \cdot 10^{-5}$	$8.1 \cdot 10^{-5}$	$9.5 \cdot 10^{-5}$	$8.7 \cdot 10^{-5}$	$9.5 \cdot 10^{-5}$	$8.6 \cdot 10^{-5}$
10^{-12}	$8.8 \cdot 10^{-6}$	$1.0 \cdot 10^{-5}$	$1.0 \cdot 10^{-5}$	$1.1 \cdot 10^{-6}$	$1.0 \cdot 10^{-5}$	$1.1 \cdot 10^{-5}$
10^{-13}	$8.8 \cdot 10^{-7}$	$5.5 \cdot 10^{-6}$	$1.0 \cdot 10^{-6}$	$5.7 \cdot 10^{-6}$	$1.0 \cdot 10^{-6}$	$5.7 \cdot 10^{-6}$

Table 16. Structual factors: Footer.

	30 cm		60 cm		90 cm	
k	Q	J_n	Q	J_n	Q	J_n
m^2	$m^3 s^{-1}$	$m^3 s^{-1}$	$m^3 s^{-1}$	$m^3 s^{-1}$	$m^3 s^{-1}$	$m^3 s^{-1}$
10^{-9}	$5.8 \cdot 10^{-3}$	$1.8 \cdot 10^{-3}$	$4.9 \cdot 10^{-3}$	$1.9 \cdot 10^{-3}$	$4.4 \cdot 10^{-3}$	$2.0 \cdot 10^{-3}$
10^{-10}	$1.1 \cdot 10^{-3}$	$5.8 \cdot 10^{-4}$	$8.8 \cdot 10^{-4}$	$5.7 \cdot 10^{-4}$	$7.7 \cdot 10^{-4}$	$5.6 \cdot 10^{-4}$
10^{-11}	$1.2 \cdot 10^{-4}$	$9.6 \cdot 10^{-5}$	$1.0 \cdot 10^{-4}$	$8.8 \cdot 10^{-5}$	$8.7 \cdot 10^{-5}$	$8.1 \cdot 10^{-5}$
10^{-12}	$1.2 \cdot 10^{-5}$	$1.1 \cdot 10^{-5}$	$1.0 \cdot 10^{-5}$	$1.1 \cdot 10^{-5}$	$8.8 \cdot 10^{-6}$	$1.0 \cdot 10^{-5}$
10^{-13}	$1.2 \cdot 10^{-6}$	$5.1 \cdot 10^{-6}$	$1.0 \cdot 10^{-6}$	$5.4 \cdot 10^{-6}$	$8.8 \cdot 10^{-7}$	$5.5 \cdot 10^{-6}$

for the basement house. For lower permeabilities, the increase amounts to less than 11 %. It is important to stress, that we cannot in general expect basement houses to have higher indoor radon levels than slab-on-grade houses because of this. Firstly, the indoor volume is larger for the basement houses, and secondly the driving forces and the internal airflow might be different for the two house types.

Gravel layer

Table 14 shows that having a highly permeable gravel layer in the subfloor region increases the entry rate of soil gas by a factor of 2.3 to 4.6. The lowest factor is for $k=10^{-9}$ m^2 that is comparable with the permeability of the gravel layer ($5 \cdot 10^{-9}$ m^2). The entry rate of radon is less affected for two reasons: Firstly, for soils of low permeability, the entry is mainly diffusive and J_n is not sensitive to changes in Q. Secondly, for soils of high permeability, the increase in Q is partly compensated by a subsequent decrease in c_n. The largest change of J_n occurs for $k=10^{-11}$ m^2: relative to the situation for a house without a gravel layer, J_n is increased by a factor of 4.3.

Backfill

Table 15 illustrates the impact of having a highly permeable backfill region located on the outer side of the footer for example, for drainage purposes. Three cases are considered. The first is the reference configuration that is defined not to have any special backfill material. In the second case, backfill material of 10^{-10} m^2 in permeability is filled into the 'backfill region' indicated in figure 17. Except for the permeability, the material is assumed to have the same properties as the undisturbed soil. The final case is different from the second only with respect to the radon generation rate, that is assumed to take a value that is an order of

Table 17. House depressurization.

k	0.1 Pa		5 Pa		10 Pa		20 Pa	
	c_n	J_n	c_n	J_n	c_n	J_n	c_n	J_n
m^2	-	$m^3 s^{-1}$	-	$m^3 s^{-1}$	-	$m^3 s^{-1}$	-	$m^3 s^{-1}$
10^{-9}	0.92	$8.0 \cdot 10^{-5}$	0.45	$2.0 \cdot 10^{-3}$	0.36	$3.2 \cdot 10^{-3}$	0.27	$4.9 \cdot 10^{-3}$
10^{-10}	0.67	$1.6 \cdot 10^{-5}$	0.73	$5.6 \cdot 10^{-4}$	0.62	$9.6 \cdot 10^{-4}$	0.52	$1.6 \cdot 10^{-3}$
10^{-11}	0.40	$6.0 \cdot 10^{-6}$	0.93	$8.1 \cdot 10^{-5}$	0.91	$1.6 \cdot 10^{-4}$	0.84	$2.9 \cdot 10^{-4}$
10^{-12}	0.37	$5.2 \cdot 10^{-6}$	0.55	$1.0 \cdot 10^{-5}$	0.71	$1.7 \cdot 10^{-5}$	0.87	$3.3 \cdot 10^{-5}$
10^{-13}	0.37	$5.1 \cdot 10^{-6}$	0.38	$5.5 \cdot 10^{-6}$	0.40	$6.0 \cdot 10^{-6}$	0.44	$7.0 \cdot 10^{-6}$

magnitude lower than that of the undisturbed soil[22]: $G_b/G = 0.1$. Table 15 shows that for $k > 10^{-10}$ m^2, the entry rate of soil gas is increased by app. 10 % because of the backfill material. The radon entry rate is less affected. The largest change in J_n occurs for $k=10^{-11}$ m^2, where the change amounts to app. 7 %. The table also shows, that J_n is quite insensitive to the radon generation rate of the backfill material.

Footer

In the reference configuration, the footer extends 90 cm below the atmospheric surface. In comparison, table 16 shows the entry rates into houses with footers extending to depths of 30 and 60 cm, respectively. Since the footer partly blocks the direct flow path from the crack to the surface, the soil-gas entry rate increases with decreasing depth of the footer. Relative to the reference configuration, the increase amounts to app. 40 % for the 30 cm footer, and app. 10 % for the 60 cm footer. The entry rate of radon is affected differently, because of the influence of the radon-free air at the atmospheric surface. For example, for $k=10^{-9}$ m^2, J_n decreases 10 % if the footer is changed from 90 cm to 30 cm. Thus, the increase in Q is compensated by an increased degree of radon depletion. For permeabilities in the range from 10^{-10} m^2 to 10^{-12} m^2, J_n increases with decreasing depths of the footer. The maximum increase of J_n is 20 %, which occurs at $k=10^{-11}$ m^2, if the footer depth is changed from 90 to 30 cm.

House depressurization

Table 17 shows entry rate as function of house depressurization[23]. Four cases are considered: 0.1 Pa, 5 Pa (reference configuration), 10 Pa, and 20 Pa. The findings are illustrated in figure 20 and figure 21. Figure 20 shows, that for $k=10^{-13}$ m^2, J_n is insensitive to the magnitude of the depressurization since the entry is mainly diffusive. For higher permeabilities, J_n approaches the 'diffusive' limit for sufficiently small depressurization. J_n increases with the depressurization and the permeability of the soil in a complicated manner. For example, if the depressurization is changed from 0.1 Pa to 5 Pa for $k=10^{-11}$ m^2, then J_n is increased by a factor of app. 14. If the depressurization is doubled from 5 Pa to 10 Pa for the same permeability, J_n is increased by a factor of 1.7.

[22]The backfill material is likely to be coarse gravel with large grains and low radon generation
[23]The entry rate of soil gas is strictly linear in Δp, and is therefore left out of the table.

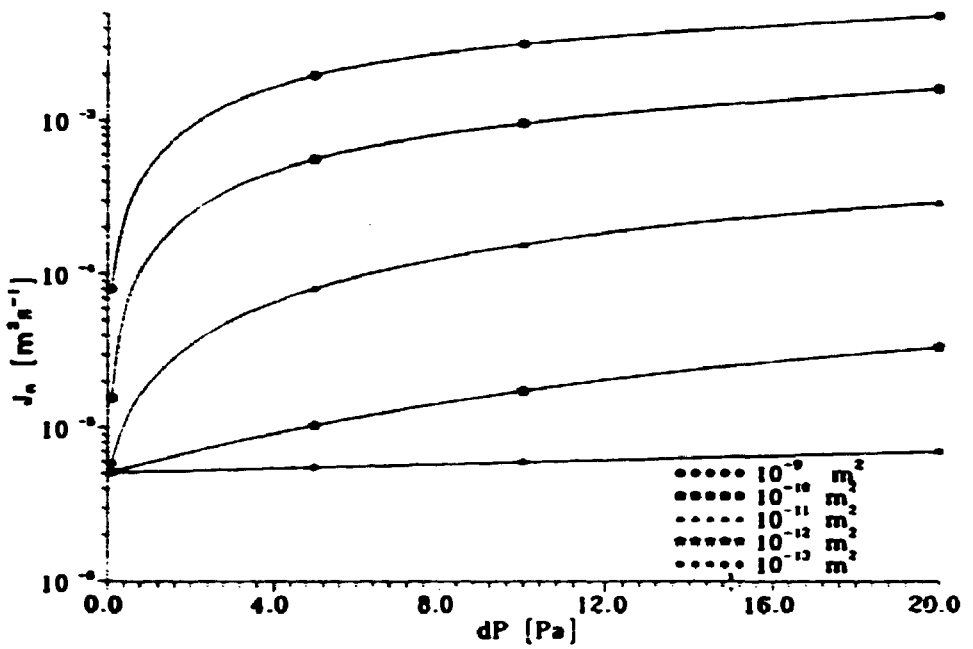

Figure 20. House depressurization: Normalized radon entry rate vs. depressurization for 5 different permeabilities. The curves are third degree polynomial fits.

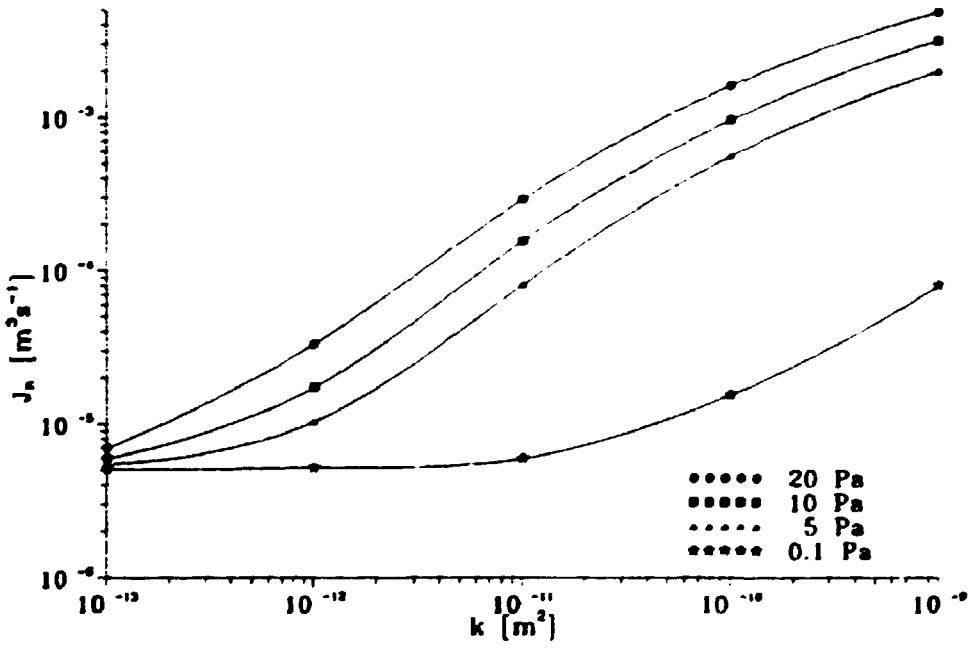

Figure 21. House depressurization: Normalized radon entry rate vs. permeability for 4 different depressurizations. The curves are third degree polynomial fits

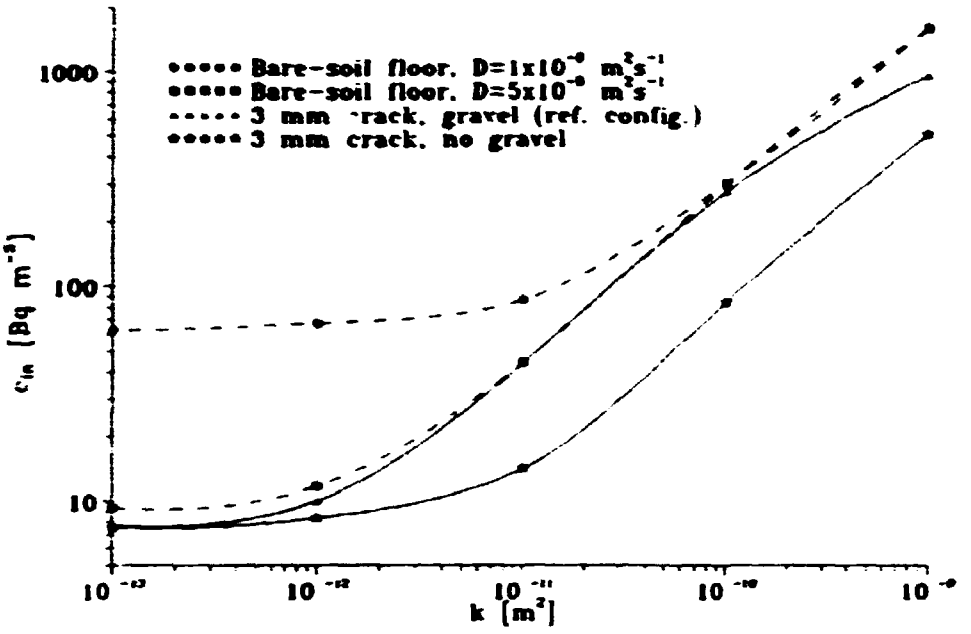

Figure 22. Indoor radon concentration versus permeability for various types of slab-on-grade houses calculated from the entry rates of the previous subsection and a simple mass-balance model (see text).

Indoor radon concentration

It[24] is instructive to convert the reported normalized radon entry rates into indoor radon concentrations using typical soil parameters and a simple single-zone mass-balance model for the accumulation of radon inside the house. The average exfiltration of air from the house to the atmosphere is given by the ventilation rate, λ_V, and the volume of the house, V:

$$Q_{exh} = V\lambda_V \tag{93}$$

We assume, that Q_{exh} is balanced by a supply of air from the atmosphere, Q_{atm}, and from the soil, Q[25]:

$$Q_{exh} = Q_{atm} + Q \tag{94}$$

and that the atmosphere and soil are the only sources of radon for the house, such that the indoor radon concentration can be found from:

$$c_{atm}Q_{atm} + c_{\infty}J_n = c_{in}Q_{exh} + \lambda V c_{in} \tag{95}$$

$$c_{in} = \frac{c_{atm}Q_{atm} + c_{\infty}J_n}{Q_{exh} + \lambda V} \tag{96}$$

where c_{in} and c_{atm} are indoor and outdoor radon concentrations.

We consider a standard 120 m^2 slab-on-grade house of the previously defined reference configuration. In addition, we set the indoor height to 2.5 m, such that

[24] This subsection has been revised April 1992

[25] Observe that Q is not always negligible compared with Q_{exh}. For $k=10^{-9}$ m^2, Q equals $8.2 \cdot 10^{-4}$ m^{3}s^{-1} for the bare soil-floor house as given in Table 12 which is app. 20 % of Q_{exh} if $V = 300$m^3 and $\lambda_V = 0.5$ h^{-1}. Experimentally, it has in fact been found, that the soil-gas entry rate may account for more than 20 % of the total air infiltration rate into specific houses. [Hubb88], [Turk87]

the volume is 300 m^3. The ventilation rate is set to 0.5 h^{-1}, which is typical for newer single-family houses in Denmark with mechanical ventilations; [Berg91]. The outdoor radon concentrations is set to 5 $Bq\,m^{-3}$, and the deep soil radon concentration, c_∞, is set to 20 $kBq\,m^{-3}$.

Figure 22 shows the indoor radon concentration for 4 slab-on-grade houses as function of the permeability: (1) is the house of the reference configuration (3 mm crack, subfloor gravel layer, D=10^{-6} $m^2\,s^{-1}$ etc.). (2) differs from (1) only by the absence of a subfloor gravel layer. (3) and (4) are houses with bare-soil floors located on soil with radon diffusivity equal to 10^{-6} $m^2\,s^{-1}$ and $5 \cdot 10^{-9}$ $m^2\,s^{-1}$, respectively. A number of observations can be made from figure 22. For example, for any given permeability the lowest indoor radon concentration is obtained for the perimeter-crack house not having a subfloor gravel layer. Adding such a gravel layer increases the entry considerably, and as can be seen from the figure, there is little difference between the total entry into a 'perimeter-crack house' with a sub-floor gravel layer and the advective entry into a similar house with a bare-soil floor.

Another observation is that the predicted indoor radon levels happen to be comparable with those found in the Danish nationwide survey from 1985 to 1986; [Sund87], [Ulb88]. The majority of the measured values (annual means) were in the range from 10-100 $Bq\,m^{-3}$, whereas a smaller part was found in the range from 100-700 $Bq\,m^{-3}$. For the living rooms of single family houses, the arithmetic mean was 76 $Bq\,m^{-3}$ (N=348, GM=56 $Bq\,m^{-3}$, and GSD=2.1).

5.4 Discussion

In the following, we list some of the limitations connected to the application of the model to real houses and summarize the results of the investigation.

Limitations

Firstly, the model treats soil-gas and radon transport under the idealizing assumption that the soil is homogeneous and isotropic. Hence, the modelling results cannot be applied to fractured media such as limestone or bedrock, where the highest indoor radon concentrations might be found.

Secondly, we have assumed the soil to be isothermal and thereby excluded natural convection as a driving force of soil gas. It was shown recently [Rev91], that buoyancy might increase the radon entry into a heated basement house with 40 %. Since the effect of buoyancy is likely to be different for slab-on-grade and basement houses, the validity of the comparison of the two house types presented herein is not valid for winter-time conditions.

Another limitation is connected to the assumption that the house depressurization is constant in time. In the presence of time-dependent driving forces (e.g. changes in the atmospheric pressure) advective transport of radon might be greatly enhanced especially for soils of low permeability; [Nar90]. Therefore, the model might underestimate radon entry rates. In the final two chapters of this report, we address the entry of soil gas in response to an indoor-outdoor pressure difference that varies cyclic in time.

Conclusion

The sensitivity analysis showed that the entry of soil gas and radon into houses depends on a number of geological and building related factors. First of all, the entry rate is proportional to the radon generation rate if the soil is homogeneous. Secondly, if the house has a crack along the perimeter and the slab is otherwise

radon tight, high entry rates can only be obtained by means of advection, and the diffusion constant is of minor importance. For moderate permeabilities, the entry rate is app. proportional to k and Δp. For a house with a bare-soil floor the situation is quite different, since diffusive entry dominates such that the permeability is only important for $k > 10^{-11}$ m^2, given the diffusion constant is not very low.

Of the remaining of the investigated factors, we found the existence of a subfloor gravel layer to be the most important since it might increase the entry rate of soil gas and radon by factors of 2 to 5. In addition, we found that the entry into a slab-on-grade house might be 10 % to 30 % lower than into a basement house of a similar configuration. Decreasing the depth of the footer of a slab-on-grade house was found to increase the entry rate of radon with up to 20 %, and the existence of a highly permeable backfill layer was found to affect the radon entry rate by less than 7 %. In general, the main findings of this study are similar to those reported in previous US-studies of entry into basement houses; [Lou87], [Rev90], [Rev91].

6 Analytical model, frequency domain

6.1 Background

The inside-outside pressure difference between a house and the atmosphere and the absolute value of the atmospheric pressure are not constant in time. For example, the inside-outside pressure difference changes in response to temperature, wind, and ventilation. In the steady-state model used in the previous chapters, we assumed the soil gas to be incompressible. This assumption is not valid if the time scale over which the pressure changes occur is short compared with the characteristic time for the propagation of a pressure perturbation in the soil, and as discussed in [Yok89], the steady-flow models represent a lower bound for advective entry rates of radon. More specifically, one recent model study of soil-gas entry into a basement house (with a bare-soil floor) showed that cyclic variations of the atmospheric pressure can greatly enhance the magnitude of soil-gas entry rates; [Nar90]. Relative to the soil-gas entry rate under static conditions, the effect was found to be most important for soils of low permeability. Hence, in the presence of time-dependent driving forces advective transport of radon might also play a role for soils of low permeability.

The purpose of the following is to contribute to the evaluation of entry of soil-gas into houses under dynamic conditions. Here, we describe a simple model based on the geometrical analogy between a basement house with a perimeter crack and a 'buried drain'. In this simplified geometry it is possible to derive an analytical expression for the development of the pressure field in the soil surrounding the drain. The soil-gas entry rate can thereafter be evaluated numerically. The analytical treatment is performed in the frequency domain, such that all quantities relate to a given frequency. In the next chapter, we report the outcome of an experimental investigation conducted at the Small Structures Project at Lawrence Berkeley Laboratory. Pressures have been measured in 8 soil probes while the structure was depressurized sinusoidally in time. The results are compared with the theoretical transfer function.

6.2 Mathematical equations

We model the dynamic entry of soil gas into a basement house having a narrow crack along the perimeter using a 'buried drain' geometry[26]. This geometry has previously been utilized for studies of steady-state soil-gas entry into houses: [DSMA83], [Mow86], [Naz88A]. The buried drain analogy provides a major simplification of the problem, and as demonstrated in [Mow86], there is little difference between the results obtained with a 2-dimensional numerical model of entry into a basement house and those of the buried drain model.

We imagine a drain of length L and radius a buried in homogeneous soil at depth d below the atmospheric surface. For a narrow crack ($a \ll L$), we can ignore the effects due to the ends of the drain and treat the problem in a 2-dimensional geometry using polar coordinates (r, θ) centered at the drain. The (disturbance) pressure field $p(r, \theta, t)$ in the soil develops in time t according to a diffusion equation:

$$\frac{\partial p}{\partial t} = D_p \nabla^2 p \tag{97}$$

where the Laplacian of p in polar coordinates is:

[26] Alternatively called, a bipolar geometry.

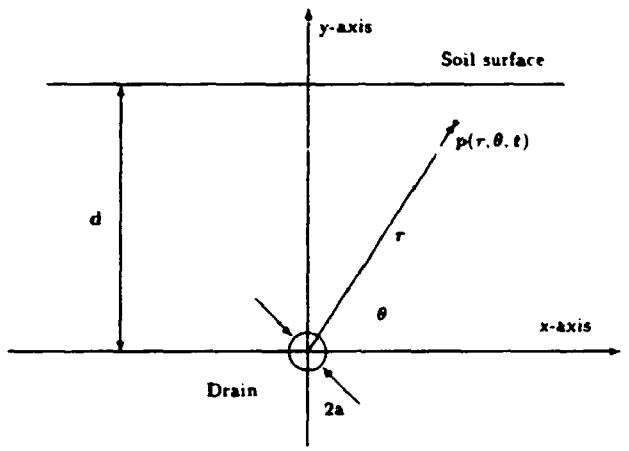

Figure 23. Geometry. Drain of radius a and length L buried at depth d below the atmospheric surface. The pressure at the field point is $p(r, \theta, t)$, where r and θ are polar coordinates.

$$\nabla^2 p = \frac{\partial^2 p}{\partial r^2} + \frac{1}{r}\frac{\partial p}{\partial r} + \frac{1}{r^2}\frac{\partial^2 p}{\partial \theta^2} \tag{98}$$

and where the diffusion constant for the pressure disturbance is:

$$D_p = \frac{k P_{atm}}{\mu \epsilon_a} \tag{99}$$

which can be obtained from Darcy's law, the conservation of mass, the state-equation for ideal gasses, and the assumption that the soil is isothermal; [Fuk55], [Clem74]. k is the permeability of the soil, P_{atm} is the absolute pressure at the atmospheric surface, μ is the dynamic viscosity, and ϵ_a is the air-porosity. The following boundary conditions apply to the present problem (for all t):

$$\begin{aligned} &\text{BC1: } p(r,\theta,t) \rightarrow 0 \text{ for } r \rightarrow \infty \\ &\text{BC2: } p(r,\theta,t) = 0 \text{ at the atmospheric surface} \\ &\text{BC3: } p(r,\theta,t) = \Delta p(t) \text{ for } r = a \end{aligned} \tag{100}$$

where the pressure difference $\Delta p(t)$ between the drain surface and the atmospheric air (corresponding to the indoor-outdoor pressure difference for the real house) is assumed to vary sinusoidally in time:

$$\Delta p(t) = p_1 \cos(\omega t) \tag{101}$$

A characteristic time for the propagation of a pressure perturbation introduced at the drain is:

$$T_0 = \frac{d^2}{D_p} = \frac{d^2 \mu \epsilon}{P_{atm} k} \tag{102}$$

and a characteristic frequency is:

$$\omega_0 = \frac{2\pi}{T_0} \tag{103}$$

Hence, we consider the frequency ω of the imposed disturbance pressure to be high or low relative to this value. We observe, that T_0 can take a large range of values. For d=2 m, μ=18.3 · 10^{-6} Pa s, ϵ=0.5, and P_{atm}=101 · 10^3 Pa, we have that T_0

equals 10 hr for $k=10^{-14}$ m^2, 6 min for $k=10^{-12}$ m^2, and 4 s for $k=10^{-10}$ m^2; cf. [Naz88B] p. 94.

The soil-gas flux density is given by Darcy's law:

$$\vec{q}(r,\theta,t) = -\frac{k}{\mu}\nabla p(r,\theta,t) \tag{104}$$

and the entry of soil gas into the drain (m^{3}s^{-1}) can be obtained by integration of $\vec{q}$ over the surface area:

$$Q(t) = aL\int_0^{2\pi} \vec{q}(r=a,\theta,t)\cdot(-\vec{r})d\theta \Leftrightarrow \tag{105}$$

$$Q(t) = aL\frac{k}{\mu}\int_0^{2\pi} \left.\frac{\partial p(r,\theta,t)}{\partial r}\right|_{r=a} d\theta \tag{106}$$

Definition of complex transfer functions

We introduce the complex notation[27]:

$$\Delta p(t) = \mathrm{Re}\left(p_1 e^{i\omega t}\right) \tag{107}$$

Because of the linearity of equations 99 and 106, we have that also the pressure field and the soil-gas entry rate oscillate sinusoidally with frequency ω. It is therefore convenient to introduce the complex transfer functions $F(r,\theta,\omega)$ and $G(\omega)$:

$$p(r,\theta,t) = \mathrm{Re}\left(p_1 F(r,\theta,\omega)e^{i\omega t}\right) \Leftrightarrow \tag{108}$$

$$p(r,\theta,t) = p_1\,|F(r,\theta,\omega)|\cos\left(\omega t + \angle F(r,\theta,\omega)\right) \tag{109}$$

and

$$Q(t) = \mathrm{Re}\left(G(\omega)e^{i\omega t}\right) \Leftrightarrow \tag{110}$$

$$Q(t) = |G(\omega)|\cos\left(\omega t + \angle G(\omega)\right) \tag{111}$$

Hence, we have transformed the problem from time to frequency domain:

$$p(r,\theta,t) \rightarrowtail F(r,\theta,\omega) \tag{112}$$

$$Q(t) \rightarrowtail G(\omega) \tag{113}$$

In the following, we derive an expression for $F(r,\theta,\omega)$ using the method of images, and it is therefore necessary firstly to find the solution to the assisting problem of *one drain in infinite space.*

One drain in infinite space

Consider a single drain in infinite space that has a disturbance pressure of $\Delta p(t)$ at the surface relative to infinite where the value is zero. Because of the axial symmetry, the disturbance pressure field $\tilde{p}(r,t)$ and the corresponding transfer function $\hat{F}(r,\omega)$ are independent of θ:

$$\tilde{p}(r,\omega) = p_1\mathrm{Re}\left(\hat{F}(r,\omega)e^{i\omega t}\right) \tag{114}$$

Substituting into equation 99 yields:

$$i\omega\hat{F}e^{i\omega t} = D_p\left(\frac{\partial^2\hat{F}e^{i\omega t}}{\partial r^2} + \frac{1}{r}\frac{\partial\hat{F}e^{i\omega t}}{\partial r}\right) \tag{115}$$

If we treat ω as a parameter, we obtain an ordinary differential equation in r:

[27] An alternative approach is to apply the Laplace transformation technique. The stationary solution is obtained if $i\omega$ is substituted for the Laplace variable s.

$$i\omega\bar{F} = D_p\left(\frac{d^2\bar{F}}{dr^2} + \frac{1}{r}\frac{d\bar{F}}{dr}\right) \Leftrightarrow \tag{116}$$

$$\frac{d^2\bar{F}}{dr^2} + \frac{1}{r}\frac{d\bar{F}}{dr} - \frac{i\omega}{D_p}\bar{F} = 0 \Leftrightarrow \tag{117}$$

$$\frac{d^2\bar{F}}{dr^2} + \frac{1}{r}\frac{d\bar{F}}{dr} - \lambda^2\bar{F} = 0 \tag{118}$$

where

$$\lambda^2 = \frac{i\omega}{D_p} \tag{119}$$

or

$$\lambda = \sqrt{\frac{\omega}{D_p}}e^{i\frac{\pi}{4}} \tag{120}$$

Equation 118 is the modified Bessel equation of 0-th order with solutions of the form:

$$\bar{F}(r,\omega) = \bar{A}(\omega)I_0(\lambda r) + \bar{B}(\omega)K_0(\lambda r) \tag{121}$$

where $I_0(z)$ and $K_0(z)$ are 0-order modified Bessel functions of the first and second kind. respectively: [Wat52] and [Abr72] p. 374. The coefficients: $\bar{A}(\omega)$ and $\bar{B}(\omega)$ depend on the boundary conditions.

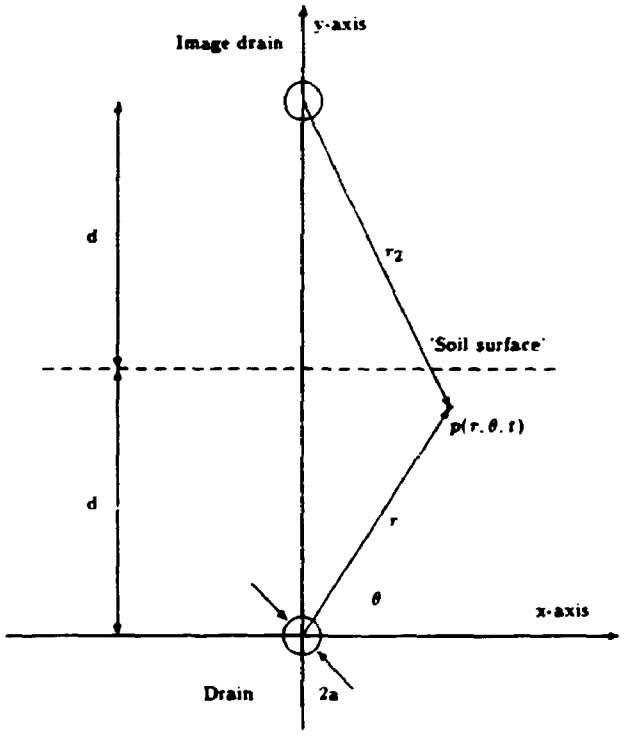

Figure 24. Location of the two drains.

Method of images

The solution to the original problem of *one drain below an isobaric surface* is equivalent to that of *two 'drains' in infinite space*. The first drain serves as a sink

and the second as a source, i.e. they are 180 degrees out of phase such that the line of symmetry remains at zero pressure. The transfer function: $F(r,\theta,\omega)$ can hence be obtained by superposition of two 'single-drain solutions' of the type specified in equation 121:

$$F(r,\theta,\omega) = A(\omega)\mathrm{I}_0(\lambda r) + B(\omega)\mathrm{K}_0(\lambda r) + C(\omega)\mathrm{I}_0(\lambda r_2) + D(\omega)\mathrm{K}_0(\lambda r_2) \quad (122)$$

where $r_2 = r_2(r,\theta)$ is the distance from the center of the image drain to the field point given by (r,θ):

$$r_2(r,\theta) = \sqrt{r^2 + 4d^2 - 4rd\sin\theta} \quad (123)$$

The coefficients: $A(\omega)$, $B(\omega)$, $C(\omega)$, and $D(\omega)$ can be found from the boundary conditions (for all ω):

$$\begin{aligned} &\text{BC1: } F(r,\theta,\omega) \;\rightarrow\; 0 \text{ for } r \rightarrow \infty \\ &\text{BC2: } F(r,\theta,\omega) \;=\; 0 \text{ for the 'atmospheric surface', i.e. where } r = r_2 \quad (124) \\ &\text{BC3: } F(r,\theta,\omega) \;=\; 1 \text{ for } r = a \end{aligned}$$

The first boundary condition (BC1) demands, that the pressure field at infinite must be zero. Since:

$$\mathrm{I}_0\left(x\sqrt{i}\right) \;\rightarrow\; \infty \text{ for } x \rightarrow \infty \quad (125)$$

$$\mathrm{K}_0\left(x\sqrt{i}\right) \;\rightarrow\; 0 \text{ for } x \rightarrow \infty \quad (126)$$

where x is real, we observe that it is solely the I_0-part of equation 122 that causes problems. A necessary condition for the field to be finite for $r \rightarrow \infty$ is that the singularities of the I_0-functions cancel each other:

$$A(\omega) = -C(\omega) \quad (127)$$

such that only the difference:

$$A(\omega)(\mathrm{I}_0(\lambda r) - \mathrm{I}_0(\lambda r_2)) \quad (128)$$

appears in the solution. However, this is not a sufficient condition. The asymptotic expansion of the I_0-function for $|\lambda r|$ large is given in [Abr72], p. 377 as:

$$\mathrm{I}_0(\lambda r) \sim \frac{e^{\lambda r}}{\sqrt{2\pi\lambda r}}\left(1 + \frac{1}{8\lambda r} + \frac{9}{2!(8\lambda r)^2}\cdots\right) \quad (129)$$

For field points located on the y-axis and $|\lambda r|$ large[28], the difference given in equation 128 approaches:

$$\mathrm{I}_0(\lambda r) - \mathrm{I}_0(\lambda r_2) = \mathrm{I}_0(\lambda r)\left(1 - e^{-2d\lambda}\right) \quad (130)$$

which is not limited according to equation 125. Thus, we conclude, that:

$$A(\omega) = 0 \quad (131)$$

and

$$C(\omega) = 0 \quad (132)$$

From the second boundary condition (BC2), it can be seen that:

$$B(\omega) + D(\omega) = 0 \quad (133)$$

and the solution therefore takes the form:

$$F(t,\theta,\omega) = B(\omega)\left(\mathrm{K}_0(\lambda r) - \mathrm{K}_0(\lambda r_2)\right) \quad (134)$$

The final boundary condition (BC3) gives, that:

[28] I.e. where $r > 2d$ and $\theta = \frac{\pi}{2}$ such that $r_2 = r - 2d$

$$1 = B(\omega)\left(K_0(\lambda a) - K_0(\lambda r_2)\right) \tag{135}$$

where r_2 is the distance from the image drain to the surface of the the real drain. In general, this cannot be fulfilled by means of a coefficient $B(\omega)$ that is independent of θ. However, for $a \ll 2d$, we have approximately that $r_2 \simeq 2d$, such that:

$$B(\omega) \simeq \frac{1}{K_0(\lambda a) - K_0(\lambda 2d)} \tag{136}$$

Thus, we have determined all coefficients of equation 122 and the transfer function is:

$$F(r,\theta,\omega) = \frac{K_0(\lambda r) - K_0(\lambda r_2)}{K_0(\lambda a) - K_0(\lambda 2d)} \tag{137}$$

Static limit

A simple test of the transfer function $F(r,\theta,\omega)$ is to see if the solution approaches a (known) static limit when the frequency ω is low compared with the characteristic frequency of the soil. Under static conditions equation 99 becomes the Laplace equation with the solution (for $a \ll d$): cf. [Mors53] p. 1210:

$$p_{static}(r,\theta) = \frac{\log(r) - \log(r_2)}{\log(a) - log(2d)}\Delta p \tag{138}$$

where Δp is the (constant) disturbance pressure of the drain relative to the atmospheric surface. Since the modified Bessel functions in equation 137 can be approximated by:

$$K_0(z) \simeq -\log(z) \tag{139}$$

for $|z|$ small, we see that the suggested transfer function in fact approaches the static limit for $\omega \to 0$.

6.3 Sample calculation

It is instructive to summarize the applied procedure and conduct a sample calculation. Accordingly, we assume that the pressure of the drain is forced to vary sinusoidally as:

$$\Delta p(t) = p_1 \cos(\omega t) \tag{140}$$

where p_1 is the amplitude (e.g. 1 Pa). The pressure at the atmospheric surface is zero. The disturbance pressure field in the soil, $p(r,\theta,t)$, vary with the same frequency as $\Delta p(t)$, but p is phase-shifted and has a different (lower) amplitude. The phase-shift and the (amplitude) attenuation are given by the complex transfer-function as specified in equation 109. For example, the pressure at the field point (r,θ) oscillates with an amplitude of:

$$p_1 |F(r,\theta,\omega)| = p_1 \left| \frac{K_0(\lambda r) - K_0(\lambda r_2)}{K_0(\lambda a) - K_0(\lambda 2d)} \right| \tag{141}$$

We refer to $|F(r,\theta,\omega)|$ as the frequency dependent pressure coupling (0 - 100 %). Figure 25 shows the development of the pressure coupling field from the static limit at T=100 T_0 to the high-frequency domain at T=0.01 T_0, where T is the period time: $T = \frac{2\pi}{\omega}$. The drain has a radius of 3.2 mm and is located at 2 m of depth. The figure demonstrates that the pressure coupling at any given location decreases with increasing frequency corresponding to the characteristics of a low-pass filter. The figure also shows that ω_0 appears to be a sound choice for a characteristic frequency since the field starts to reshape seriously for $\omega \simeq \omega_0$. Finally, it can be seen that the 'active' part of the soil[29] that participates in the cyclic exchange of soil gas decreases with frequency.

[29]The 'active' part of soil is equivalent to the depth of penetration defined in [Car59] p. 81.

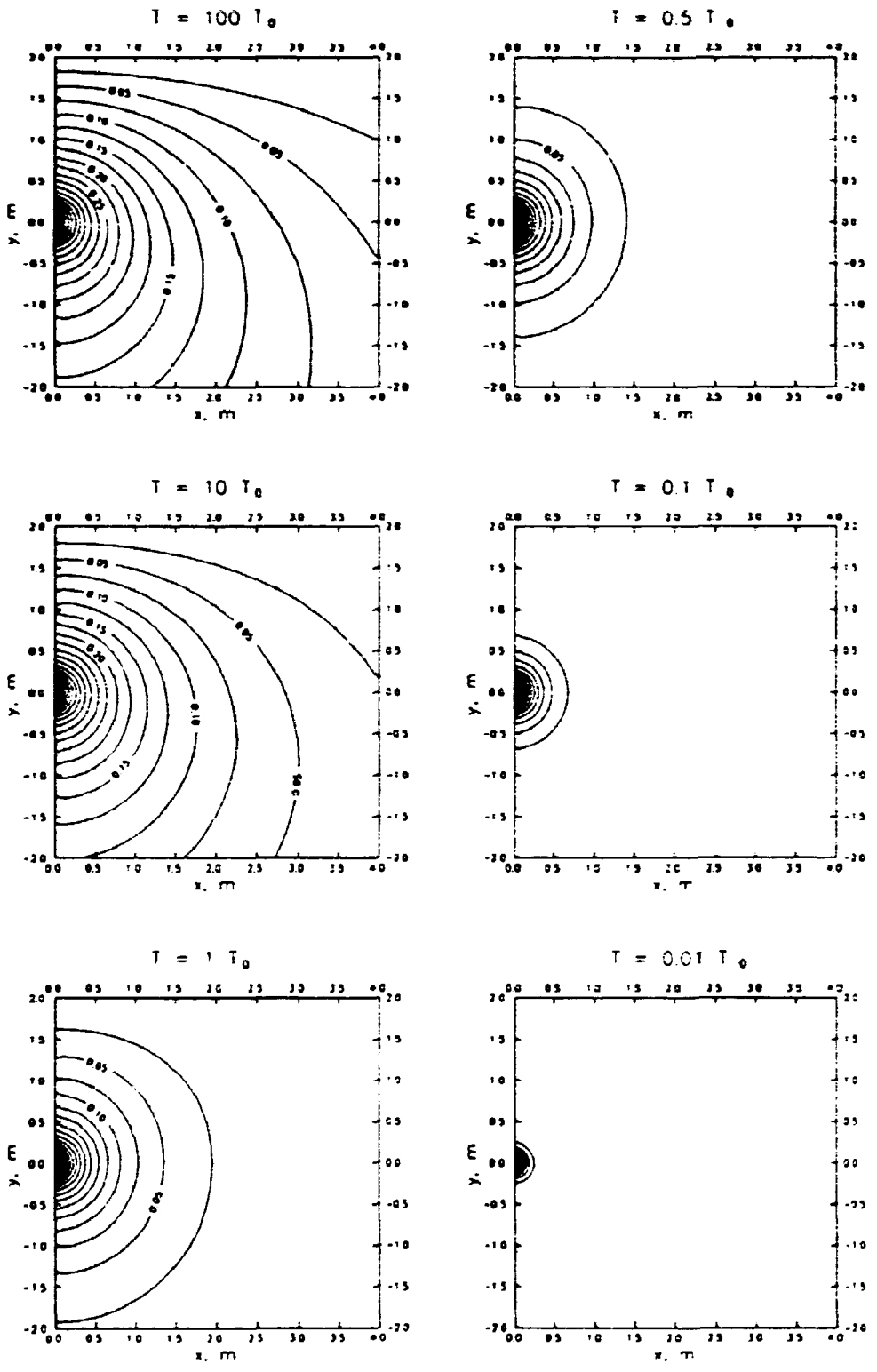

Figure 25. Model calculation of the pressure coupling field: $|F(r,\theta,\omega)|$ in the soil surrounding a drain of radius 3.2 mm buried at depth 2 m. $T = \frac{2\pi}{\omega}$ is the period time of the imposed drain pressure: $\Delta p(t) = p_1 \cos(\omega t)$. The drain is located at (0.0) and the atmospheric surface is at $y = 2$ m. T_0 is the characteristic time for propagation of a pressure perturbation in the soil.

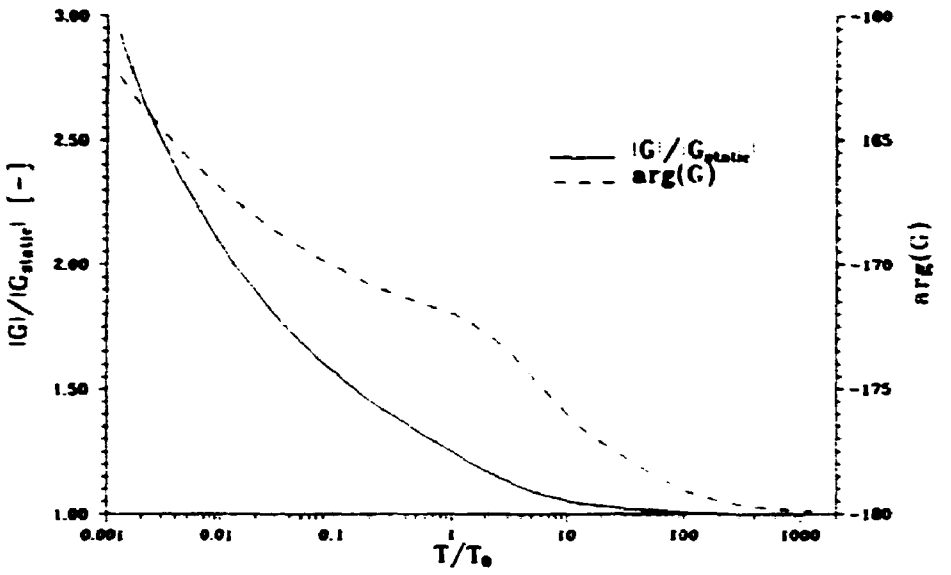

Figure 26. Model calculation of the transfer function for the soil-gas entry rate: $G(\omega)$ into a drain of radius 3.2 mm buried at depth 2 m. $T = \frac{2\pi}{\omega}$ is the period time of the imposed drain pressure: $\Delta p(t) = p_1 \cos(\omega t)$. T_0 is the characteristic time for propagation of a pressure perturbation in the soil.

Soil-gas entry rate

The transfer function $G(\omega)$ for the soil-gas entry rate can be found from equations 106, 109, and 111:

$$G(\omega) = aL\frac{k}{\mu}\int_0^{2\pi} \left.\frac{\partial F(r,\theta,\tau)}{\partial r}\right|_{r=a} d\theta \tag{142}$$

Differentiating equation 137 and using that: $K'_0(z)=-K_1(z)$ ([Abr72], p. 376) gives:

$$G(\omega) = \tag{143}$$

$$-aL\frac{k}{\mu}\int_0^{2\pi} \lambda \frac{K_1(\lambda a) - \frac{a-2d\sin\theta}{\sqrt{a^2+4d^2-4ad\sin\theta}} K_1(\lambda\sqrt{a^2+4d^2-4ad\sin\theta})}{K_0(\lambda a) - K_0(\lambda 2d)} d\theta$$

which can be evaluated using numerical integration techniques.

Figure 26 shows the phase and normalized amplitude of $G(\omega)$ for a drain of 3.2 mm in radius buried at 2 m of depth and with the parameters: $k=5 \cdot 10^{-11}$ m^2. $P_{atm}=92000$ Pa. and $\epsilon=0.5$. $|G(\omega)|$ is normalized with respect to:

$$|G_{static}| = \left| -\frac{2\pi kL}{\mu \cosh^{-1}(\frac{d}{a})} \right| \tag{144}$$

that comes from the solution of the corresponding static problem: see for example [Mow86]. We observe, that

$$\frac{|G(\omega)|}{|G_{static}|} \to 1$$

for $T \to \infty$, which is a supplementary test of the static limit. In addition, it can be seen that the flow rate amplitude increases with increasing frequency. For $T = T_0$,

the amplitude is approximately 25 % larger than for $T \gg T_0$. For $T = 0.01\ T_0$, the amplitude is more than doubled. The phaseshift of G is relatively small. For $T = T_0$, it amounts to less than 10 degrees compared with the static limit.

6.4 Conclusion

We have derived a transfer function for the behaviour of the pressure field surrounding a buried cylinder depressurized sinusoidally in time. The numerical evaluation of the soil-gas entry rate into the drain showed, that the steady-state solution represents a lower limit, such that the amplitude of the soil-gas entry rate increases with the frequency of the depressurization. The increased flow simply comes about because of alternate compression and expansion of soil gas in pore spaces of the 'active' part of soil volume. It is important to notice, that this does not necessarily lead to higher (net) entry rates of radon because the 'active' part of the soil shrinks with increasing frequency, and because the flow is oscillating back and forth (so-called reversed flow). The importance of the effect, for example in conjunction with changes in the atmospheric pressure, therefore depends on the mixing conditions of radon in the soil.

7 Experimental investigation, frequency domain

At the Small Structures Project at Lawrence Berkeley Laboratory, the soil-gas pressure field has been measured in 8 probes while the structure was depressurized sinusoidally in time. In the following, we describe the experimental situation at the Ben Lomond site and the results of the experiments. The results are compared with a theoretical transfer function based on the 'buried drain' analogy.

7.1 Structure design

The small structures are located at the Ben Lomond Mountain 12 km inland from the Pacific coast of California; [Fisk89]. The structures are designed especially for studies of radon entry into houses, and they provide the experimental part of an interdisciplinary research effort commonly referred to as the Small Structures Project. The structures are two room-size precisely-fabricated basements. Soil-gas enters the structures through adjustable aluminum slots located in the basement floor. The building shell is otherwise very tight with less than 1 cm^2 of effective leakage area. The structures are equipped with state-of-the-art instrumentation such that for example radon concentrations, pressures, and permeabilities can be measured continuously in the 32 soil-probes of each structure according to a pre-programmed pattern. Detailed descriptions of the structures can be found in [Fisk89], [Sext91], and [Gar92].

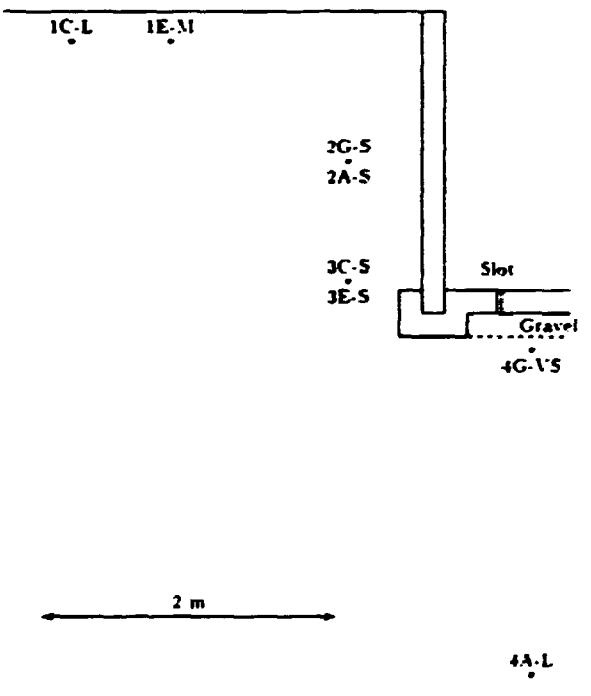

Figure 27. Sketch of structure and location of 8 probes.

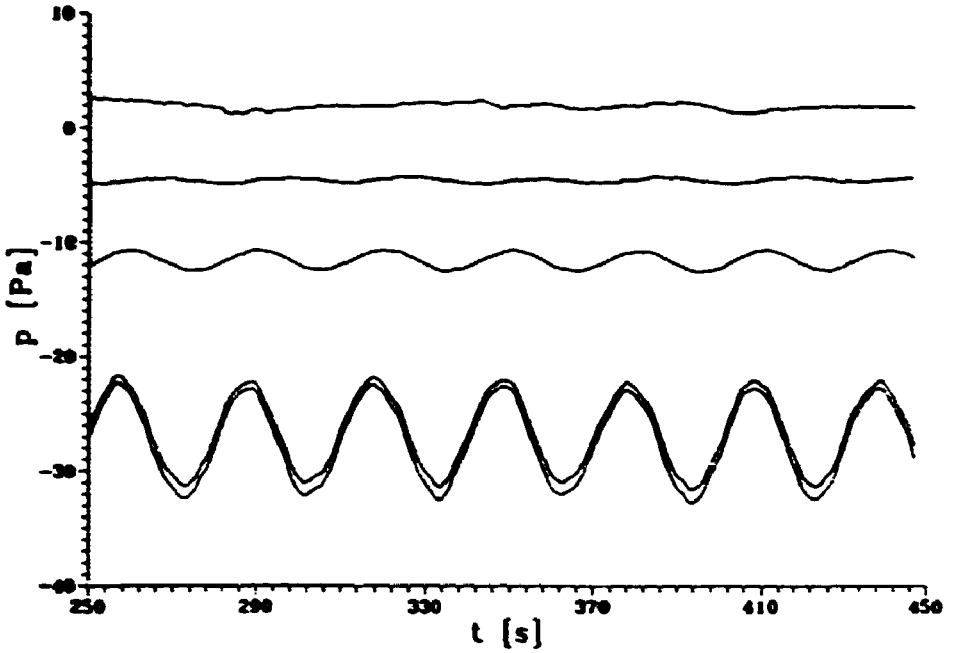

Figure 28. Experiment BLW54.04. where T=30 s. From top to bottom, the figure shows the measured pressures of the probes named: 1C-L, 2G-S, 3C-S, and 4G-VS. The bottom curve is the pressure of the structure. The pressures are measured relative to a reference probe located in the far field.

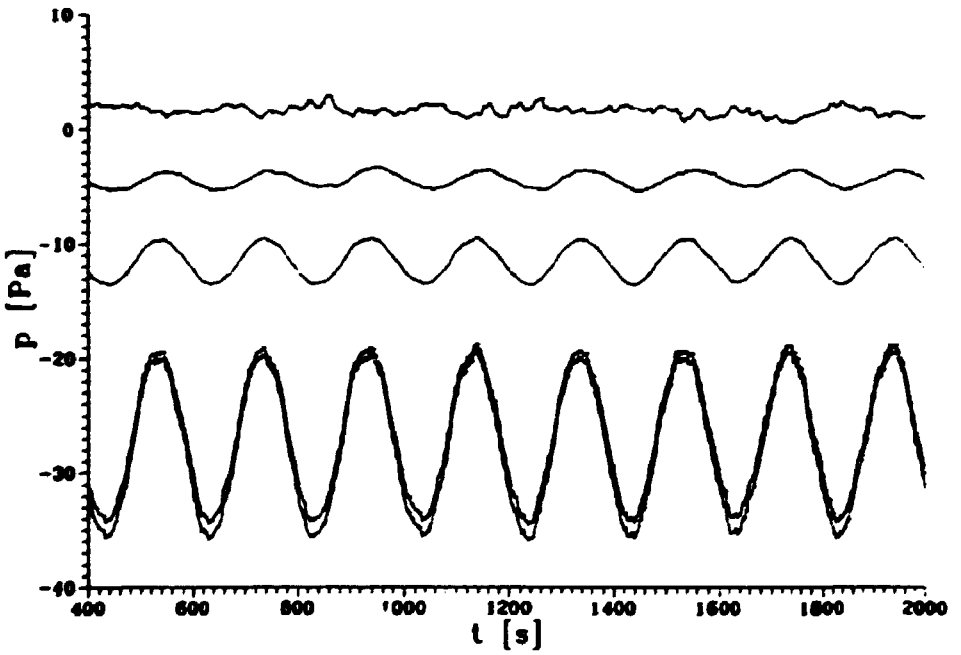

Figure 29. Experiment BLW54.06. where T=200 s. From top to bottom, the figure shows the measured pressures of the probes named: 1E-M, 2A-S, 3E-S, and 4A-L. The bottom curve is the pressure of the structure. The pressures are measured relative to a reference probe located in the far field.

Table 18. Measured pressure couplings at 4 probe locations: 1C-L, 2G-S, 3C-S, and 4G-VS.

Id	T	P_{straw}	High wall	Mid wall	Low wall	Sub slab
	sec	Pa	1C-L	2G-S	3C-S	4G-VS
BLW54.02	6	1.2	0.005	0.016	0.074	0.931
BLW54.10	7	1.4	0.015	0.023	0.088	0.940
BLW54.03	10	2.3	0.008	0.022	0.113	0.937
BLW54.36	18	3.5	0.049	0.033	0.154	0.940
BLW54.09	20	3.6	0.020	0.035	0.161	0.941
BLW54.30	23	7.6	(0.150)	0.035	0.156	0.942
BLW54.04	30	4.8	0.025	0.044	0.182	0.945
BLW54.01	60	6.5	0.028	0.072	0.218	0.948
BLW54.11	80	7.0	0.038	0.075	0.225	0.949
BLW54.05	100	7.3	0.027	0.084	0.233	0.949
BLW54.06	200	7.9	0.039	0.099	0.245	0.951
BLW54.08	900	4.1	0.083	0.119	0.260	0.953

Table 19. Measured pressure couplings at 4 probe locations: 1E-M, 2A-S, 3E-S, and 4A-L.

Id	T	P_{straw}	High wall	Mid wall	Low wall	Sub slab
	sec	Pa	1E-M	2A-S	3E-S	4A-L
BLW54.22	4	0.8	0.024	0.022	0.039	0.065
BLW54.21	9	2.0	0.148	0.002	0.085	0.101
BLW54.17	12	2.5	0.211	0.030	0.088	0.099
BLW54.20	15	2.9	0.126	0.024	0.111	0.111
BLW54.35	18	3.6	0.035	0.031	0.122	0.118
BLW54.28	20	3.8	0.031	0.032	0.131	0.137
BLW54.19	25	4.3	0.175	0.043	0.128	0.092
BLW54.27	27	4.5	0.009	0.039	0.143	0.143
BLW54.18	40	5.6	0.061	0.065	0.158	0.157
BLW54.26	70	6.7	0.003	0.076	0.189	0.203
BLW54.23	150	7.6	0.034	0.105	0.219	0.246
BLW54.29	300	8.1	0.016	0.111	0.233	0.267
BLW54.25	3154	8.6	0.025	0.114	0.234	0.280

Table 20. Probe locations in polar coordinates: r and θ. The coordinate system has its center at the bottom of the slot: see figure 27.

Probe Id	Type	r m	θ deg
1C-L	High wall	3.42	148
2G-S	Mid wall	1.43	135
3C-S	Low wall	1.03	168
4G-VS	Subfloor	0.34	-46
1E-M	High wall	2.87	141
2A-S	Mid wall	1.43	135
3E-S	Low wall	1.03	168
4A-L	Subfloor	2.39	-84

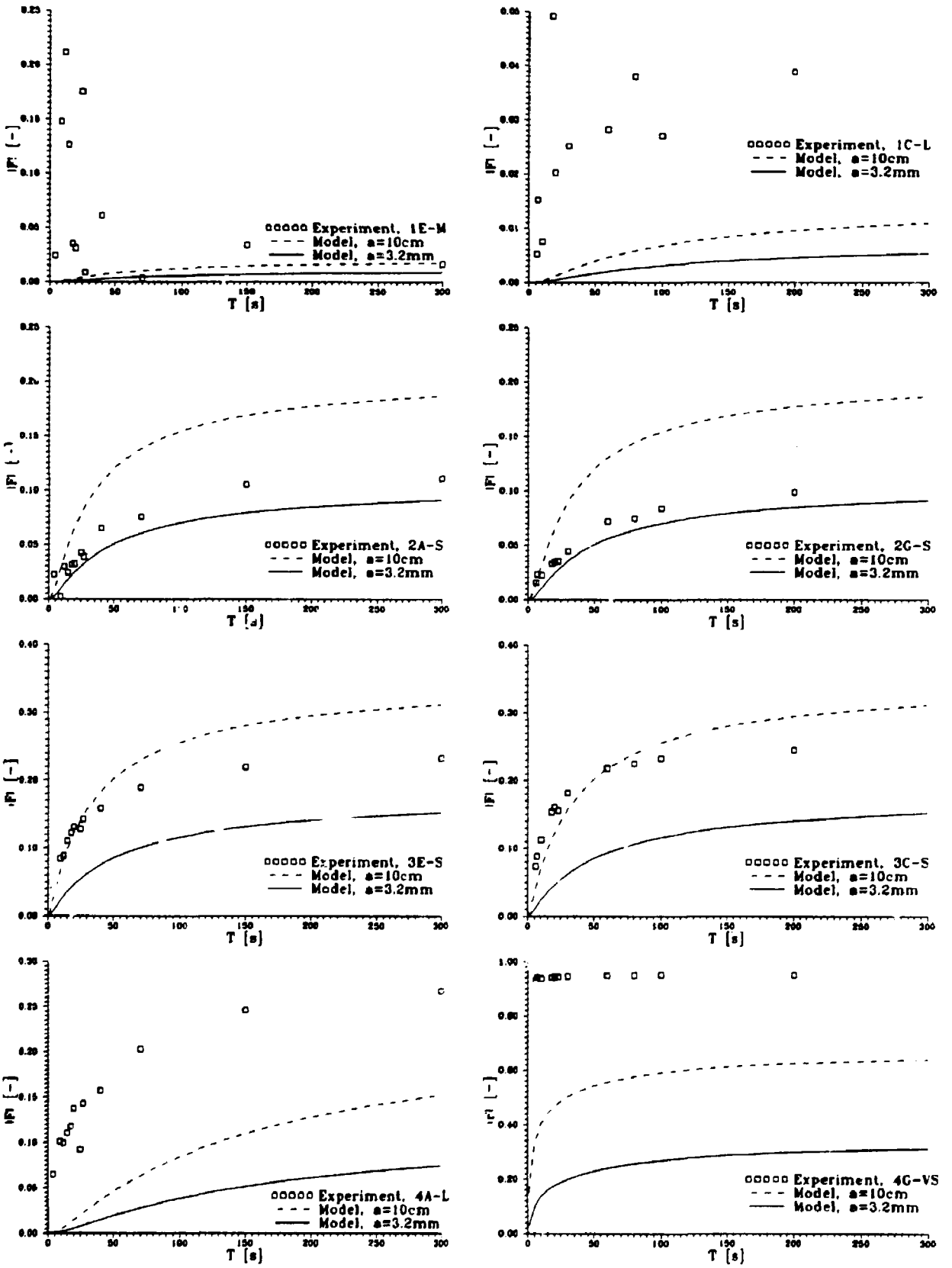

Figure 30. Comparison of measured and calculated pressure couplings for T=0 to 300 s for the 8 probes.

Experimental configuration

The set of experiments[30] reported herein was conducted over a period of 27 hours starting October 1, 1990 at the Ben Lomond west structure. The slot spacing was 3.2 mm. Two mass-flow controlled pumps were used to depressurize the structure sinusoidally in time around a baseline value of -27 Pa. The amplitude of the applied structure depressurization varied from 0.8 Pa to 8.6 Pa[31].

The pressures were measured with differential pressure transducers relative to a reference probe (in the far-field) for two sets of probes located in different positions of the ground. The first set consists of the probes named: 1C-L, 2G-S, 3C-S, and 4G-VS. The second set consists of: 1E-M, 2A-S, 3E-S, and 4A-L. The numbers refer to the level 1 - 4, with 1 being high at the basement wall, 2 and 3 at the mid and low part, and 4 in the basement floor.

Figure 28 shows measured pressures for a period time, T, equal to 30 s. The bottom curve corresponds to the pressure of the structure relative to the reference probe. Above that curve (almost on top the structure curve) is the pressure of the subfloor probe, 4G-VS. That probe is located very close to the gravel layer and is therefore well coupled. The three other curves correspond to the probes 3C-S, 2G-S, and 1C-L, respectively. We observe, that the pressure coupling decreases with the distance to the slot such that 1C-L is almost uncouppled to the structure. The 'random' fluctuations of 1C-L were found to be due to changes in the atmospheric pressure. Figure 29 shows the response for T equal to 200 s.

7.2 Experimental results

Tables 18 and 19 list the measured pressure couplings for the two sets of probes. Column two and three of the tables give the period time and amplitude of the structure depressurization. For example, for the experiment referred to as BLW54.36, the period time was 18 seconds and the amplitude of the pressure in the structure was 3.5 Pa. The pressure of the probe named 3C-S oscillated with an amplitude that was app. 15 % of that in the structure. The pressure couplings were found using fast Fourier analysis.

7.3 Model-experiment comparison

The[32] purpose of the following is to compare the experimental results with the theoretical transfer function $F(r, \theta, \omega)$ derived from the buried-drain model. As parameters in the model, we use values characteristic for the experimental situation: d=2 m, k=6 · 10^{-12} m^2 [33] [Gar92], ϵ=0.31 [Fisk89], and P_{atm}=92000 Pa such that the characteristic time for pressure propagation (see equation 102) is: $T_0 \simeq 40$ seconds. Model calculations are conducted for two drain radii: a=3.2 mm and a=10 cm corresponding to the slot-spacing and the thickness of the sub-slab gravel layer, respectively. The soil-probes are physically located on different sides of the structure. However, in order to apply the buried drain model it is necessary to map the probes relative to the slot as shown in figure 27. Table 20 gives the coordinates of the probe locations.

Figure 30 shows the measured and calculated pressure couplings of the 8 probes for period times in the range from 0 to 300 seconds. We observe some agreement

[30] Identified as BLW054.

[31] For a constant amplitude of the mass flows, the pressure variation inside the structure decreases with increasing frequency. This phenomenon was studied simultaneously using the framework of the so-called AC-pressurization technique; [Sher80]. For example, we also measured the structure response under conditions were the slots were sealed off.

[32] This section has been revised April 1992. The original Ph.D. thesis was based on incorrect values for porosity (0.5) and permeability (5 · 10^{-11} m^2).

[33] Mean value. The permeability ranges from approximately 2 · 10^{-13} m^2 to 3 · 10^{-11} m^2.

between the measured and calculated pressure couplings which supports the mathematics of the model and the physical significance of the characteristic time T_0 of 40 seconds applied in the model.

The best agreement is obtained for the 4 mid and low-wall probes: 2A-S, 3E-S, 2G-S, and 3C-S. For these probes, the model tends to predict the correct shape of the measured pressure coupling curves. Regarding the absolute values of the pressure couplings (e.g. the static limit), the model calculations corresponding to a=3.2 mm predict couplings that are lower than the measured values, whereas the model calculations for a=10 cm give pressure couplings that are too high.

The measured pressure couplings for probe 4A-L and 1C-L are higher than predicted by the model, which might be due to the geometric simplifications on which the model is based.

Probe 4G-VS is located a few centimeters below the gravel layer and therefore has a high (and relatively constant) pressure coupling of approximately 93 - 96 %. This is much higher than predicted by the model, since the model ignores the gravel layer. Probe 1E-M responded in a non-systematic way.

7.4 Conclusion

An experimental investigation has been carried out regarding the pressure coupling of soil probes when the structure was depressurized sinusoidally in time. The pressure couplings were found to decrease with increasing frequency corresponding to low-pass filter characteristics. The measurements were compared with a theoretical transfer function based on the buried-drain analogy. Considering, that the model ignores the existence of the structure and the subfloor gravel layer, and assumes the flow to be two-dimensional and the soil to be homogeneous, there was good agreement between the calculated and measured pressure couplings.

Acknowledgements

I would like to express my appreciation to the Indoor Environment Group at Lawrence Berkeley Laboratory for support and stimulation during my stay there. Especially, my sincere thanks go to Rich Sextro, Ashok Gadgil, Karina Garbesi, and Mark Modera for welcoming me at LBL and providing me with everything from helpful discussions to experimental guidance at the small structures.

In Denmark, I would like to thank my supervisors, Benny Majborn and Anders Damkjær who initiated this study, stimulated the test structure experiment, and helped me participate in various international meetings throughout the project.

Finally, special thanks to Jens Søgaard-Hansen for help with the solution of mathematical and experimental problems, Poul Christensen for letting me use his 486-machine during the last hectic months, Lis Sørensen for all types of moral and human support, and the rest of the Section of Health Physics for help and assistance during this work.

The study was jointly financed by Riso National Laboratory and the Danish Research Academy.

References

[Abr72] M. Abramowitz and I. A. Stegun. Handbook of Mathematical Functions. Dover publications, 1972.

[And84] D. A. Anderson, J. C. Tannehill, and R. H. Pletcher. Computational Fluid Mechanics and Heat Transfer. Hemisphere Publishing Corporation, 1984.

[Bak87] P. H. Baker, S. Sharples, and I. C. Ward. Air Flow through Cracks. *Building and Environment*, vol. 22, no. 4, p. 293, 1987.

[Bal85] C. C. Ballisager. Fundering af enfamiliehuse og mindre bygninger. SBI-anvisning 127, Statens Byggeforskningsinstitut, København, 1985 (in Danish).

[Bear72] J. Bear. Dynamics of Fluids in Porous Media. Dover Publications, 1972

[BEIR88] Committee on the Biological Effects of Ionizing Radiations; Health Risks of Radon and Other Internally Deposited Alpha Emitters: BEIR IV. National Academy Press, Washington, DC, 1988

[Berg91] N. C. Bergsøe. Undersøgelser af ventilationsforhold i nyere boliger. Luftskifte - Luftfugtighed - Organiske gasser og dampe. SBI-anvisning 213, Statens Byggeforskningsinstitut, København, 1991 (in Danish).

[Bird60] R. B. Bird, W. E. Stewart, and E. N. Lightfoot. Transport Phenomena. John Wiley & Sons, 1960.

[Bor91] T. B. Borak. Effects of Vegetation on Radon Transport Processes in Soil. In: Radon Research Program FY-1990. Project Summaries, p. 31-34. DOE/ER-0488P. U.S. Department of Energy, March 1991.

[Byg82] Kompendium i husbygning. Udvalgte blade af Byggebogen. Nyt Nordisk Forlag, Arnold Busk, 2. oplag, 1982 (in Danish).

[Car56] P. C. Carman. Flow of Gases through Porous Media. Butterworths Scientific Publications. 1956.

[Car59] H. S. Carslaw and J. C. Jaeger. Conduction of Heat in Solids. Second edition. Oxford Science Publications. Oxford. 1959.

[Chr69] G. Christensen and N. E. Andersen. Terrændæk. SBI-anvisning 72. Statens Byggeforskningsinstitut. København 1969 (in Danish).

[Clem74] W. E. Clements and M. H. Wilkening. Atmospheric Transport across the Earth-Air Interface. *Journal of Geophysical Research*. vol. 79. no. 33. 1974.

[Clev79] H. L. Clever (ed.). Solubility Data Series. Volume 2. Krypton. Xenon and Radon - Gas Solubilities. Pergamon Press, 1979.

[Col81] R. Collé, R. J. Rubin, L. I. Knab, and J. M. R. Hutchinson. Radon Transport Through and Exhalation from Building Materials: A Review and Assessment. NBS Technical Note 1139. National Bureau of Standards, U.S. Department of Commerce. 1981

[Dam91] A. Damkjær and U. Korsbech. Personal communication and 'A Small-Diameter Probe for In-situ Measurements of Gas Permeability of Soils'. Paper presented at Fifth International Symposium on the Natural Radiation Environment, Salzburg. September 22-28. 1991. To be published in *Radiation Protection Dosimetry*.

[Dim85] P. J. Dimbylow and P. Wilkinson. The Numerical Solution of the Diffusion Equation Describing the Flow of Radon Through Cracks in a Concrete Slab. *Radiation Protection Dosimetry*. vol. 11. no. 4. pp. 229-236. 1985.

[Dim87] P. J. Dimbylow. The Solution of the Pressure Driven Flow Equation for Radon Ingress Through Cracks in Concrete Foundations. *Radiation Protection Dosimetry*. vol. 18. no. 3. pp. 163-167. 1987.

[DOE90] U.S. Department of Energy. Office of Energy Research. and Office of Health and Environmental Research. FY-1990 Radon Research Program. DOE/ER-0488P. March 1991.

[Dom90] P. A. Domenico and F. W. Schwartz. Physical and Chemical Hydrogeology. John Wiley and Sons. 1990.

[DSMA83] DSMA Atcon Ltd. Review of Existing Instrumentation and Evaluation of Possibilities for Research and Development of Instrumentation to Determine Future Levels of Radon at a Proposed Building Site. Report INFO-0096. Atomic Energy Control Board. Ottawa. 1983.

[Fisk89] W. J. Fisk, S. Flexser, A. J. Gadgil. H. Y. Holman. M. P. Modera. T. N. Narasimhan, T. Nuzum. K. L. Revzan. R. G. Sextro. A. R. Smith. Y. W. Tsang. and H. A. Wollenberg. Monitoring and Modeling of Radon Entry into Basements: A Status Report for the Small Structures Project. LBL-27692. September 1989.

[Fred90] J. Fredericia. Sprækker og permeabilitet i moræneler. Instituttet for Teknisk Geologi. 1990 (in Danish).

[Fro91] F. Frost. Personal communication and 'En metode til måling af radon-emanation fra små jordprøver'. M.S. thesis. Dept. of Electrophysics. The Technical University of Denmark. September 1991 (in Danish).

[Fuk55] H. Fukuda. Air and Vapor Movement in Soil due to Wind Gustiness. *Soil Science* 79, p. 249-256. 1955.

[Gad91] A. J. Gadgil. Models of Radon Entry: A Review. Paper presented at Fifth International Symposium on the Natural Radiation Environment, Salzburg, September 22-28. 1991. To be published in *Radiation Protection Dosimetry*.

[Gar89] K. Garbesi and R. G. Sextro. Modeling and Field Evidence of Pressure-Driven Entry of Soil Gas into a House through Permeable Below-Grade Walls. *Environ. Sci. Technol.*, vol. 23, no. 12, p. 1481-1487. 1989.

[Gar92] K. Garbesi, R. G. Sextro. W. J. Fisk. M. P. Modera. and K. L. Revzan. Soil-Gas Entry into an Experimental Basement: Model-Measurement Comparisons and Seasonal Effects. Lawrence Berkeley Laboratory. Berkeley. CA. USA. LBL-31873. March 1992. To be submitted to *Environmental Science and Technology*.

[Har84] Harremoës. K. Ovesen. and M. Jacobsen. Lærebog i geoteknik 1. Polyteknisk forlag. 5. udgave. 1984 (in Danish).

[Hub88] L. M. Hubbard. B. M. Bolker. K. J. Gadsby. D. A. Hull. D. T. Harrje. and R. H. Socolow. Radon Dynamics Indoors. United States Department of Energy Research Report. contract no. 4545910.A02. December 20. 1988.

[Inc85] F. P. Incropera and D. P. DeWitt. Fundamentals of Heat and Mass Transfer. Second edition. John Wiley & Sons. 1985.

[Kors91] U. Korsbech. Technical University of Denmark. Personal communication.

[Lou87] C. O. Loureiro. Simulation of the Steady-state Transport of Radon from Soil into Houses with Basements under Constant Negative Pressure. Lawrence Berkeley Laboratory. Berkeley. CA. USA. LBL-24378. Ph.D. Dissertation. 1987.

[Lou90] C. O. Loureiro. L. M Abriola. J. E. Martin. and R. G. Sextro. Three-Dimensional Simulation of Radon Transport into Houses with Basements under Constant Negative Pressure. *Environ. Sci. Technol.*, vol. 24. no. 9. p. 1338. 1990.

[Mors53] P. M. Morse and H. Feshbach. Methods of Theoretical Physics. McGraw-Hill Book Company, Inc., 1953.

[Mow86] R. J. Mowris. Analytical and Numerical Models for Estimating the Effect of Exhaust Ventilation on Radon Entry in Houses with Basements or Crawl Spaces. Lawrence Berkeley Laboratory, Berkeley. CA. USA. LBL-22067. M.S. thesis. 1986.

[Mow87] R. J. Mowris and W. J. Fisk. Modelling the Effects of Exhaust ventilation on Radon Entry Rates and Indoor Radon Concentrations. *Health Physics*. 54. 1987. p. 491.

[Nar90] T. N. Narasimhan. Y. W. Tsang. and H. Y. Holman. On the Potential Importance of Transient Air Flow in Advective Entry into Buildings. *Geophysical Research Letters*. vol. 17. no. 6. p. 821-824. 1990.

[Naz88A] W. W. Nazaroff. Predicting the Rate of ^{222}Rn Entry from Soil into the Basement of a Dwelling due to Pressure-Driven Air Flow. *Radiation Protection Dosimetry*, vol. 24, no. 1/4, pp. 199-202, 1988.

[Naz88B] W. W. Nazaroff and A. V. Nero (ed.). Radon and its Decay Products in Indoor Air. Wiley-Interscience. 1988.

[Naz88C] W. W. Nazaroff, B. A. Moed, and R. G. Sextro. Soil as a source of Indoor Radon: Generation, Migration, and Entry. In: W. W. Nazaroff and A. V. Nero (ed.). Radon and its Decay Products in Indoor Air. Wiley-Interscience. 1988.

[Naz90] W. W. Nazaroff and K. Teichman. Indoor Radon. Exploring U.S. Federal Policy for Controlling Human Exposures. *Environ. Sci. Technol.* vol. 24, no. 6, pp. 774-782, 1990

[Nero89] A. V. Nero. Earth, Air, Radon and Home. *Physics Today*, p. 32, April 1989.

[Nero90] A. V. Nero, A. J. Gadgil, W. W. Nazaroff, and K. L. Revzan. Indoor Radon and Decay Products: Concentrations, Causes, and Control Strategies. DOE/ER-0480P. November 1990.

[Pat80] S. V. Patankar. Numerical Heat Transfer and Fluid Flow. Hemisphere Publishing Corporation. 1980.

[Pres86] F. Press and R. Siever. Earth. Fourth edition. W. H. Freeman and company, 1986.

[Pres89] W. H. Press, B. P. Flannery, S. A. Teukolsky, and W. T. Vetterling. Numerical Recipes in Pascal. The Art of Scientific Computing. Cambridge University Press, 1989.

[Rev90] K. L. Revzan and W. J. Fisk. Modelling Radon Entry into Houses with Basements: The Influence of Structural Factors. Lawrence Berkeley Laboratory, Berkeley, CA. USA, LBL-28109. May 1990.

[Rev91] K. L. Revzan, W. J. Fisk, and A. J. Gadgil. Modelling Radon Entry into Houses with Basements: Model Description and Verification. *Indoor Air*, 2, pp. 173-189, 1991.

[Rog90] V. C. Rogers and K. K. Nielson. Benchmark and Application of REATRAD Model. The 1990 International Symposium on Radon and Radon Reduction Technology: Volume III. Preprints. EPA/600/9-90/005c. Paper number: VI-1. January 1990.

[Rog91A] V. C. Rogers and K. K. Nielson. Multiphase Radon Generation and Transport in Porous Material. *Health Physics*, vol. 60, no.6 (June), pp. 807-815, 1991.

[Rog91B] V. C. Rogers and K. K. Nielson. Correlations for Predicting Air Permeabilities and ^{222}Rn Diffusion Coefficients of Soils. *Health Physics*, vol. 61, no.2 (August), pp. 225-230, 1991.

[Roy91] W. R. Roy and R. A. Griffin. An Analytical Model for In Situ Extraction of Organic Vapors. *Journal of Hazardous Materials*, 26, pp. 301-317, 1991.

[Sco63] R. F. Scott. Principles of Soil Mechanics. Addison-Wesley Publishing Company, 1963.

[Sext91] R. G. Sextro, W. J. Fisk, H. A. Wollenberg, T. N. Narasimhan, S. Flexser, A. J. Gadgil, K. Garbesi, M. Modera, T. Nuzum, K. L. Revzan, A. R. Smith, and Y. W. Tsang. An Experimental and Theoretical Examination of Radon Transport and Entry into Two Small Basement Structures. Paper presented at Fifth International Symposium on the Natural Radiation Environment, Salzburg, September 22-28, 1991. To be published in *Radiation Protection Dosimetry*.

[Sher80] M. H. Sherman. Air Infiltration in Buildings. Lawrence Berkeley Laboratory, Berkeley, CA, USA, LBL-10712. 1980.

[Sund87] Sundhedsstyrelsen. Naturlig stråling i danske boliger. Sundhedsstyrelsen, 1987 (in Danish).

[Søg91] J. Søgaard-Hansen. Risø National Laboratory. Personal communication.

[Turk87] B. H. Turk, R. J. Prill, W. J. Fisk, D. T. Grimsrud, B. A. Moed, and R. G. Sextro. Radon and Remedial Action in Spokane River Valley Homes. Volume 1: Experimental Design and Data Analysis. Lawrence Berkeley Laboratory, Berkeley, CA, USA, LBL-23430, 1987.

[Ulb88] K. Ulbak, B. Stenum, A. Sørensen, B. Majborn, L. Botter-Jensen, and S.P. Nielsen. Results from the Danish Indoor Radiation Survey. *Radiation Protection Dosimetry*, vol. 24, no. 1/4, pp. 401-405, 1988.

[UNS88] United Nations Scientific Committee on the Effects of Atomic Radiation. Sources and Effects of Ionizing Radiation. United Nations Publications, 1988.

[Wat52] G. N. Watson. A Treatise on the Theory of Bessel Functions. Cambridge at the University Press, 1952.

[Wil85] P. Wilkinson and P. J. Dimbylow. Radon Diffusion Modelling. *The Science of the Total Environment*, 45, pp. 227-232, 1985

[Wri88] A. D. Wrixon, S. L. Wan, and K. D. Cliff. The Origin of Indoor Radon. Radiation Protection Practice. Seventh International Congress of the International Radiation Protection Association, Sydney, 10-17 April 1988 (IRPA 7), proceedings vol. 1, pp. 228-231.

[Yok89] F. Y. Yokel. Site Characterization for Radon Source Potential. NISTIR 89-4106, U.S. Dept. of Commerce, 1989.

A Sample jobfile

This appendix contains a sample jobfile in Pascal used for the model calculation named Ad1; see table 6 on page 30. The jobfile controls the execution of the radon transport model named rnmod2d.pas: see page 17. Operational and general physical constants are defined in the procedure called: set_parameters. The geometrical constants: X1, X2 etc. and the boundaries BC_cen, BC_per etc. are indicated in figure 3 on page 18. The function named region divides the (i,j)-computational plane into user-defined regions specified in the type called regiontype = (struc, gravel, soil1 etc.). Physical parameters are specified for each region using the functions called: D, G, e, and beta.

```
program rn2_1124;
(* Main file: Rn2_xxxx.pas, Job specification   *)
(* Radon transport model                        *)
(* 2D-Finite difference, two-phase              *)
(* Claus E. Andersen                            *)
(* Dept. of Nuclear Safety Research             *)
(* Risoe National Laboratory                    *)
(* DK-4000 Roskilde, Denmark                    *)
(* E-Mail: claus@risoe.dk                       *)
(* January 31,  1992                            *)

{$M 2000,0,600000} (* Memory configuration *)
{$N+} (* 80287 numerical processor         *)
{$R-} (* Range checking                    *)
{$S-} (* Stack-overflow checking           *)

uses Dos,Crt;

const I12   = 6;   J01  = 6;
      I23   = 6;   J12  = 6;
      I34   = 18;  J23  = 6;
      I45   = 6;   J34  = 12;
      I56   = 6;   J45  = 6;
      I67   = 6;   J56 =  6;
      I78   = 10;
      I89   = 14;

type datatype    = real;
     regiontype  = (struc,gravel,soil1,soil2,soil3,soil4,soil5,soil6);

{$I rnmod2dL.aaa} (* Include : Declarations   *)

procedure set_parameters;
begin
job             :='Radon Test Struc, Case Ad1, advec. w. parm S1+S1';
qf:=on;   qfile :='c:\tp50\ou_1124.dat';   (* Output (main results)       *)
tf:=on;   tfile :='c:\tp50\it_1124.dat';   (* Iterations                  *)
gf:=off;  gfile :='c:\tp50\gr_1124.dat';   (* Grid: x[i], dx[i], z[j] etc.*)
pf:=off;  pfile :='c:\tp50\pl_1124.dat';   (* Plot file for Rn2_plot.pas  *)
af:=off;  afile :='c:\tp50\co_1124.dat';   (* Coefficients: aW,aE etc.    *)
xf:=on;   xfile :='c:\tp50\xf_1124.dat';   (* Special output              *)
lf:=on;   lfile :='c:\surfer\lu_1124.dat'; (* Surfer, stream lines        *)
rf:=off;  rfile :='c:\surfer\ru_1124.dat'; (* Surfer, residuals           *)
sf:=on;   sfile :='c:\surfer\su_1124.dat'; (* Surfer, field               *)
          ffile :='c:\tp50\ff_1101.dat';   (* Import/export flow field    *)
          cfile :='c:\surfer\su_1124.dat'; (* Import initial conc. field  *)

solver          := on;       (* Solver switch                           *)
iter_lines      := 20;       (* Number of iterations between output     *)
dclimit         := 1E10;     (* Limit for dcx and dcz in grid evaluation *)
```

```
streamlinefacter := 1E8;      (* Multiplication of streamfunction        *)
min_iterations   := 2;        (* Lower limit for number of iterations    *)
max_iterations   := 3000;     (* Upper limit for number of iterations    *)
convlimit        := 1E-8;     (* Limit for convergence, relative change  *)
cinit            := 0;        (* Initial value of field, if not imported *)
w                := 1.00;     (* Relaxation of field calc., 0 - 1.7      *)
scheme           := powerlaw; (* central, powerlaw, upwind, hybrid, exact *)
c_profile        := lin;      (* Interpol. func. f. flux calc: lin, log  *)
Deff_profile     := lin_mean; (* harm_mean, lin_mean, log_mean           *)

configuration    :=structure;    (* structure, probe                     *)
geometry         :=cylindrical;  (* cartesian, cylindrical               *)
grid             :=special;      (* uniform, special                     *)
initfield        :=import;       (* none, import                         *)
flowfield        :=import;       (* none, import, export                 *)
flowfactor       :=0.664;        (* Multiplication of imported flowfield *)

BC_struc   := accumulation;          (* constant, accumulation           *)
BC_cen     := true;     c_cen :=0;   (* Center crack                     *)
BC_per     := false;    c_per :=0;   (* Perimeter crack                  *)
BC_wat     := false;    c_wat :=0;   (* Water table                      *)
BC_wall    := false;    c_wall:=0;   (* Wall                             *)
BC_atm     := true;     c_atm :=0;   (* Atmosperic surface               *)
BC_atm_ext := long;                  (* short: I7-I9, long:I6-I9         *)

lambda     := 2.098E-6;            (* Decay constant, 1/s                *)
mu         := 18.3E-6;             (* Dynamic viscosity, Pa-s            *)
Vstruc     := 0.040;               (* Volume of structure, m3            *)
Vent       := 0.00;                (* Ventilation rate, 1/s              *)

Dref       := 0;                   (* Diffusion constant, m2/s           *)
Gref       := 0;                   (* Generation rate, Bq/(m3-s)         *)
eref       := 0;                   (* Porosity,-                         *)

isoil1:=I1;   jsoil1:=J2;              ocation of 1. reference point      *)
isoil2:=I7;   jsoil2:=J0+1;          (* Location of 2. reference point     *)
isoil3:=I9-1; jsoil3:=J4;            (* Location of 3. reference point     *)

L0:= 1;                              (* Length of cartesian y-coord., m    *)

I1:= 1E-6;       Z0:=0;
I2:= 0.0475;     Z1:=0.70;
I3:= 0.20;       Z2:=1.11;
I4:= 0.9027;     Z3:=1.33;
I5:= 1.00;       Z4:=1.48;
I6:= 1.264;      Z5:=1.60;
I7:= 1.279;      Z6:=2.00;
I8:= 2.00;
I9:= I0;
end; (* set_parameters *)


function region(i:itype; j:jtype):regiontype;
var r:regiontype;
begin
case j of
  J0..J1-1: r:=soil1;
  J1..J2-1: r:=soil2;
  J2..J3-1: r:=soil3;
  J3..J4-1: case i of
              I1..I4-1: r:=gravel;
              I4..I9-1: r:=soil4;
            end;
  J4..J5-1: case i of
```

```
            I1..I6-1: r:=struc;
            I6..I9-1: r:=soil5;
          end;
  J5..J6-1: case i of
            I1..I6-1: r:=struc;
            I6..I9-1: r:=soil6;
          end;
end;
region:=r;
end;

function D(i:itype; j:jtype):datatype;
(* Diffusion constants *)
begin
case region(i,j) of
  soil6,soil5:                D:=9.6862E-7;
  soil4,soil3,soil2,soil1:    D:=9.6862E-7;
  gravel:                     D:=5E-6;
else D:=0;
end;
end;

function G(i:itype; j:jtype):datatype;
(* Generation rate *)
begin
case region(i,j) of
  soil6,soil5:                G:=lambda*9.7*2.273509*1000;
  soil4,soil3,soil2,soil1:    G:=lambda*9.7*2.273509*1000;
  gravel:                     G:=lambda*5000;
else G:=0;
end;
end;

function e(i:itype; j:jtype):datatype;
(* Porosity *)
begin
case region(i,j) of
  soil6,soil5:                e:=0.53;
  soil4,soil3,soil2,soil1:    e:=0.53;
  gravel:                     e:=0.5;
else e:=0;
end;
end;

function beta(i:itype; j:jtype):datatype;
(* Partition corrected porosity *)
begin
case region(i,j) of
  soil6,soil5:                beta:=0.421472;
  soil4,soil3,soil2,soil1:    beta:=0.421472;
  gravel:                     beta:=e(i,j);
else beta:=0;
end;
end;

{$I rnmod2dL.bbb}  (* Include: Basics                  *)

{$Define solver}
{$IFDEF solver}
{$I rnmod2dL.ccc}  (* Include: Solver                  *)
{$ELSE}            (* Wr_special etc. + Post processing *)

procedure wr_special;
(* User definable output rutine *)
```

```
begin
end;

{$I rmod2dL.ddd}  (* Include: Post processor *)
{$ENDIF}

procedure set_grid_special;
(* User d     ed grid *)
begin
set_x_single(func2,X1,X2,1,I1, I2);
set_x_double(func1,func2,X2,X3, 1.5, 1.5, 0.2, I2, I3);
set_x_double(func1,func2,X3,X4, 1.7, 1.7, 0.5, I3, I4);
set_x_double(func1,func2,X4,X5, 1.7, 1.7, 0.5, I4, I5);
set_x_double(func1,func2,X5,X6, 1.7, 1.7, 0.5, I5, I6);
set_x_double(func1,func2,X6,X7, 1, 1, 0.5, I6, I7);
set_x_double(func1,func2,X7,X8, 2, 1, 0.2, I7, I8);
set_x_single(func1,X8,X9, 2,I8, I9);

set_z_double(func1,func2,Z0,Z1, 1.4, 1.4, 0.5, J0, J1);
set_z_double(func1,func2,Z1,Z2, 1.4, 1.4, 0.5, J1, J2);
set_z_double(func1,func2,Z2,Z3, 1.1, 1.1, 0.5, J2, J3);
set_z_double(func1,func2,Z3,Z4, 3.0, 3.0, 0.5, J3, J4);
set_z_double(func1,func2,Z4,Z5, 1.5, 1.5, 0.5, J4, J5);
set_z_double(func1,func2,Z5,Z6, 1.2, 1.2, 0.5, J5, J6);
end;

begin
  main
end.
```

B Scintillation cell measurements

Scintillation cell measurements of radon concentrations in the test structure probes. These results are summarized in table 2 on page 24. The measurements are given in units of kBq m^{-3}. 6.08.91 means August 6. 1991 etc.

ID	6.08.91 exp. 1	7.08.91 exp. 1	9.08.91 exp. 1	26.08.91 exp. 1	30.08.91 exp. 1
Cyl.	48.4/49.4	39.7		47.8	42.6
M1	45.9	44.8		39.9	39.0
M2	47.6	48.4	46.1	47.8/48.7	51.0
M3	60.4	57.2		58.9	57.6
M4	58.4	49.8		57.1	53.0
M5	61.3	50.8	58.7	59.4	61.1
M6	46.6	40.3		45.8	44.9
W1	26.3	14.9		34.5	32.8/29.3
E1	20.0	16.7/17.1	19.?	29.0	34.8
W2	50.2	45.6	48.1	46.2	51.1
W3	33.6	32.1/28.4		47.2	43.6
E3	24.3/21.5	21.4	19.6	34.4/33.8	32.2
W4	16.8/19.4	17.5		25.4	25.1
E4	15.8	14.7		26.4	19.8
W5	56.1	50.8	54.0	56.9	57.3
W6	27.0	22.0		35.3	28.6
E6	23.4	16.7		29.9	26.1/23.4
N1	45.0	46.6		47.1	49.8
N3	59.9	55.8/57.3		59.3	56.0
N4	25.1	17.5	23.4	33.1	25.2/25.1

ID	9.07.91 exp.2	10.7.91 exp. 2	11.7.91 exp. 2	12.7.91 exp. 2	24.7.91 exp. 3	25.7.91 exp.3
Cyl.	12.9		11.4		9.9	10.3/8.8
M1			9.9	9.4	7.2	5.6/6.6
M2	20.6		20.5	21.0	15.4	12.0/15.3
M3		44.5	46.5	49.7	44.5	45.5
M4		23.2	23.5	23.6	20.3	21.3/19.2
M5	30.7		28.9	32.0	27.4	30.1
M6			15.9	13.2	10.5	12.5
W1	9.2	7.8/8.9	8.8	6.9	7.0/7.0	8.3
E1		6.6/7.8	6.2	4.7	5.3	5.9
W2		46.4	40.4	44.6	50.4	49.9
W3				31.8	25.2	24.6/23.4
E3	23.7	23.0/18.3	21.4	17.2	18.6/17.1	17.0/15.1
W4		18.4/18.3	17.9	18.3	14.4	15.0
E4		18.4	16.7	15.8	14.6	15.1
W5				49.7		51.9/51.8
W6				11.8/11.6	9.8/9.7	8.3
E6				4.4/5.1	4.6	5.0
N1		47.7	44.6	44.0	39.9	43.3
N3		72.3	73.3	70.6	61.6	64.4
N4				(63.6)	22.3/32.7	29.5/25.2

C Model calculations

This appendix contains model calculations of pressure couplings (0-100 Pa), radon concentrations (kBq m^{-3}), and radon depletions (0-1) at probe locations at the radon test structure. Table 6 on page 30 summarizes the parameters used in each of the calculations.

Id	Pr1 Rn2_1100	Pr2 Rn2_1101	Pr3 Rn2_1102
Cyl	100	.30	100
M1	97.2	95.0	87.3
M2	81.7	79.9	75.4
M3	60.4	58.7	57.0
M4	77.0	75.1	70.9
M5	49.4	47.8	47.7
M6	96.6	96.5	89.2
W1	4.3	3.4	8.5
E1	4.0	3.2	7.9
W2	10.3	9.6	12.4
W3	5.5	4.9	8.6
E3	5.5	4.9	8.6
W4	0.8	0.6	2.3
E4	0.6	0.5	1.8
W5	2.7	2.5	7.9
W6	8.0	6.7	14.3
E6	8.0	6.7	14.3
N1	18.7	17.6	21.0
N3	4.3	3.9	6.1
N4	1.2	1.1	2.4

Id	Di1 Rn2_1110	Di2 Rn2_1115	Di3 Rn2_1117	Di4 Rn2_1116	Di5 Rn2_1111
Cyl	16.7	34.5	32.8	26.5	39.9
M1	17.8	38.3	36.5	40.3	45.0
M2	19.3	47.4	43.4	175.5	52.0
M3	20.3	55.3	46.8	159.9	59.1
M4	19.1	47.3	43.4	175.7	52.6
M5	20.0	55.2	46.4	157.8	59.9
M6	18.2	38.0	36.2	29.3	44.2
W1	7.5	6.6	7.3	4.6	29.9
E1	7.1	6.3	6.9	4.4	28.3
W2	19.9	59.1	43.4	115.1	63.8
W3	14.2	32.5	30.9	189.1	51.6
E3	14.2	32.5	30.9	189.1	51.6
W4	8.2	7.2	8.0	5.1	33.7
E4	6.6	5.9	6.6	4.3	28.0
W5	19.6	58.9	43.2	115.1	63.8
W6	11.8	14.2	14.7	92.7	43.3
E6	11.8	14.2	14.7	92.7	43.3
N1	18.7	53.3	43.9	153.4	60.9
N3	18.0	52.2	42.9	153.4	60.7
N4	13.9	32.3	30.7	189.1	51.5

Id	Ad1 Rn2_1124	Ad2 Rn2_1122	Ad3 Rn2_1125	Ad4 Rn2_1123	Ad5 Rn2_1120
Cyl.	9.4	14.9	13.2	27.4	17.3
M1	6.1	2.7	3.2	2.7	3.1
M2	16.4	47.8	35.9	105.5	52.1
M3	17.0	46.2	35.0	100.7	50.7
M4	14.8	36.9	30.2	73.3	41.7
M5	15.4	37.3	30.6	74.3	42.4
M6	8.6	11.[illegible]	10.6	18.7	13.3
W1	2.2	1.5	1.9	1.8	1.8
E1	2.0	1.4	1.8	1.7	1.6
W2	17.1	46.5	36.0	106.0	52.0
W3	9.8	9.6	10.9	14.1	16.2
E3	9.8	9.6	10.9	14.1	16.2
W4	6.2	3.9	4.7	3.3	12.6
E4	4.9	3.2	4.0	2.9	9.7
W5	18.4	52.9	39.9	124.3	58.3
W6	4.6	2.4	3.0	3.0	3.9
E6	4.6	2.4	3.0	3.0	3.9
N1	13.8	24.3	22.6	36.7	30.0
N3	15.7	36.0	32.0	74.8	44.2
N4	12.4	21.3	21.8	45.5	36.0

Id	Depl. 1	Depl. 2	Depl. 3	Depl.4	Depl. 5
Cyl	0.437	0.568	0.598	-0.033	0.560
M1	0.657	0.930	0.913	0.933	0.930
M2	0.152	-0.009	0.173	0.399	-0.001
M3	0.165	0.166	0.253	0.370	0.142
M4	0.225	0.221	0.303	0.583	0.208
M5	0.229	0.324	0.341	0.529	0.292
M6	0.527	0.705	0.707	0.361	0.699
W1	0.705	0.777	0.735	0.606	0.941
E1	0.712	0.778	0.736	0.610	0.942
W2	0.138	0.213	0.172	0.079	0.186
W3	0.311	0.703	0.648	0.925	0.687
E3	0.311	0.703	0.648	0.925	0.687
W4	0.244	0.466	0.406	0.343	0.627
E4	0.257	0.455	0.395	0.327	0.654
W5	0.061	0.103	0.078	-0.080	0.086
W6	0.611	0.834	0.795	0.968	0.909
E6	0.611	0.834	0.795	0.968	0.909
N1	0.265	0.544	0.485	0.761	0.507
N3	0.124	0.311	0.254	0.512	0.271
N4	0.107	0.340	0.290	0.759	0.301

D Dansk resumé

Indtrængning af jordgas og radon til huse er undersøgt eksperimentelt og teoretisk. Det eksperimentelle arbejde er foretaget ved hjælp af særlige radon teststrukturer etableret ved Forskningscenter Risø og Lawrence Berkeley Laboratory. USA.

En numerisk model af endelig-differens typen er opstillet ud fra de stationære transportligninger for Darcy-flow af jordgas og kombineret diffusion og advektion af radon. Modelberegninger foretaget på baggrund af målte jordparametre er sammenlignet med måleresultater fra teststruktur eksperimenter. Desuden er modellen anvendt til at belyse sammenhængen mellem radon indtrængningen for terrændæk huse og forskellige geologiske og bygningsmæssige forhold.

En analytisk model er udviklet for at beskrive indtrængning af jordgas under forhold, hvor undertrykket i huset varierer cyklisk. Tilsvarende er der foretaget teststrukturmålinger, hvor det dynamiske trykfelt i jorden blev kortlagt. Modelberegningerne er sammenlignet med målingerne.

Bibliographic Data Sheet **Risø-R-625(EN)**

Title and author(s)

Entry of Soil Gas and Radon into Houses

Claus E. Andersen

ISBN	ISSN
87-550-1804-1	0106-2840

Dept. or group	Date
Nuclear Safety Research	April 1992

Groups own reg. number(s)	Project/contract No.

Pages	Tables	Illustrations	References
86	26	30	66

Abstract (Max. 2000 char.)

Entry of soil gas and radon into houses has been investigated by a conjunction of experiments conducted at specially designed radon test structures and numerical or analytical modelling.

The numerical model solves the steady-state equations for Darcy flow of soil-gas and combined diffusive and advective transport of radon. Model calculations have been compared with results from field experiments conducted at Risø National Laboratory, and it was found that there was good agreement between measured and modelled pressure coupling and radon concentration profiles. However, discrepancies regarding absolute values of soil-gas entry rates and radon concentrations were observed.

The numerical model has been used to study the importance of soil and building related factors on radon entry rates into slab-on-grade houses. It was found, that for a house with a 3 mm perimeter crack along the floor-wall joint, the entry was mainly determined by the soil permeability and building related factors such as house depressurization and presence of a capillary breaking layer of gravel below the slab. For a house with a bare soil floor, the diffusivity of the soil was found to be of principal importance for the entry rate even for moderate permeabiiities.

Finally, an analytical model has been developed for the purpose of studying soil-gas entry rates into houses in response to non-static driving forces. The model is based on the analogy between a 'buried drain' and a basement house with a perimeter crack. The modelling results have been compared with experiments conducted at a test structure at the Lawrence Berkeley Laboratory. The structure was depressurized sinusoidally in time and the frequency dependent pressure couplings were measured. There was fairly good agreement between theoretical and experimental results given the simplifying assumptions underlying the model.

Descriptors INIS/EDB

ADVECTION; AIR INFILTRATION; CONVECTION; DARCY LAW; DIFFUSION; ENVIRONMENTAL TRANSPORT; FINITE DIFFERENCE METHOD; GAS FLOW; HOUSES; MATHEMATICAL MODELS; PERMEABILITY; RADON 222; SOILS. TRANSFER FUNCTIONS

Available on request from:
Risø Library, Risø National Laboratory (Risø Bibliotek, Forskningscenter Risø)
P.O. Box 49, DK-4000 Roskilde, Denmark
Phone (+45) 42 37 12 12, ext. 2268/2269 · Telex 43 116 · Telefax (+45) 46 75 56 27

Available on request from:
Risø Library
Risø National Laboratory,
P.O. Box 49, DK-4000 Roskilde, Denmark
Phone +45 42 37 12 12, ext. 2268/2269
Telex 43116, Telefax +45 46 75 56 27

ISBN 87-550-1804-1
ISSN 0106-2840